Luciano de Oliveira Júnior

WATER CIRCULATION ALONG THE NORTHERN MARGIN OF THE GULF OF CADIZ

UNIVERSIDADE DO ALGARVE

FACULDADE DE CIÊNCIAS E TECNOLOGIA

2023

Luciano de Oliveira Júnior

WATER CIRCULATION ALONG THE NORTHERN MARGIN OF THE GULF OF CADIZ

Doutoramento em Ciências do Mar, da Terra e do Ambiente,

Ramo: Ciências do Mar

Trabalho efetuado sob a orientação de: Doutor Erwan Garel

Prof. Doutor Paulo Relvas

UNIVERSIDADE DO ALGARVE

FACULDADE DE CIÊNCIAS E TECNOLOGIA

2023

Water circulation along the northern margin of the Gulf of Cadiz

Declaração de autoria de trabalho

Declaro ser o(a) autor(a) deste trabalho, que é original e inédito. Autores e trabalhos consultados estão devidamente citados no texto e constam da listagem de referências incluída

Copyright

Acknowledgments

My most sincere thanks go to Erwan Garel, my supervisor who had always time to help. I thank him for being patient and dedicated to help me with the struggle of scientific writing and most importantly I thank him to always push me in order to progress and become a better professional.

I also thank Paulo Relvas for all the support, clarifications and advises during this period.

Especially, I thank Tainá Garcia da Fonseca, who was always on my side motivating me and giving me support in the most difficult moments. Thanks to my son Caetano who fill my life with love and helps me to carry on every day with joy.

I would like to acknowledge IPMA for being one of the originators of the ADCP data set used for this work and a special thanks to Teresa Drago who has been putting a lot of effort to maintain the data acquisition active. I acknowledge Puertos del Estado for freely providing the high-frequency radar data which was also essential for the development of this work.

Financial support

This work was funded by Fundação para a Ciência e Tecnologia, through the PhD fellowship SFRH/BD/140250/2018

Resumo

Um conjunto inédito de observações que inclui perfis verticais de corrente medidos por um correntómetro acústico de efeito Doppler (ADCP) em 5 locais durante vários fundeamentos entre 2008 e 2019, e também 4,5 anos de velocidades superficiais coletadas por radares de alta frequência (HFR) são analisados na presente Tese juntamente com outras variáveis ambientais. O objetivo principal deste trabalho é atualizar o conhecimento sobre os padrões de circulação e explicar a dinâmica envolvida nos padrões observados. Ventos provenientes de um modelo de previsão de alta resolução foram usados para avaliar o efeito da interação atmosfera-oceano com o intuito de inferir sua relevância no desenvolvimento da circulação oceânica na área de estudo. Os resultados mostram que a variabilidade sazonal e espacial de diferentes mecanismos de afloramento está associada com a variabilidade do gradiente transversal de pressão, contribuindo assim para a posição meridional da Corrente do Golfo de Cádiz sobre o talude continental na região oeste. Além disso, uma depressão do nível do mar é frequentemente observada na mesma região onde se observam valores elevados de Ekman "pumping". O efeito dessa depressão poderá contribuir significativamente para o desenvolvimento do vórtice ciclónico e de escoamentos para oeste ao longo da costa. Na plataforma, a circulação é polarizada, alinhada com a direção da costa. As principais direções, para oeste ou para leste, são observadas praticamente com a mesma frequência. Os escoamentos para leste estão associados com a ação direta do vento, enquanto os escoamentos para oeste estão associados a um gradiente horizontal de pressão ao longo da costa, possivelmente como resultado da intensidade variável do afloramento ao longo da costa. Por fim, a análise extensiva das observações provenientes dos HFR e ADCPs possibilitou o desenvolvimento de um modelo conceptual da circulação superficial para os períodos de primavera e verão.

Palavras-chave: Oceanografia Costeira, Contra corrente costeira, Gradiente horizontal de pressão, Corrente do Gulf of Cadiz, Afloramento Costeiro, Ekman pumping, Radar de alta frequência, ADCP

Abstract

A novel set of current observations that includes multi-year (from 2008 to 2019) acoustic Doppler current profiler (ADCP) vertical profiles at 5 different locations and 4.5 years (2016-2020) of surface velocities from high-frequency radars (HFR) are explored in this Thesis along with relevant environmental variables to depict the ocean circulation along the northern margin of the Gulf of Cadiz (NMGoC), and to postulate explanations for the dynamics involved. High-resolution modelled winds were used to assess the exchange of momentum with the atmosphere, and to infer their relevance on driving the ocean circulation at the NMGoC. Results show that the seasonal and spatial variability of different upwelling mechanisms are associated with the variability of the cross-shore pressure gradient, which contributes significantly to the meridional position of the Gulf of Cadiz Current over the western bight. In addition, a permanent mean sea level depression corresponds to the location of the strongest Ekman pumping. The dynamic adjustment of this depression may contribute to drive a cyclonic cell at the western region and alongshore poleward currents along the entire NMGoC. Over the shelf, HFR and ADCP data show that the circulation is overall balanced, polarized in the alongshore direction and fluctuates with the wind. Equatorward flows were shown to be associated with the wind forcing while poleward flows were shown to be associated with an alongshore pressure gradient possibly resulting from the alongshore variability of the upwelling intensity. Finally, the extensive analysis of the HFR and ADCP observations provided a holistic understanding of the circulation that culminated with a detailed conceptual model of the spring and summer surface circulation for the region.

Keywords: Coastal oceanography, Coastal counter currents, Alongshore pressure gradient, Gulf of Cadiz current, Coastal upwelling, Ekman pumping, High-frequency radar, ADCP

Resumo Alargado

O Sistema de afloramento costeiro da Corrente das Canárias está entre as áreas mais produtivas do oceano que inclui também os sistemas de afloramento da California, Benguela e Humboldt/Peru. No entanto, a presença do Golfo de Cádiz, uma enseada de águas atlânticas localizada entre a ponta SW da Península Ibérica e a costa NW do continente africano, diferencia o sistema de afloramento das Canárias de seus análogos. O Golfo de Cádiz impõe uma importante descontinuidade no sistema das Canárias devido as abruptas mudanças de orientação da linha costa. Além disso, a troca de água com o Mar Mediterrâneo adjacente é uma característica importante que afeta significativamente o balanço de salinidade do Atlântico Norte. O processo inicial relacionado com o escoamento do Mediterrâneo para o Atlântico ocorre ao longo da margem norte do Golfo de Cádiz (NMGoC) que é delimitada pelo Cabo de São Vicente (CSV) a oeste e pelo Estreito de Gibraltar a leste. Embora muito esforço tenha sido feito para estudar a dinâmica e os caminhos das águas mediterrânicas ao longo da NMGoC, muito menos esforços foram dedicado à circulação das camadas superiores, especialmente na região da plataforma continental onde uma série de atividades socioeconômicas se desenvolvem e onde também ocorrem processos físicos importantes para o ecossistema marinho. Apesar de sua importância, a circulação das camadas superiores da NMGoC é surpreendentemente pouco conhecida, e além do mais, a literatura científica é marcada pela falta de consenso acerca de vários aspetos dos processos físicos envolvidos. Motivada pela existência de um conjunto inexplorado de observações de velocidades de corrente, a presente Tese visa contribuir para definir a circulação oceânica ao longo da NMGoC. O objetivo central deste trabalho é atualizar o conhecimento sobre os padrões de circulação e explicar a dinâmica envolvida nos padrões observados. O conjunto de observações utilizados inclui perfis verticais medidos por correntómetro acústico de efeito Doppler (ADCP) em 5 locais diferentes durante várias campanhas entre 2008 e 2019, e também 4,5 anos de velocidades superficiais coletadas remotamente por radares de alta frequência (HFR). A análise destas observações em conjunto com outros parâmetros ambientais, fornece uma compreensão holística da circulação costeira e do talude continental em várias escalas temporais e espaciais. O trabalho desenvolvido e as principais conclusões para alcançar o objetivo proposto estão apresentados em três capítulos principais (Capítulos 2, 3 e 4) organizados na forma de artigos científico. A Tese termina com uma seção de conclusão que integra as principais conclusões e lança luz sobre trabalhos futuros.

No Capítulo 2, a circulação superficial (subtidal) da NMGoC é descrita com base em medições de HFR durante o período de 2016 a 2020. Análises estatísticas (média, desvio padrão, excentricidade e funções ortogonais empíricas) foram aplicadas ao conjunto de dados, que foi completado com múltiplas séries temporais de ADCP e vento (ERA5). Fora da plataforma, o principal padrão de circulação consiste numa corrente de talude, a corrente do Golfo de Cádiz (GCC), que é observada ao longo do ano. Na região leste da NMGoC, a GCC não apresenta variações significativas durante as diferentes estações do ano. A região oeste da GCC tem valores médios mais elevados no verão e ocupa uma grande área sobre o talude continental enquanto no inverno os seus valores médios de velocidade são mais baixos e a GCC se encontra centrada no limite da plataforma continental. A circulação sobre o talude muda de sentido durante eventos de ventos com componente leste aproximadamente >10 m.s−1. Na plataforma, a direção das correntes é polarizada e alinhada com a direção da costa, sendo que as direções principais, para oeste ou para leste, são observadas praticamente com a mesma frequência. A circulação é geralmente contínua ao longo da costa, exceto para escoamentos para oeste (PFs) fracos (<0,1 m.s−1, de forma geral). Neste caso, o fluxo tende a ser para leste na região do Cabo Santa Maria. No inverno, os PFs geralmente estendem-se por toda a margem e são principalmente induzidos pelo vento. No verão, PFs geralmente consistem em contracorrentes costeiras (CCCs) com direção oposta à da corrente sobre o talude. As CCCs estão associadas a uma recirculação ciclónica significativa a oeste, onde um vórtice transitório é brevemente observado quanto a intensidade do vento diminui. Esse vórtice desenvolve-se após períodos de fortes ventos de noroeste, sugerindo que as CCCs resultam do desequilíbrio de um gradiente de pressão regional ao longo da costa.

No Capítulo 3, os ventos do modelo de previsão de alta resolução SKIRON foram usados para estimar o transporte de Ekman e o Ekman “pumping”, e explorar seus efeitos na circulação da NMGoC juntamente com outras variáveis relevantes como a temperatura da superfície do mar, anomalia do nível do mar e observações de correntes. Neste capítulo foi mostrado que em geral as condições favoráveis ao afloramento ocorrem ao longo do ano em toda a NMGoC, e com maior intensidade perto do CSV devido ao efeito persistente do Ekman “pumping”. Durante o inverno, a divergência superficial é restrita à região costeira devido a eventos fracos de Ekman “pumping” centrados na região da plataforma interna e também fortes eventos de transporte de Ekman, o que resulta num gradiente transversal do nível do mar localizado próximo da costa.

Durante o verão o gradiente intensifica-se e estende-se mais sobre a região do talude (na região oeste da NMGoC) devido à intensificação do Ekman "pumping" associada ao CSV. A variabilidade sazonal dos diferentes mecanismos de afloramento e a sua influência na posição e intensidade do gradiente transversal do nível do mar contribui assim para a posição meridional da GCC (geostrófica) sobre o talude da plataforma ocidental ao longo do ano. Além disso, uma depressão permanente do nível do mar é observada na mesma região onde se observam os valores mais elevados do Ekman "pumping", próximo a CSV. O ajuste dinâmico dessa depressão do nível do mar poderá ser o responsável pelo desenvolvimento do vórtice ciclónico e também das PFs frequentemente observados ao longo da NMGoC.

O Capítulo 4 explora um extenso conjunto de dados de ADCP (16 fundeamentos; 34.121 registos horários) coletados na mesma amarração a 23 m de profundidade com o objetivo de obter informações sobre os principais forçamentos das CCCs. O estudo é baseado em parâmetros que descrevem a estrutura vertical do escoamento no momento de mudança de direção. Os resultados mostram que os escoamentos apresentam padrões gerais contrastados consoante a sua direção. Embora 70% das CCCs sejam gerados em condições de vento favoráveis, esses escoamentos geralmente se desenvolvem através das camadas junto ao fundo, principalmente durante o verão. Este facto indica que ventos de leste não é o principal factor que promove as CCCs na maioria dos casos, uma vez que as correntes não se desenvolvem pelas camadas superficiais com tanta frequência. A estrutura geral das CCCs durante o seu desenvolvimento sugere fortemente que a força dominante que compete com o efeito do vento é um gradiente horizontal de pressão ao longo da costa (APG). A existência deste forçamento também é reforçada por uma análise do balanço de momento linear.

Contents

List of Figures

List of Tables

List of Abbreviations

ADCP	Acoustic Doppler Current Profiler
APG	Alongshore Pressure Gradient
CCCs	Coastal Counter Currents
CSM	Cabo de Santa Maria
CSV	Cabo de São Vicente
DINEOF	Data Interpolating Empirical Orthogonal Functions
EF	Equatorward to Poleward Flow Reversal
EFs	Equatorward Flows
EkP_T	Integrated Ekman Pumping velocities
Ek_T	Ekman Transport, Cross-shore Component
$\overline{Ek_T}$	Ekman Transport (vector)
EOF	Empirical Orthogonal Functions
GCC	Gulf of Cadiz Current
HFR	High-Frequency Radar
NMGoC	Northern Margin of the Gulf of Cadiz
PCA	Principal Component Analysis
PE	Poleward to Eastward Flow Reversal
PFs	Poleward Flows
PVD	Progressive Vector Diagram
RIMC	Region of Intensified Mean Currents
SBC	Santa Barbara Channel
SST	Sea Surface Temperature
SLA	Sea Level Anomaly

u_{bed}	Near Bed Flows
u_{surf}	Near Surface Flows
V_{al}	Alongshore Velocity
V_{cr}	Cross-shore Velocity
VRSA	Vila Real de Santo António
w_{Ek}	Vertical Velocities Due to Ekman Pumping

Chapter 1 - Introduction

The eastern North Atlantic water circulation is dominated by the dynamic interaction between the atmosphere and the ocean. The region is under the influence of the Azore high-pressure cell (Chase, 1951) which produces dominant northerly winds along the Iberian – North African western façade during, at least a substantial part of the year. Together with the Earth rotation effect, this atmospheric setup results in a generalized equatorward upwelling circulation marked by cold coastal water between Cape Finisterre, at 43ºN, and Senegal, at 12ºN (see Figures 1.1a and 1.1b, Kämpf and Chapman, 2016; Benazzouz et al., 2014; Arístegui et al., 2009). This region is called the Canary Current Upwelling System (CCUS), which is part of the Eastern Boundary Upwelling Systems (EBUS) of the world, along with the California, Benguela and Humboldt/Peru upwelling systems which share many oceanographic characteristics. EBUS play an important role in the biogeochemical cycles of the ocean and are among the most productive regions of the world (Kämpf and Chapman, 2016). The CCUS is particularly interesting as it is the only EBUS with a significant disruption of the coastline orientation, imposed by the Gulf of Cadiz, and that exchanges water with an adjacent sea, the Mediterranean.

The Gulf of Cadiz is an embayment of Atlantic waters located between the SW tip of the Iberia Peninsula and the NW African coast. The initial process related to the Mediterranean outflow (MOW) into the Atlantic takes place along the northern margin of the Gulf of Cadiz (NMGoC) that is delimited by Cape São Vicente (CSV) at west and the Strait of Gibraltar at east (See Figure 1.1). The Strait of Gibraltar has a width less than 14 km and a minimum depth of 270 m at the Camarinal Sill (Gómez, 2003; García-Lafuente et al., 2011). There, the exchange of the Mediterranean and Atlantic waters takes place in a two-layer flow with Mediterranean waters flowing below (Wesson and Gregg, 1994). The adjustment of the denser Mediterranean outflow (MOW) to the gravity field leads to its abrupt sinking along the NMGoC continental slope as a narrow gravity current. On its descent, the MOW split into an upper and a lower branch with different densities centred near 800 m and 1200 m, as indicated in Figures 1.2a and 1.2b by salinities >35.90 and >36.30 respectively. At these depths and far from the strait, the MOW becomes neutrally buoyant due to a decrease in salinity mainly from the entrainment of the fresher North Atlantic Central Water (Ambar et al., 2002). West of CSV, the outflow spreads

over the eastern North Atlantic Basin (Iorga and Lozier, 1999) and further west, reaching as far as the western North Atlantic (Figure 1.2c, McDowell and Rossby, 1978; Reid, 1978). Thus, the MOW is an important contributor to the salinity input in the North Atlantic (Lozier et al., 1995; Reid, 1978; Iorga and Lozier, 1999), and impacts the global climate due to its interference with the Atlantic Meridional Overturning Circulation (AMOC, Reid, 1979; Mauritzen et al., 2001; Ivanovic et al., 2014).

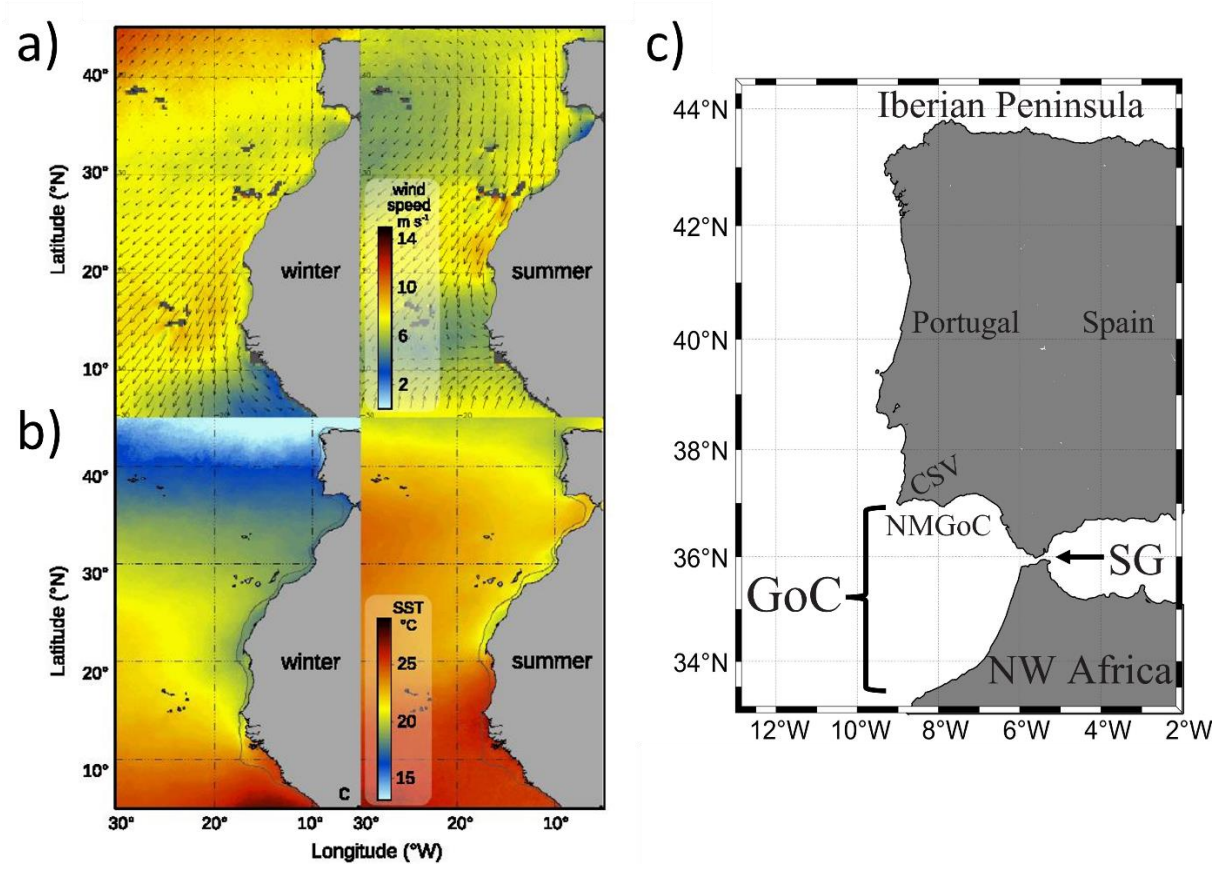

Figure 1.1 - Winter and Summer climatology from QuikSCAT (1999 - 2009) wind (a), and AVHRR (1982 - 2011) sea surface temperature with the 200 m isobath superimposed (b) from Benazzouz et al., (2014). (c) Geographical setting of the Northern margin of the Gulf of Cadiz (NMGoC). CSV: Cape São Vicente, SG: Strait of Gibraltar.

Although much effort has been made to study the dynamics and pathways of the Mediterranean waters along the NMGoC, much less effort was dedicated to the circulation above the MOW, especially over the shelf region. The western region of the NMGoC is at the southern limit of the Portuguese branch of CCUS and is described to be highly affected by mesoscale features

such as filaments, meanders, and eddies that have a profound impact on the local ecosystem functioning (Relvas and Barton, 2002; García Lafuente and Ruiz, 2007; Sánchez and Relvas, 2003). In addition, the NMGoC region hosts a series of socio-economic activities such as fishing (Bueno-Pardo et al., 2017), aquaculture, and tourism (do Valle et al., 2012) that are important to the local economy (Ortega et al., 2013). Understanding the main water circulation patterns in the upper layers of the NMGoC is essential to support the management of socio-economic activities and the marine ecosystem. Furthermore, the existence of a busy maritime route offshore (Figure 1.3) that connects northern Europe with the eastern Mediterranean, poses a risk regarding the spilling of hazardous substances carried on large tankers.

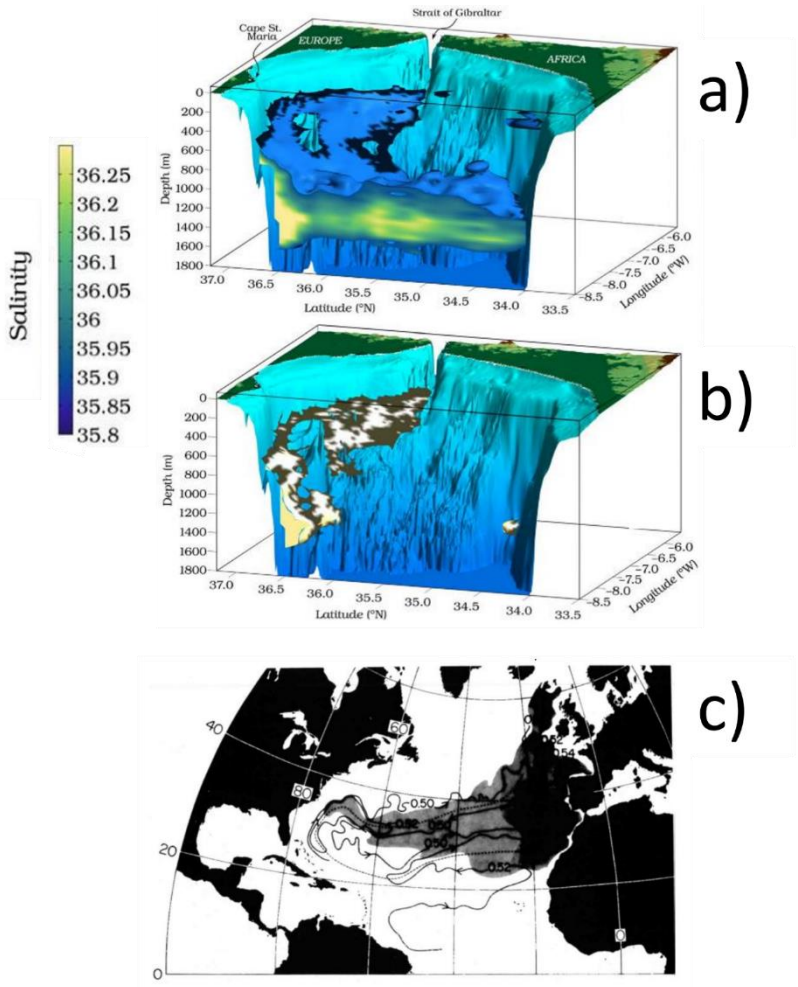

Figure 1.2 - a) Three-dimensional view of the 35.90 isohaline as a buoyant, salty plume abutting the slope. b) As in (a) but for the 36.30 isohaline adapted from Sánchez-Leal et al. (2017). c) Wedge of saline water >35.1 ‰ at a water depth of 1000 m represented by the grey area, adapted from Reid (1978).

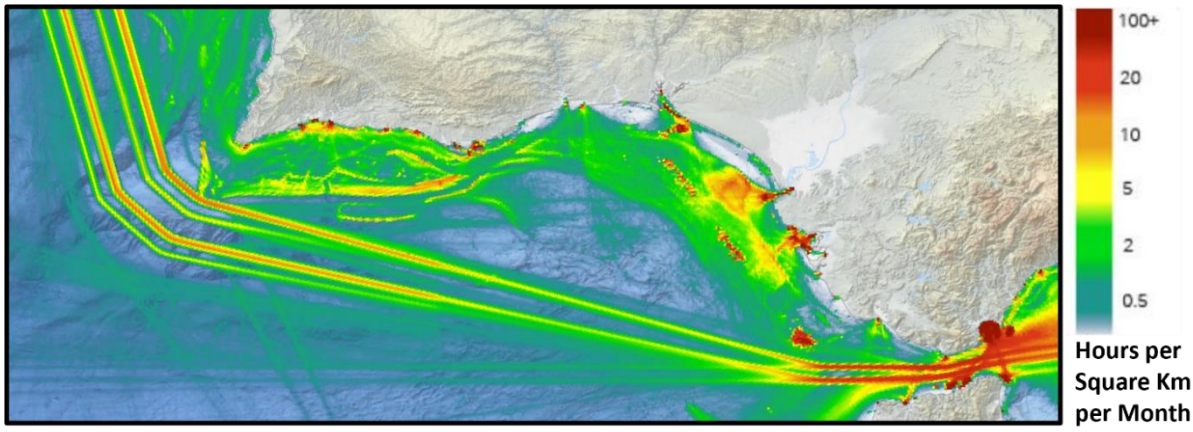

Figure 1.3 - Annual average vessel density considering all types of vessels during 217-2021. Source emodnet.ec.europa.eu

Even though the water circulation at the NMGoC is directly linked with important ecological and economical activities, it is surprisingly poorly known, and the scientific literature is marked by a lack of consensus regarding several aspects of the physical processes involved. For example, off the shelf, the circulation is marked by the presence of the Gulf of Cadiz Current (GCC, following the terminology of Peliz et al., 2007), which contributes to the inflow of Atlantic waters into the Mediterranean (Peliz et al., 2009a, 2007; García-Lafuente et al., 2006), see core N2 in Figure 1.4a. The GCC is often identified based on the cold sea surface temperature (SST) signal along the shelf and slope (Figure 1.4b) suggesting that it is an upwelling jet proceeding from the Portuguese west coast, that may merge with locally upwelled waters (Fiúza, 1983; Folkard et al., 1997; Relvas and Barton, 2002; Stevenson, 1977). However, numerical model results suggest that the entrainment of Atlantic waters by the MOW is able to produce the pressure gradient needed to drive the GCC rather than a direct influence of the wind and upwelling process (Peliz et al., 2009a, 2007).

Over the shelf, the coastal circulation is described to be dominated by the alternation of eastward and westward alongshore flows (Relvas and Barton, 2002), referred to as equatorward flows (EFs) and poleward flows (PFs), respectively. EFs are expected to be broadly wind-driven as they are generally associated with upwelling events (Fiúza et al., 1982; Relvas and Barton, 2005, 2002) but a detailed characterization and their relations with the wind forcing have not been explored so far. PFs are often considered to be coastal counter currents (CCCs) as they are

associated with warm water signal that often replaces the more dominant cold signal associated with EF (Relvas and Barton, 2002; Fiúza, 1983). However, a definition for the CCCs at the NMGoC based on the spatial structure of the flow would be more accurate. The mechanisms that create the CCCs in the NMGoC are also largely speculative. On the one hand, a numerical study suggests that favourable winds are essential to generate intense and realistic CCCs (Teles-Machado et al., 2007). On the other hand, some authors argue that they are most likely to be driven by an alongshore pressure gradient possibly generated by the effect of thermal expansion of warm waters at east (García-Lafuente et al., 2006) or by the effect of the large-scale wind heterogeneity and dissimilar upwelling favourable wind pattern around CSV (Sánchez et al. 2006).

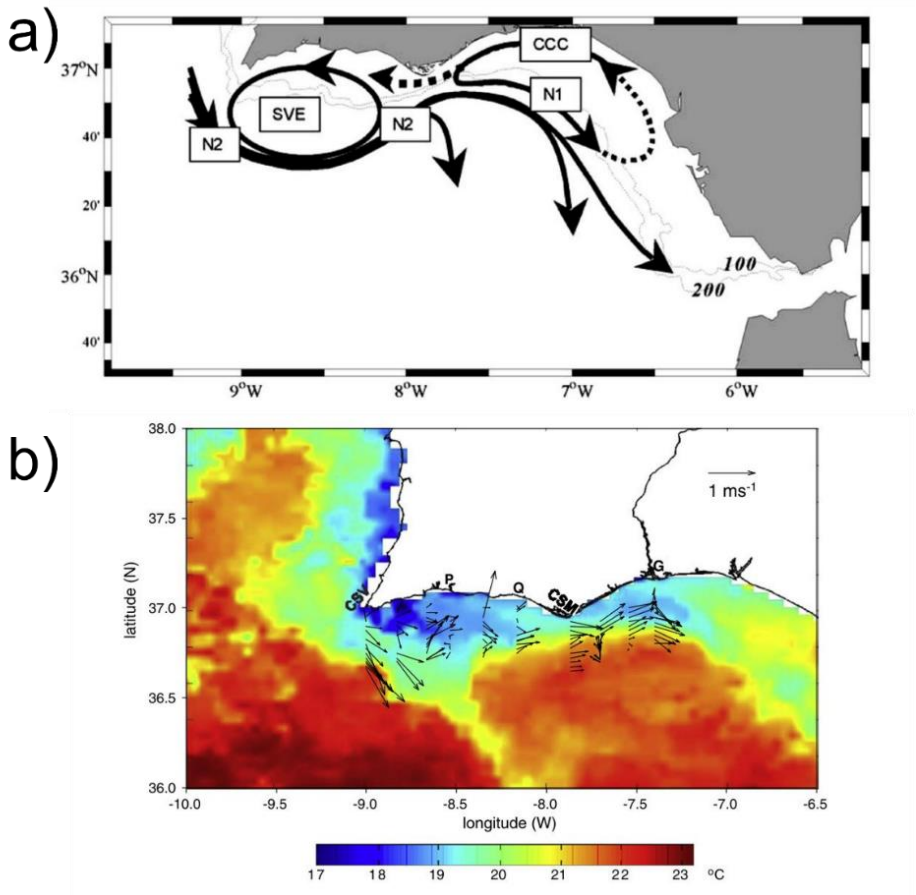

Figure 1.4 - a) Sketch of the surface circulation in the Gulf of Cádiz as deduced from multiple hydrographic surveys in Garcia-Lafuente et al. 2002. Core N2 is a branch of the larger-scale Portuguese–Canary Eastern Boundary Current that veers eastward into the Gulf of Cádiz to feed in part the Atlantic inflow into the Mediterranean through the Strait of Gibraltar. b) Sea surface temperature satellite image, with the upper layer ADCP velocity vectors superimposed, adapted from Cravo et al. 2013.

It is noted that the hypothesis presented by the existing literature are supported by relatively few direct observations, limited in time (mostly in spring and summer) and space (single points or few transects) providing an incomplete description of the general circulation pattern and its seasonal variability. Therefore, the identification of the main drivers of these flows requires the application of a physical approach relying on long-term current observations at some key locations and the integration of various potential environmental forcing parameters. In the present Thesis a novel set of current velocities observations that includes multi-year (from 2008 to 2019) acoustic Doppler current profiler (ADCP) vertical profiles at 5 different locations and 4.5 years (2016-2020) of surface velocities from high-frequency radars (HFR) is exploited to complement the understanding of the ocean circulation along the NMGoC between 9ºW and 7ºW approximately. The central objective of this work is to update the knowledge about the circulation patterns and to postulate explanations for the dynamics involved.

The work developed and the achievement of the proposed objective is presented in this Thesis as three main chapters organized in the form of independent research articles which are summarized below. The Thesis closes with a conclusion section that integrates the main findings and sheds light on future work.

Chapter 2. Kinematics of surface currents at the northern margin of the Gulf of Cádiz

This chapter addresses the characterization of the surface circulation main patterns carried out using 4.5 years of surface velocities from HFR covering most of the shelf and slope region. The velocities from radar were complemented and validated using long-term (2008-2019) velocity data from ADCPs at multiple locations. The integration of all patterns from observations provided a holistic understanding of the circulation at various temporal and spatial scales resulting in an updated conceptual model of the dominant circulation patterns in the NMGoC. The content of Chapter 2 was published in Ocean Sciences as ***de Oliveira Júnior, L., Relvas, P., and Garel, E. 2022. Kinematics of surface currents at the northern margin of the Gulf of Cádiz, Ocean Sciences, 18, 1183–1202.***

Chapter 3. Upwelling processes variability and water circulation along the Northern Margin of the Gulf of Cadiz

High-resolution modelled winds were used to assess the wind forcing effect and its impact on the water circulation based on the characterization of the Ekman transport and Ekman pumping

mechanisms. A seasonal wind regime characterization is provided and comparisons between the different upwelling processes with ancillary SST, sea level anomaly and currents observations data from HFR and ADCP evidenced how the circulation at the NMGoC is affected by the atmosphere-ocean interaction. More specifically, how the modulation of the pressure field is induced by spatially and temporally variable upwelling processes. The content of Chapter 3 was submitted to Continental Shelf Research as ***de Oliveira Júnior, L., Relvas, P., and Garel, E. 2023. Upwelling processes variability and water circulation along the Northern Margin of the Gulf of Cadiz.***

Chapter 4. The structure of incipient coastal counter currents in South Portugal as indicator of their forcing agents

Insights about the main drivers of CCCs are presented in this chapter based on kinematic parameters describing the structure of the flow when it changes direction. The parameters were derived from an extended ADCP dataset (16 deployments; 34,121 hourly records) collected at a single bed mooring (23 m water depth). Based on the characterisation of the general structure of incipient CCCs, the dominant driving forces were inferred and further supported by an analysis of the depth-averaged momentum equation. The content of Chapter 4 was published in the Journal of Marine Systems as ***de Oliveira Júnior, L., Garel, E., and Relvas, P. 2021. The structure of incipient coastal counter currents in South Portugal as indicator of their forcing agents, Journal of Marine Systems, 214, 103486.***

Chapter 2 - Kinematics of surface currents at the northern margin of the Gulf of Cádiz

Abstract

The subtidal surface water circulation at the northern margin of the Gulf of Cadiz, at the southern extremity of the Iberian upwelling system, is described based on validated hourly high frequency radar measurements from 2016 to 2020. Statistical analyses (mean, standard deviation, eccentricity and empirical orthogonal functions) are applied to the dataset, which is completed with ADCP time-series from multiple moorings at 5 inner-shelf stations and ERA5 wind. Off the shelf, the main circulation pattern consists of a slope current, best developed in summer when north-westerlies dominate, in particular at the most exposed western region. Other mechanisms than upwelling must contribute to this flow in order to explain its seasonal persistence. The slope circulation reverses for regional wind events with east component >10 $m.s^{-1}$, approximately. On the shelf, currents are mainly alongshore and balanced. The circulation is generally continuous along the coast, except for weak (<0.1 $m.s^{-1}$, broadly) poleward flows. In the latter case, the flow tends to remain equatorward near Cape Santa Maria. In winter, coastal poleward flows often extend over the entire margin and are mainly wind-driven. In summer, these flows generally consist of coastal counter currents (CCCs) with poleward direction opposed to the one of the slope current. The CCCs are associated with significant cyclonic recirculation, strongest at West, where a transient eddy is shortly observed for weak wind stress. This circulation develops after periods of strong north-westerlies, supporting that CCCs result from the unbalance of a regional along-shore pressure gradient.

2.1 Introduction

The northern margin of the Gulf of Cadiz (NMGoC), along the southwest coast of the Iberian Peninsula, is characterized by a complex water circulation related to its geographic setting. The region is bounded at west by the Portuguese branch of the Canary Current Upwelling System

and, at east, by the Strait of Gibraltar where important water exchange and mixing occur between Atlantic and Mediterranean waters (García-Lafuente et al., 2011; Price et al., 1993). The water circulation at the NMGoC is influenced by these remote forcings together with regional wind conditions producing coastal upwelling and associated mesoscale structures (Criado-Aldeanueva et al., 2006a; Relvas and Barton, 2002; García-Lafuente et al., 2006; Peliz et al., 2007; Sánchez et al., 2007). Understanding the main circulation patterns is essential to support the management of socio-economic activities and of the marine ecosystem. In particular, fisheries and coastal tourism have a considerable weight in the region (Ortega et al., 2013) and some spots on the shelf have been recognized as biodiversity sanctuaries (Boavida et al., 2016). The offshore region is also a busy maritime route (Nunes et al., 2020) for large tankers that pose a risk regarding hazardous substances spill. However, available studies about the coastal and shelf circulation are supported by relatively few direct observations, mostly in spring and summer, and provide an incomplete description of the general circulation pattern and its seasonal variability.

The large-scale surface circulation at the NMGoC has been mainly assessed from sea surface temperature (SST) satellite imagery (Fiúza et al., 1982; Folkard et al., 1997; Relvas and Barton, 2002; Stevenson, 1977; Vargas et al., 2003) and CTD measurements (Criado-Aldeanueva et al., 2006a; Garcia et al., 2002; Sánchez and Relvas, 2003). These data limit the scope of investigation to water masses having a significant temperature contrast and to geostrophic flows. In situ velocity measurements were obtained from few cross-shelf ADCP transects (Cravo et al., 2013; García-Lafuente et al., 2006; García Lafuente and Ruiz, 2007; Relvas and Barton, 2005) and week-to-months long seabed moorings at the eastern part of the inner-shelf (Criado-Aldeanueva et al., 2009; de Oliveira Júnior et al., 2021; Garel et al., 2016; Prieto et al., 2009; Sánchez et al., 2006). Besides, numerical models have been developed to investigate the wind-driven coastal circulation (Teles-Machado et al., 2007) and the hydrodynamic effects in the region of the water exchange with the Mediterranean Sea (Kida et al., 2008; Peliz et al., 2013, 2009a, 2007).

From the above studies, the subtidal inner-shelf (or coastal) circulation is generally described as being dominated by alongshore flows with opposed direction and contrasted temperature in summer, with variations up to 2°C per day (Garel et al., 2016). Cold equatorward flows (EFs, broadly eastward) are generally associated to upwelling events (Fiúza et al., 1982; Relvas and

Barton, 2002, 2005) while warm poleward flows (PFs, broadly westward), often referred to as coastal counter currents (CCCs), develop when upwelling favourable winds relax or reverse (de Oliveira Júnior et al., 2021; Garel et al., 2016; Relvas and Barton, 2002; Sánchez et al., 2006; Teles-Machado et al., 2007). Observations from ADCP moorings at the eastern inner-shelf indicate that the coastal flow is highly polarized, switching semi-weekly between equatorward and poleward without clearly predominant direction during the year (de Oliveira Júnior et al., 2021; Garel et al., 2016). Cross-shelf transects further suggest that in spring and summer the CCCs constitute the northern branches of cyclonic cells that occupy the whole margin (García-Lafuente et al., 2006). At the southern boundary of the shelf, over the shelf slope, the upper layer circulation is dominated by a permanent strong eastward current (Criado-Aldeanueva et al., 2006a; García-Lafuente et al., 2006; García Lafuente and Ruiz, 2007; Peliz et al., 2009a, 2007; Relvas and Barton, 2002, 2005; Sánchez and Relvas, 2003) associated to a cold SST signal in summer which is typical of upwelling events (Fiúza, 1983; Folkard et al., 1997; Relvas and Barton, 2002; Vargas et al., 2003). This feature has been termed a "slope current", not in the sense of JEBAR driven (Simpson and Sharples, 2012) but that it is somehow constrained by the slope bathymetry (Peliz et al., 2009a, 2007; Relvas and Barton, 2002; Sánchez and Relvas, 2003).

To contribute to the knowledge of the water circulation at the NMGoC, the present study addresses the kinematics of surface currents based on 4.5 years (February 2016 - October 2020) of hourly measurements from the South Iberian High Frequency Radar (HFR) system. The analysis allows the establishment of the main circulation patterns and its variability. Special attention is paid to the distribution and seasonality of the coastal and slope flows and to their linkage through cross-shore recirculation in relation to wind conditions. The results provide a detailed characterization of the surface circulation at the NMGoC and some insights about their driving processes.

2.2 Study Area

2.2.1 Geographical Setting

The NMGoC lies along the southern Atlantic coast of Portugal and Spain. It extends from Cape São Vicente (CSV), where the coastline orientation changes from meridional to zonal at the southwest of Portugal, to the Strait of Gibraltar at east (Figure 2.1). The margin consists of two distinct physiographic regions separated by Cape Santa Maria (CSM) where the shelf is the narrowest (5 km-wide): a western bight, characterized by a relatively narrow shelf (<30 km) with a steep slope; and an eastern bight where the shelf is comparatively wider (>40 km) and the slope is gentler (Figure 2.1). The shelf break is at about 200 m in depth. The few rivers flowing into the NMGoC are mainly located at east (e.g., the Guadiana, Tinto-Odiel and Guadalquivir in the study area; Figure 2.1) and feature a low freshwater discharge throughout the year due to the semi-arid regional climate and to strong river flow regulation by dams (Díez-Minguito et al., 2012; Garel and D'Alimonte, 2017).

2.2.2 Circulation Patterns

Coastal upwelling generally occurs from April to September along the west coast of Portugal due to the predominance of northerlies(Alvarez et al., 2008; Fiúza et al., 1982). As the coastline sharply changes its orientation, northerlies rotate counterclockwise around CSV due to a low-pressure cell centred over the Iberian Peninsula and to orographic constraints induced by the presence of a coastal mountain range (Fiúza, 1983; Relvas and Barton, 2002).The westerly component of the rotated wind may promote coastal upwelling along the NMGoC until 7°15'W approximately, being generally more pronounced at the capes (CSV and CSM) (Criado-Aldeanueva et al., 2006a; Relvas and Barton, 2002). These events generally last for few days only, such as the NMGoC has been described as a region with episodic upwelling events rather than a typical upwelling region (such as western Iberia) where upwelling persists during a substantial part of the year, at least (Garel et al., 2016).

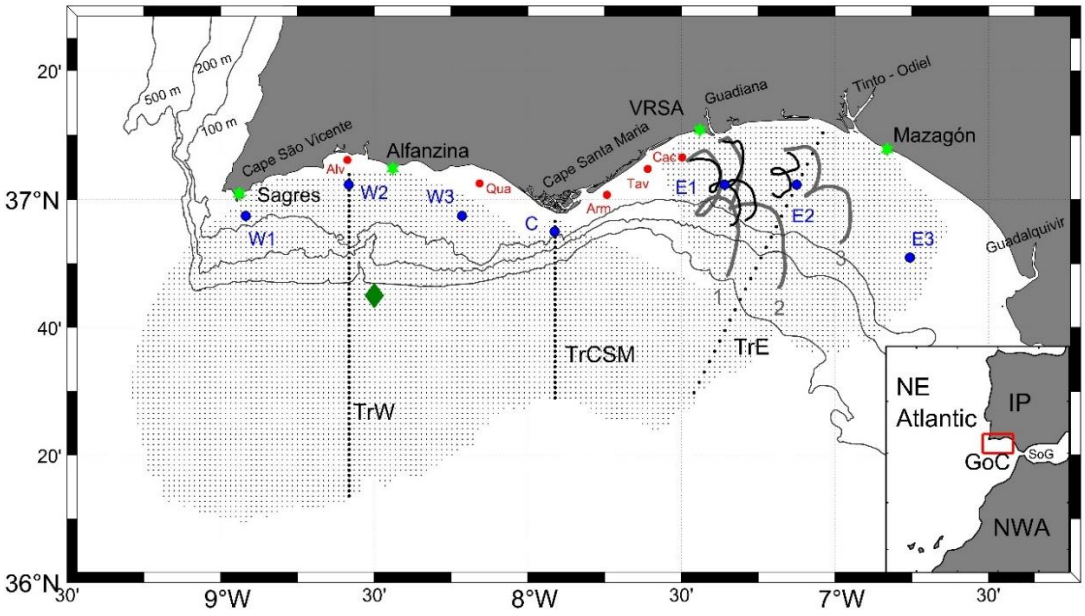

Figure 2.1 - Study area with location of the HFR antennas (green stars, with VRSA: Vila Real de Santo Antonio), ADCP mooring (red dots, with Alv: Alvor, Qua: Quarteira, Arm: Armona, Tav: Tavira, Cac: Cacela.), HFR grid nodes with ≥ 60% of measurements (thin black dots) along with the transects (TrW, TrCSM and TrE indicated as thick black dots) and grid nodes (W1, W2, W3, C, E1, E2, E3, thick blue dots) analysed in the study. The thick grey and black lines represent the drifters' trajectories and corresponding PVD from HFR data, respectively (see section 2.4). Dark green diamond indicates the point where wind from ERA5 reanalysis was extracted (Section 2.6.1). The isobaths of 100, 200 and 500 m are represented as thin black lines. For general location, see inset (IP: Iberian Peninsula; NWA: Northwest of Africa; GoC: Gulf of Cadiz and SoG: Strait of Gibraltar).

The equatorward upwelling jet over the western Portugal shelf tends to follow the coast around CSV and to merge with locally upwelled water at the NMGoC (Relvas and Barton, 2002, 2005; Sánchez and Relvas, 2003). There, the flow typically corresponds to a band of cold SST along the shelf and its slope (Fiúza, 1983; Folkard et al., 1997; Relvas and Barton, 2005; Stevenson, 1977; Vargas et al., 2003) which eastward extension is promoted by favourable (westerly) wind (Criado-Aldeanueva et al., 2006a; Vargas et al., 2003). Velocity measurements have confirmed that this cold-water band is associated with eastward currents, having relatively strong near-surface velocities (>0.25 $m.s^{-1}$) along the slope (Cravo et al., 2013; García-Lafuente et al., 2006; Peliz et al., 2009a; Relvas and Barton, 2005). Over the western bight, this current has been observed up to 300 m in depth and to extend significantly offshore from the slope in summer (García-Lafuente et al., 2006). At CSM, the slope current approaches close to the coastline due

to the narrowness of the shelf (Cravo et al., 2013; Criado-Aldeanueva et al., 2006a). Over the eastern bight, the flow has been reported during all seasons and veers anticyclonically following the slope orientation (Figure 2.1; Criado-Aldeanueva et al., 2009, 2006; Fiúza, 1983; Garcia et al., 2002; Peliz et al., 2007, 2009a; Relvas and Barton, 2002; Sánchez and Relvas, 2003). Measurements from ADCP moorings suggest that, at a sub-monthly scale, these flows reverse predominantly in winter and are wind-driven (Criado-Aldeanueva et al., 2009). In addition, numerical model results support that the Mediterranean inflow-outflow coupling contribute significantly to the development of the slope current through an entrainment process (Peliz et al., 2009, 2007). These authors proposed to name this current the Gulf of Cadiz Current (GCC).

Over the inner-shelf, the polarized alongshore subtidal circulation (de Oliveira Júnior et al., 2021; Garel et al., 2016) is well-evidenced on SST images from spring to autumn due to strong thermal contrast (Fiúza, 1983; Folkard et al., 1997; Relvas and Barton, 2002). The upwelled cold water is frequently displaced offshore by a narrow band of warm water, about 10-20 km wide, leaning along the coast. This warm water signal originates from the region of the Guadalquivir mouth (Figure 2.1) and propagates westward depending on the strength and duration of easterlies, rarely reaching the West coast at north of CSV (Fiúza, 1983; Relvas and Barton, 2002). The corresponding PFs (so-called CCCs) are produced by the unbalance of an alongshore pressure gradient during the relaxation (or reverse) of upwelling favourable winds (de Oliveira Júnior et al., 2021; García-Lafuente et al., 2006; Garel et al., 2016; Relvas and Barton, 2002) and are enhanced by easterlies (Teles-Machado et al., 2007). ADCP measurements at the eastern inner-shelf show that EFs and PFs occur equally along the year, reversing direction every 4 days in average (de Oliveira Júnior et al., 2021; Garel et al., 2016). Cross-shelf ADCP transects (García-Lafuente et al., 2006) and a spring-summer climatological analysis of the geostrophic surface circulation based on historical (1900-1998) CTD data (Sánchez and Relvas, 2003) suggest the existence of two cyclonic cells centred over the eastern and western bights, connecting the slope and coastal flows.

2.3 Data and Methods

2.3.1 HFR, ADCP and Drifter Data Sets

The study area is equipped with four CODAR medium range SeaSonde HFR antennas located in Sagres, Alfazina, Vila Real de Santo Antonio (VRSA) and Mazagon (Figure 2.1, green stars), as a result of a collaboration between Puertos del Estado (Spain) and Instituto Hidrográfico (Portugal). The system operates at 13.5 MHz, providing hourly radial surface velocities with spatial resolution of approximately 1.5 km up to 60 km from the coast (CMEMS Service Evolution, 2017). Each antenna measures the velocity towards or away from it; thus, at least two antennas are required to compute the total velocities (zonal and meridional components) through least squares fitting (Lipa and Barrick, 1983; Paduan and Washburn, 2013). At regions where the radials from two antennas make an angle $\leq 20°$, the orthogonal velocity component cannot be estimated accurately (Chapman et al., 1997; Paduan and Washburn, 2013) and is estimated from adjacent valid measurements (i.e., with radial angle >20º; CODAR, 2004a, 2004b)

The first pair of HFR antennas, at VRSA and Mazagon, was installed in 2013 covering an area restricted to the eastern bight. Alfazina station started operating in November 2014, extending the spatial coverage westward of CSM (up to 8°20'W). In February 2016, the last antenna was installed in Sagres, and full coverage of the western shelf was achieved (Figure 2.1). The dataset analysed in this study corresponds to the period with largest coverage, from February 2016 to October 2020. Earlier data were used for validation.

ADCP records were obtained at 5 moorings stations along the coast (Armona, Cacela, Tavira, Alvor and Quarteira) at water depths of 20-23 m (for location, see red stars in Figure 2.1). A total of 30 deployments, lasting 0.4 to 6 months each, were performed between 2008 and 2019 using Workhorse 600 kHz and Sentinel V 500 kHz ADCPs from TRDI (Figure 2.2). For each deployment, the instrument was installed inside a cubic concrete artificial reef unit (1.4 m side) lying on the bottom, with the sensor head slightly rising out. Velocities were recorded along the water column within cells of 0.5-1 m in thickness (depending on the deployment) with a sampling interval of 60 minutes, at maximum. The standard deviation (STD) of the horizontal velocity resulting from the ADCP setup (number of pings per ensemble, cell size, etc.) was generally less than 0.03 $m.s^{-1}$.

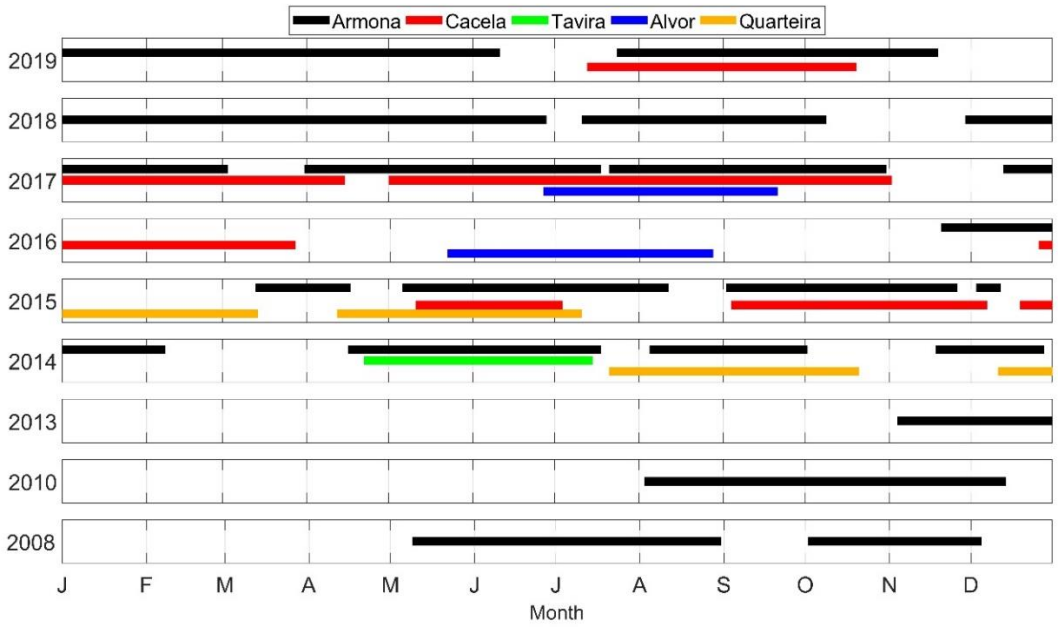

Figure 2.2 - ADCP deployments per month (x axis) between 2008 and 2019 (y axis) at Armona (black), Cacela (red), Tavira (green), Alvor (blue) and Quarteira (orange) stations.

Three Metocean iSPHERE drifters were deployed by Instituto Hidrográfico on 10 May 2013 at 2-8 km from the eastern bight shore, between 7°W and 7°30'W (Figure 2.1). The drifters weight 13.15 kg for a diameter of 34 cm. They have no drogue, making the drift relatively sensible to wind conditions. The drifters' position was recorded every 10 minutes by an internal GPS.

2.3.2 Processing

ADCP data quality was ensured by independent validation of each ensemble following the procedure described in Garel et al. (2016). In particular, the upper cells affected by the surface boundary were removed based on the signal intensity. For this study, only validated near surface cells (generally within the first 2-4 m from the surface) were considered.

The HFR maps with low spatial coverage (<50%) were removed from the time-series. Subsequently, periods with infrequent consecutive maps were also discarded resulting in data gaps ranging from 2 days up to 144 days (see blanks on Figure 2.3a). The zonal and meridional surface velocity components were linearly interpolated at grid nodes with time gaps ≤ 6h. This threshold assures that no excessive interpolation is performed (as the flow generally does not

change drastically during such time interval). It was checked that other interpolation choices do not affect the results.

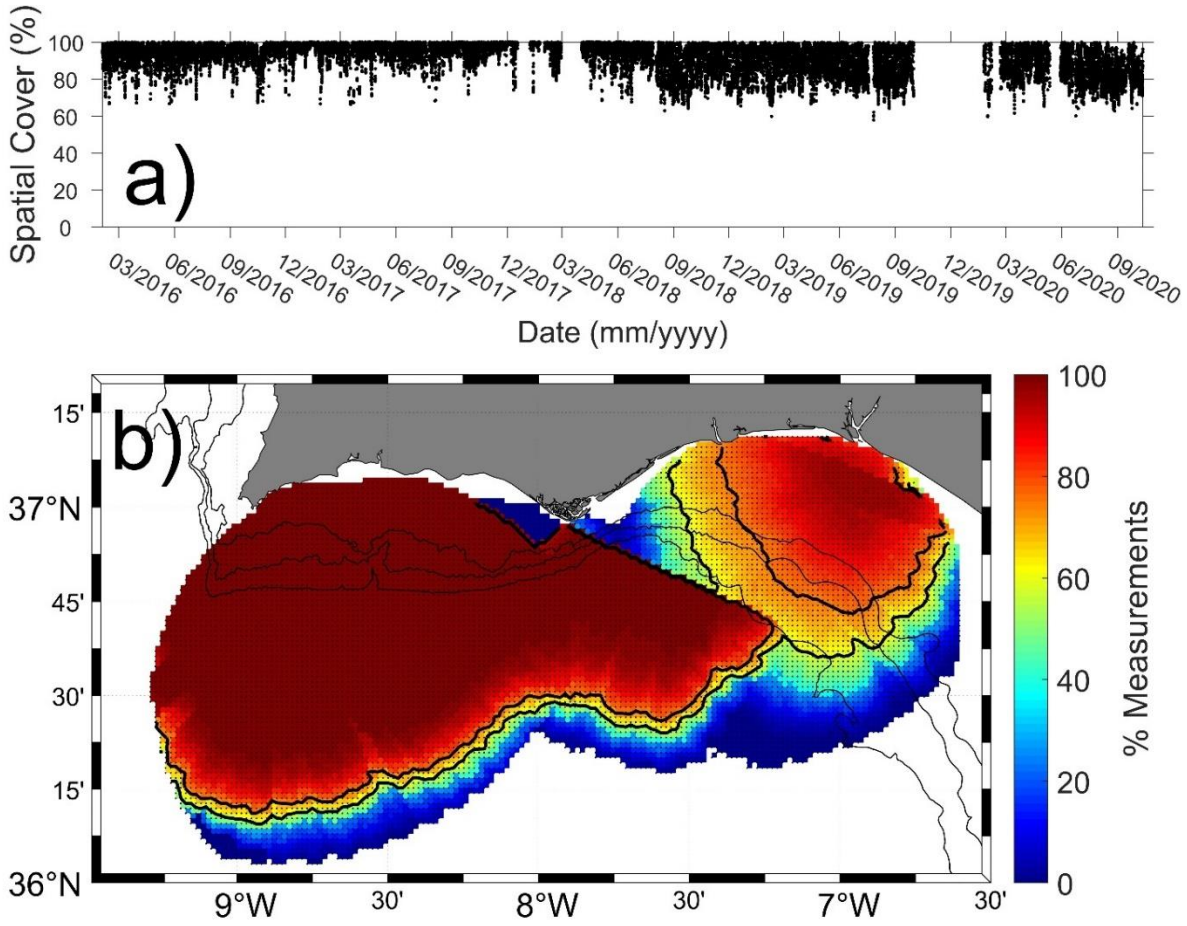

Figure 2.3 - a) Temporal distribution of the spatial coverage area considering grid nodes having at least 60% of records. b) Percentage of data at each grid node with indication of the 60% and 75% isocontours (thick black lines). The isobaths of 100, 200 and 500 m are represented as thin black lines.

The HFR and ADCP velocity components were low-pass filtered with a 4th order Butterworth filter of 40-hour cut-off period. The resulting subtidal (or sub-inertial) zonal (u, positive eastward) and meridional (v, positive northward) velocities are considered hereafter, unless indicated For HFR data, the mean, STD ellipses and eccentricity ($= \frac{\sqrt{a^2-b^2}}{a}$, where a and b are the length of semi-major and semi-minor axis of an ellipse respectively) maps were produced for the region having at least 60% of records at each grid node (Figure 2.3b). This threshold allows considering a large area with few temporal gaps. For instance, the hourly velocity maps

cover at least 80% of the selected area during 90% of the period 2016-2020 (Figure 2.3a). The analysis was performed considering both the whole time series and seasons (defined for simplicity as winter: 1 December-28 February; spring: 1 March-31 May; summer: 1 June 31 August; and autumn: 1 September-30 November).

In order to describe the surface current main variability patterns, an empirical orthogonal function (EOF) analysis was applied to the subtidal HFR data following the techniques described in Kaihatu et al. (1998) and Kundu and Allen (1976). The current field $V(x,t)$, where t is the time and x is the coordinate, is expressed as a complex scalar $V(x,t) = u(x,t) + jv(x,t)$, where $j = (-1)^{0.5}$. The data set V is then decomposed in terms of k spatial and k temporal coefficients (ϕ_k and a_k, respectively where k is an integer that ranges from 1 to the total number of grid nodes):

$$V = \sum_k a_k(t)\phi_k(x)\ , \qquad (1)$$

The spatial and temporal coefficients are complex numbers and are typically represented by their amplitude and phase. Furthermore, the complex eigenfunctions ϕ_k can be decomposed according to the velocity components as $\phi_k = \phi_u^k + \phi_v^k$.

Since EOF requires the dataset to be free of gaps, the velocity components were interpolated using the Data Interpolating Empirical Orthogonal Functions (DINEOF) method presented in (Beckers and Rixen, 2003), which is widely used for filling gaps of satellite derived products (Alvera-Azcárate et al., 2005) and is suitable to the case of HFR data (e.g., Hernández-Carrasco et al., 2018; Kokkini et al., 2014). The DINEOF methodology was performed using unfiltered data, for maps having at least 75% of spatial coverage (against 60% for the mean and STD) to avoid excessive interpolation. The technique consists in subtracting the mean values from each time series and substituting the missing values by zero. Then, an EOF analysis is applied to the demeaned matrix in order to reconstruct the time series based on EOF modes with highest variability. This procedure is performed iteratively, substituting the originally missing values with the estimated ones. The number of iterations and the number of modes to be retained is defined based on statistical convergence (achieved through cross-validation). The final step consists in summing the mean value back to each time series which have then no gap.

The variability of the flow from the coastal to the off-shelf regions (i.e., the region offshore the 200 m isobath, hereafter) was evaluated along transects at the western bight, CSM and eastern bight (TrW, TrCSM and TrE, respectively; thick dotted lines in Figure 2.1). Each transect is approximately perpendicular to the shelf break, which roughly corresponds to the coastline orientation: TrW and TrCSM are N-S, while TrE is NE-SW. The flow is represented by its alongshore (V_{al}) and cross-shore (V_{cr}) components, corresponding to u and v, respectively, for TrW and TrCSM, and to u and v rotated 30° clockwise from east for TrE. The width (i.e., offshore extent from the coast) of EFs and PFs along the transects was quantified considering flows with V_{al} of the same sign at the two most landward nodes, after smoothing out small velocity fluctuations with a 5-nodes moving average.

The propagation of EFs and PFs along the coast was evaluated considering V_{al} at 3 grid nodes located at a depth of 40 m (W2, C and E3 in Figure 2.1). At these nodes, V_{al} was obtained based on the angle of maximum variance, which closely corresponds to the nearby coastline orientation, as previously reported at inner-shelf mooring stations (de Oliveira Júnior et al., 2021; Garel et al., 2016; Prieto et al., 2009).

2.4 HFR Data Validation

ADCP time series at Alvor, Tavira and Cacela Stations were compared with HFR velocities at the nearest grid nodes to estimate the quality of HFR data near the coast. The selected nodes were located at less than 1 km for Cacela and Tavira (which are both within the HFR coverage area) and at 4 km southward for Alvor. The other stations were not considered as Armona is well outside the HFR coverage area (see Figure 2.1) and Quarteira records (in 2014-2015; Figure 2.2) do not overlap with HFR ones.

The mean ADCP velocity of the flow components is generally close to 0, while the STD of u is one order of magnitude larger than v, confirming that the coastal flow is mainly alongshore and polarized (Table 1). The HFR velocities feature similar characteristics, except at Alvor grid node (where the mean of v is larger than the mean of u) possibly due to the distance between the HFR node and ADCP station. The deployment at Cacela from December 2016 to April 2017 illustrates the good correspondence between HFR and ADCP records and the predominance of the u flow component (Figure 2.4). Overall, the Spearman's correlation coefficient (R) between

HFR and ADCP is very good (0.92) for u and poor for the weak v component (Table 1). The mean of the differences and the root mean square of the differences (RMSd) between HFR and ADCP velocities are small (≤ 0.09 m.s^{-1} and ≤ 0.11 m.s^{-1} respectively). Large differences up to 0.3 m.s^{-1} (Figure 2.4a) are episodically observed. Such differences are expected due to the distinct depth of HFR and ADCP measurements. ADCPs upper measurements are at 2-4 m below the surface, while the radars measure the surface layer (<0.5 m below surface) which is more likely affected by wind drag. Moreover, HFR and ADCP systems have distinct measurement methods (e.g., in terms of horizontal position, footprint, sampling duration and averaging). Despite these inherent differences between both equipment, the correlations between HFR and ADCP velocities support the good quality of the HFR measurements, in particular near the coast. Furthermore, the present skill scores are similar to those obtained at regions with flow velocities similar to the ones at the NMGoC (Lorente et al., 2015).

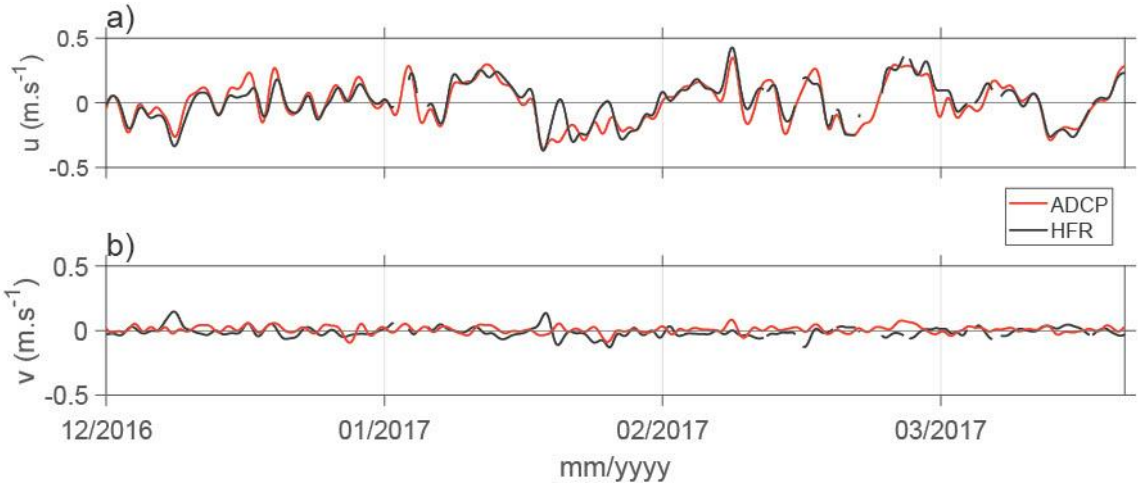

Figure 2.4 - Comparison of the flow velocity (m.s^{-1}) recorded by an ADCP at Cacela station (red lines) with the velocity at the nearest HFR grid node (black lines) from December 2016 to April 2017: a) eastward component u; b) northward component v.

On the shelf, drifter's trajectories were qualitatively compared with HFR trajectories obtained from a progressive vector diagram (PVD) of unfiltered velocities. For statistical comparisons with unfiltered HFR data at the nearest node, drifter's pseudo-Eulerian velocities were derived from the distance between pairs of successive drifter's positions, subsampled at the HFR time, divided by the time interval (1 hour).

The trajectories of the three drifters presented a general southward displacement of 31-45 km affected by clockwise inertial rotation (Figure 2.1, grey lines). Such overall drift was fairly reproduced by the PVDs in all the 3 cases (Figure 2.1, black lines), although they remained closer to the shore than the drifters (in particular when compared with drifter 3). The skill scores between the drifter-derived and HFR flow components is poorer than for HFR-ADCP data (Table 1). Discrepancies between HFR and drifter pseudo-Eulerian velocities are inherent to their distinct acquisition techniques (e.g., spatial averaging of eulerian records for HFR against lagrangian measurements at a point for the drifters and subsequent transformation to pseudo-Eulerian velocities), along with the potential wind drag effect on the emerged part of the drifters. Nevertheless, the results are within the range of what has been reported as satisfactory in other studies comparing HFR currents with various types of drifters (Kaplan et al., 2005; Paduan and Rosenfeld, 1996; Solabarrieta et al., 2014).

Table 2.1 Validation statistics between HFR and in situ (i.e., ADCP, drifter) measurements of the u and v flow components.

In situ observations	Period	Mean (STD) in m.s^{-1}				R		Mean difference (STD) in m.s^{-1} In situ – HFR		RMSd in m.s^{-1} In situ – HFR	
		u in situ	v in situ	u HFR	v HFR	u	v	u	v	u	v
ADCP Cacela	May - Jul 2015	0.01 (0.16)	0 (0.03)	0.04 (0.12)	-0.02 (0.04)	0.92	0.64	-0.03 (0.06)	0.02 (0.03)	0.07	0.03
	Sep - Dec 2015	0 (0.13)	0.01 (0.03)	-0.02 (0.11)	0 (0.03)	0.84	0.33	0.01 (0.07)	0.01 (0.04)	0.07	0.04
	Dec 2015 - Mar 2016	0.07 (0.16)	0.02 (0.03)	0.08 (0.15)	-0.01 (0.03)	0.94	0.19	-0.01 (0.06)	0.02 (0.04)	0.06	0.05
	Dec 2016 - Apr 2017	0 (0.16)	0.01 (0.03)	0.01 (0.15)	-0.01 (0.04)	0.93	0.04	-0.01 (0.06)	0.02 (0.05)	0.07	0.05
	May - Nov 2017	0.02 (0.14)	0.01 (0.03)	0.05 (0.12)	-0.01 (0.03)	0.91	0.38	-0.03 (0.06)	0.02 (0.04)	0.07	0.04
ADCP Alvor	May - Aug 2016	-0.03 (0.09)	-0.01 (0.02)	-0.06 (0.15)	-0.10 (0.06)	0.68	0.14	0.03 (0.1)	0.09 (0.06)	0.11	0.11
	Aug - Sep 2017	-0.03 (0.09)	-0.02 (0.03)	-0.02 (0.1)	-0.06 (0.04)	0.61	0.31	-0.01 (0.08)	0.04 (0.04)	0.08	0.06
ADCP Tavira	Apr - Jul 2014	0.03 (0.15)	0.01 (0.07)	0.08 (0.14)	0.01 (0.09)	0.88	0.31	-0.05 (0.07)	0.01 (0.09)	0.09	0.09
Drifter 1	May 2013	0.08 (0.23)	-0.23 (0.31)	0.01 (0.21)	-0.09 (0.17)	0.86	0.90	0.07 (0.09)	-0.13 (0.18)	0.12	0.23
Drifter 2	May 2013	0.12 (0.21)	-0.29 (0.24)	0.04 (0.15)	-0.18 (0.15)	0.87	0.84	0.08 (0.12)	-0.11 (0.14)	0.14	0.17
Drifter 3	May 2013	0.11 (0.24)	-0.17 (0.22)	-0.03 (0.17)	-0.07 (0.1)	0.96	0.66	0.14 (0.11)	-0.09 (0.17)	0.18	0.19

2.5 Results

2.5.1 Mean Circulation

HFR mean velocities are broadly oriented south-eastward over the study area (Figure 2.5a). This direction generally corresponds to the main variability of the STD (see the elongated ellipses with northwest-southeast orientation in Figure 2.5b), indicating the predominance of south eastward currents through time. At off-shelf regions where the current direction varies importantly, in particular between 8°10'W and 8°20'W and between 7°15'W and 7°30'W (see rounded ellipses and areas with dark blue colours in Figure 2.5b), the mean currents remain south-eastward. At west of 8°45'W, mean currents are towards the south and southwest but vary principally along the northwest-southeast direction. This region is also characterized with strong velocities (see the large STD ellipses in Figure 2.5b). It is noted that some rays emanating from the HFR antennas feature regions with lower eccentricity than the surrounding, suggesting a slight underestimation of one of the flow components.

The main feature revealed in the mean flow is a zonal band with strong velocities (from 0.075 m.s-1 up to 0.15 $m.s^{-1}$), elongating east-west across the whole study area (between 36°30'N and 36°55'N, broadly). This region of intensified mean currents (RIMC, hereafter) includes the shelf slope. At the western bight, the RIMC is broader and presents greater velocities than at the eastern bight; the south-eastward mean currents are oblique with respects to the (east-west) shelf break orientation. The mean flow at the RIMC rotates cyclonically near CSV and is aligned with the shelf slope isobaths at the eastern bight due to the predominance of along-slope currents, as indicated by the STD ellipse orientations.

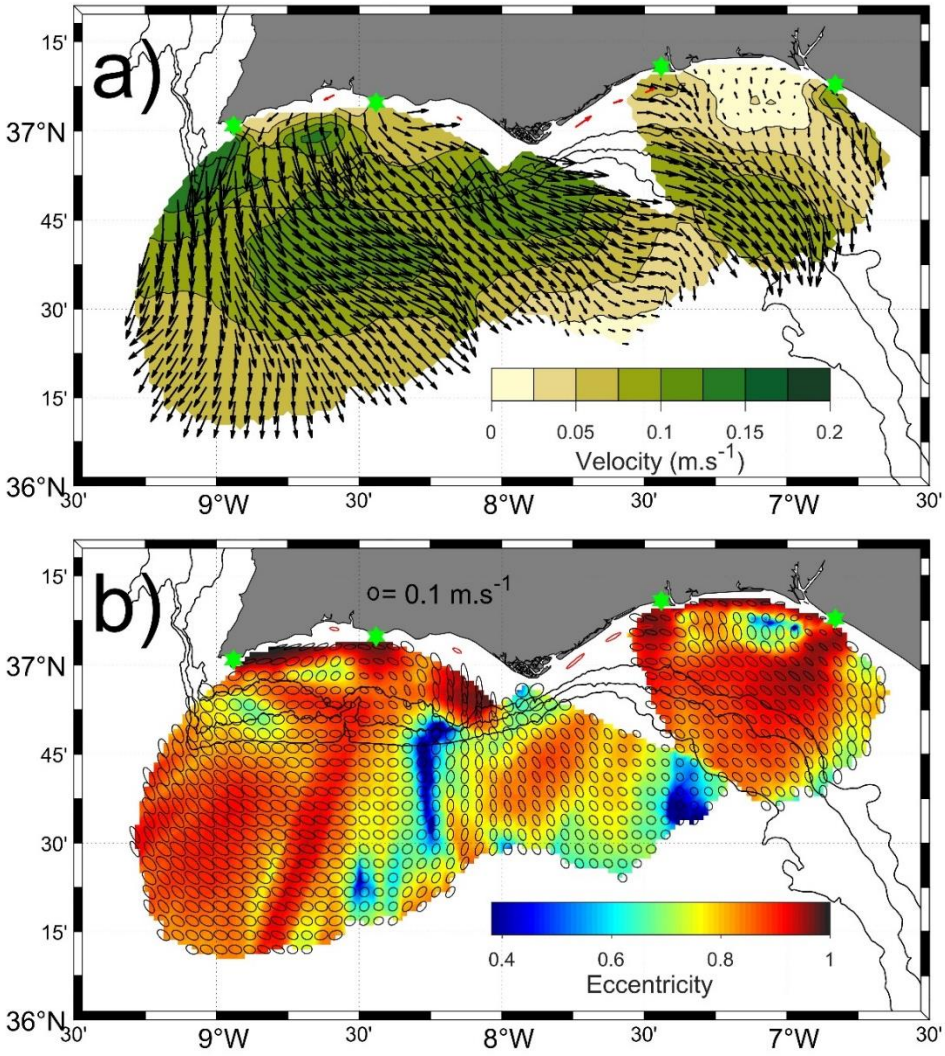

Figure 2.5 - Mean HFR surface velocities (a) and STD ellipses and eccentricity (b) for the period February 2016 - October 2020. For clarity, the ellipses and arrows are represented every three grid nodes. The mean velocity and STD ellipses of ADCP data for the deployment periods and stations indicated in Figure 2.2 are shown in red. The locations of the HFR antennas are indicated with green stars.

A well-defined region of high eccentricity values is observed near the coast (dark red in Figure 2.5b), except in front of CSM. These elongated STD ellipses result from the dominance of alongshore currents. The eccentricity is close to one at coastal regions where the grid nodes and antennas are aligned (e.g., near CSV), due to an underestimation of the orthogonal velocity component (that does not challenge the observed overall predominance of alongshore flows). The mean coastal flow velocity is generally >0.05 $m.s^{-1}$ and equatorward, being poleward only near CSV (Figure 2.5a). This pattern is consistent with the mean ADCP velocities, which are all alongshore and equatorward, except at Alvor station where it is poleward (see red arrows

and red ellipses in Figure 2.5). However, considering the u-component at the 7 selected nodes on the shelf (for location, see Figure 2.1), the relative occurrence of EFs and PFs is balanced, except near CSM and its western flank (Table 2). The strongest mean velocities are observed at the capes (about 0.10 $m.s^{-1}$ at CSM and 0.15 $m.s^{-1}$ at CSV) and also near 8°40'W over the mid-shelf where the flow is offshore (southward). Finally, the shelf between the Guadiana and Tinto-Odiel river mouths is characterized by variable flow directions with balanced magnitude, resulting in the weakest mean flow at the study area (<0.025 $m.s^{-1}$ with STD = 0.15 $m.s^{-1}$). In details, the STD ellipses are elongated alongshore near the coast and along the slope at the shelf break but feature a significant cross-shelf component in between.

Table 2.2. Percentage of occurrence between the eastern (u) component of eastward and westward flows at the selected nodes.

	W1	W2	W3	C	E1	E2	E3
Eastward	48%	59%	80%	77%	60%	52%	59%
Westward	52%	41%	20%	23%	40%	48%	41%

2.5.2 Seasonal Variability

The overall mean current direction and STD patterns (Figure 2.5) remain similar for all seasons, including the coastal alongshore flow delineated by low eccentricity values (Figure 2.6). Seasonality is mainly observed in terms of velocity magnitude at the RIMC over the western bight (Figure 2.6 a-d). There, the RIMC evolves from a narrow (zonal) band with relatively weak mean currents in winter to a wide band (extending significantly off-shelf) of strong mean velocities (up to 0.2 $m.s^{-1}$) in summer. Spring corresponds to an intermediate situation between winter and summer. In autumn, mean currents are the weakest (generally <0.075 $m.s^{-1}$) and the RIMC is poorly expressed.

Over the shelf, the mean currents are dominantly towards the SE in winter and spring (Figure 2.6a, b). In summer and autumn, they describe a cyclonic pattern from CSV (south-westward) to CSM (south-eastward; Figure 2.6c-d). The shelf region with strong southward velocity near 8°40'W (Figure 2.5) is best defined in summer. For all seasons, the largest variability on the shelf (STD >0.2 $m.s^{-1}$) corresponds to EFs at the western flank of CSM (Figure 2.6e-h). By contrast, the mean currents over the east margin (including the RIMC) have a relatively constant magnitude and direction for all seasons. It is noted that the cross-shelf component is enhanced at the eastern limit of the study area.

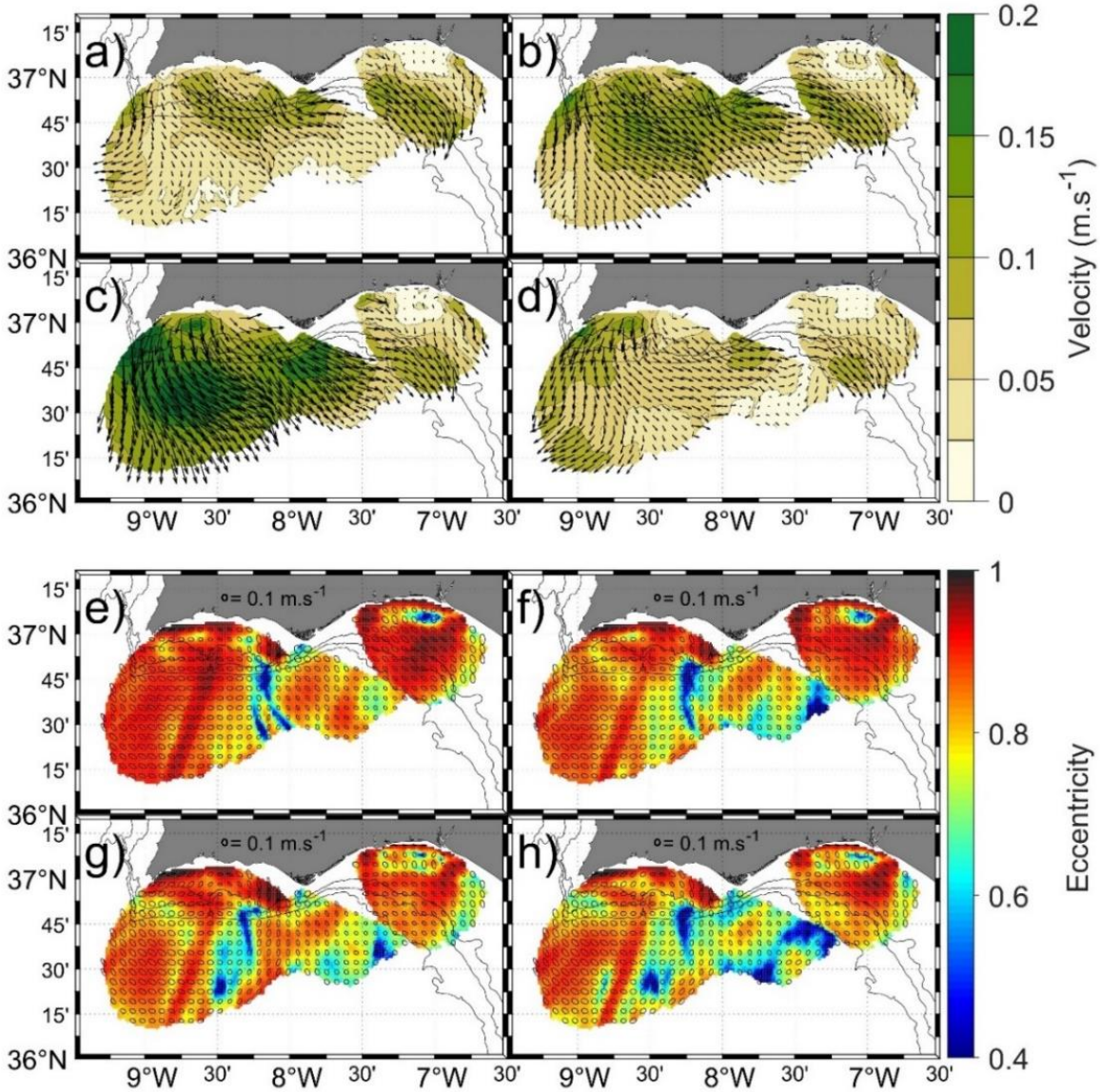

Figure 2.6 - Seasonal mean HFR currents and standard deviation with eccentricity as colour maps in (a, e) winter, (b, f) spring, (c, g) summer and (d, h) autumn for the period February 2016 - October 2020. For clarity, the ellipses and arrows are represented every four grid nodes.

2.5.3 Main Circulation Patterns

Modes 1 and 2 of the complex EOF analysis account for 59% of the data variability (47% and 12%, respectively). The other modes explain no more than 6% each. The dominant spatial pattern described by mode 1 corresponds to EFs over the inner-shelf and south-eastward flows offshore having maximum amplitude at south of CSV (Figure 2.7a). Exceptions to this general pattern occur at west of CSM (southward shelf flows) and from the Guadiana to the Tinto-Odiel River mouths (cyclonic rotation of the coastal flow). Mode 1 circulation is relatively constant through time, as its phase is generally close to 0 (Figure 2.7c). For example, it is between -25° and 25° during 47% of the time, in particular in spring and summer (70%); at that time, the amplitude is also the highest (as illustrated by the low-passed filtered time series in Figure 2.7d), denoting a more vigorous circulation than in autumn and winter. Reversals of spatial mode 1 occur during any season but are relatively rare, the phase being between 155° and 205° during 9% of the time, only (Figure 2.7c-d).

Mode 2 describes a more variable circulation, both spatially and temporally, than mode 1 (Figure 2.7b). Velocity amplitudes are greatest over the shelf (except for the offshore area at south of CSV, as for mode 1). At the western bight, the circulation features a cyclonic cell, about 70 km in diameter, characterized by strong PFs near the coast that recirculate offshore near CSV to merge with the region of maximum amplitude offshore. This circulation pattern occurs mainly (64%) in summer and in autumn, when the phase is dominantly between -25° and 25° (Figure 2.7e). PFs are comparatively weaker at the eastern shelf and are best observed on the outer-shelf rather than inner-shelf. Noteworthy, this flow goes around CSM, thus connecting both shelves. Mode 2 is often out of phase, being for example between 155° and 205° during 48% of the whole time series (against 19% of the time between -25° and 25°), and up to 60% in winter and spring. For approximately 30% of these “out of phase” events in winter and spring, mode 1 is in phase, such as both modes contribute to the development of strong EFs over the shelf and south-eastward flows further offshore.

It is noted that the EOF results remain similar with unfiltered data. In particular, the spatial patterns of modes 1 and 2 are similar than with filtered data and the explained variability is 42% and 9.4%, respectively.

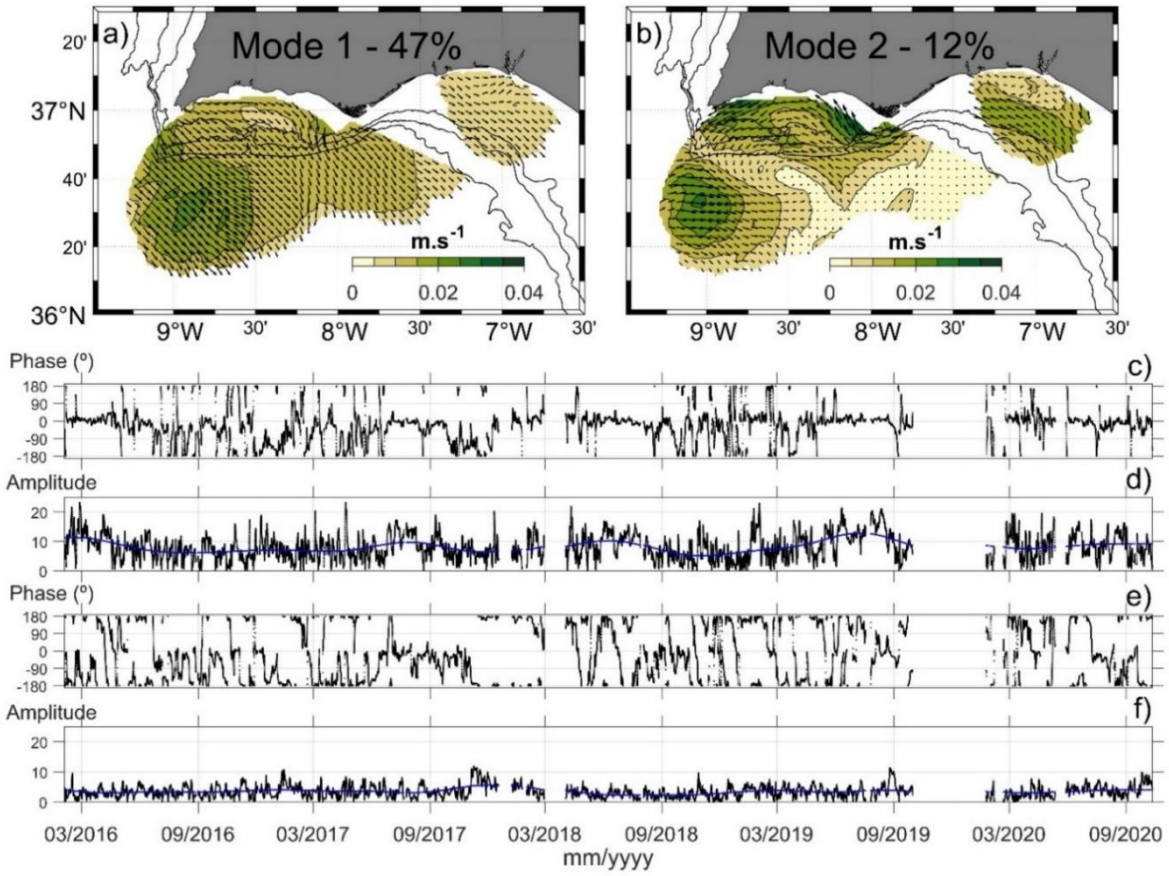

Figure 2.7 - Results of the complex EOF analyses: spatial modes 1 (a) and 2 (b); temporal modes 1 (c: phase, d: amplitude) and 2 (e: phase, f: amplitude). The reconstructed velocity for each mode corresponds to the local spatial value multiplied by the dimensionless amplitude and rotated of the respective phase angle. For clarity, arrows are represented every three grid nodes. The ticks on the x-axes indicate the beginning of spring and autumn. The blue line on d and f represents the low-passed filtered time series with a cut-off period of 6 months.

2.5.4 Flow Variability

The Hovmöller diagrams of currents at transects TrW, TrCSM and TrE show that the alongshore component is generally stronger than the cross-shore one (Figure 2.8; see Figure 2.1 for transects location). Both components tend also to be weakest at TrE (Figure 2.8e-f), as previously observed at the eastern bight on the mean and STD maps (see Figures 2.5 and 2.6). Coastal PFs are often restricted to the shelf, i.e., up to the 200 m isobath (indicated with black

horizontal lines in Figure 2.8). By contrast, EFs tend to occupy the entire transects' length, especially at TrW and TrCSM. The analysis of coastal flows' width (i.e., cross-shore extension from land) confirms this pattern: 60-70% of PFs extends up to the shelf break (Figures 2.9a, 2.9c and 2.9e), while EFs extends dominantly up to the offshore limit of each transect (Figures 2.9b, 2.9d and 2.9f). Cross-shore velocities are predominantly directed offshore (orange in Figure 2.8). Onshore flows (green in Figure 2.8) may occur at any season, the strongest events being often associated with strong PFs (red in Figure 2.8) along the whole transects (such as in March-June 2017) corresponding to periods of north-westward flows over the study area.

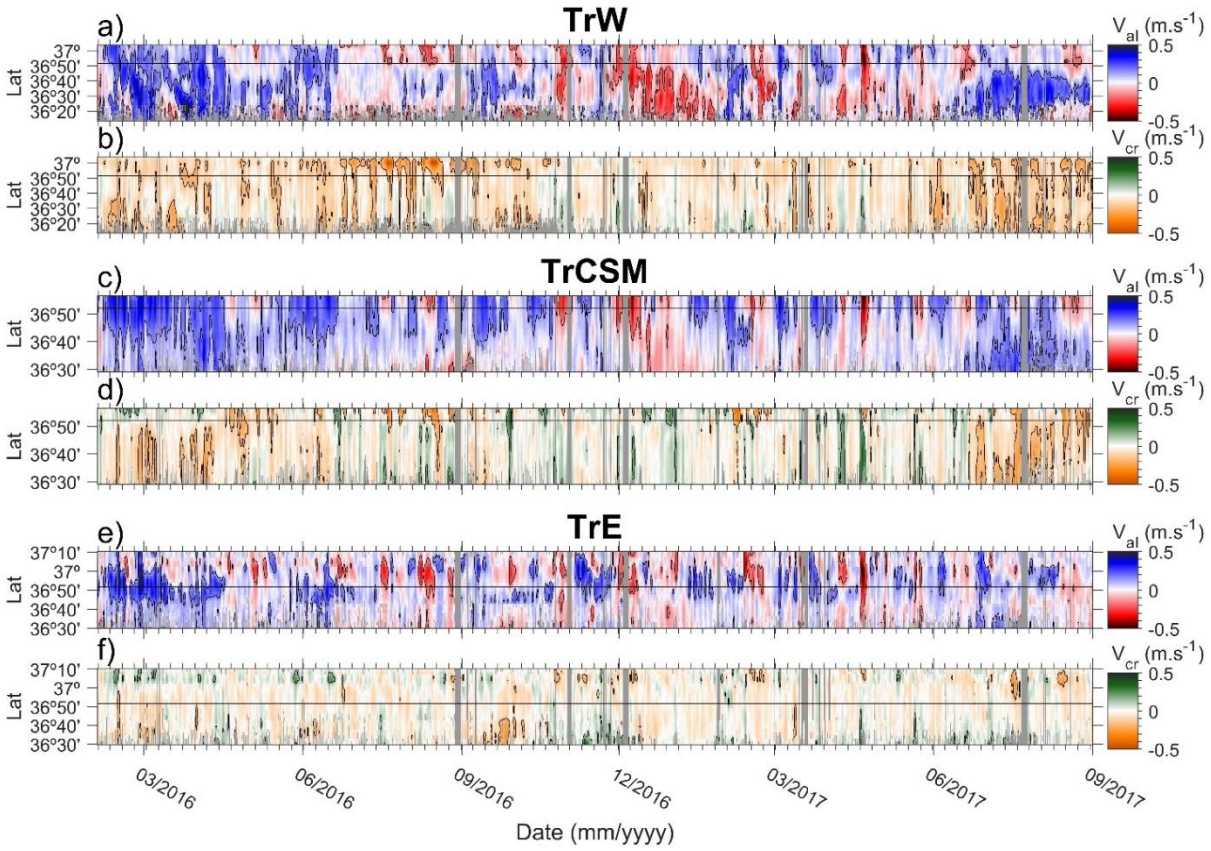

Figure 2.8 - Hovmöller diagram of V_{al} (a, c, e) and V_{cr} (b, d, f) extracted at transects TrW, TrCSM and TrE, from 03 February 2016 to 01 September 2017. Equatorward and poleward velocities are represented in blue and red, respectively; onshore and offshore velocities are represented in green and orange, respectively. Black contours indicate ±0.15 m.s^{-1}. The 200 m isobath is indicated as a black horizontal line. Major ticks on x axes represent the first day of the indicated month and minor ticks represent one-week interval.

At TrW, strong offshore flows (V_{cr} up to 0.5 m.s^{-1}) are observed over the shelf in summer and autumn (e.g., see summer 2016 in Figure 2.8b). During these events, V_{al} is mainly poleward over the shelf and equatorward further offshore, in agreement with the cyclonic pattern

described by EOF mode 2 (also in summer and autumn) over this region (see Figures 2.7b, 2.7e and 2.7f). Similar observations at TrCSM also suggest an episodic cyclonic recirculation of coastal PFs in front of CSM (e.g., end of summer 2017 in Figure 2.8c-d).

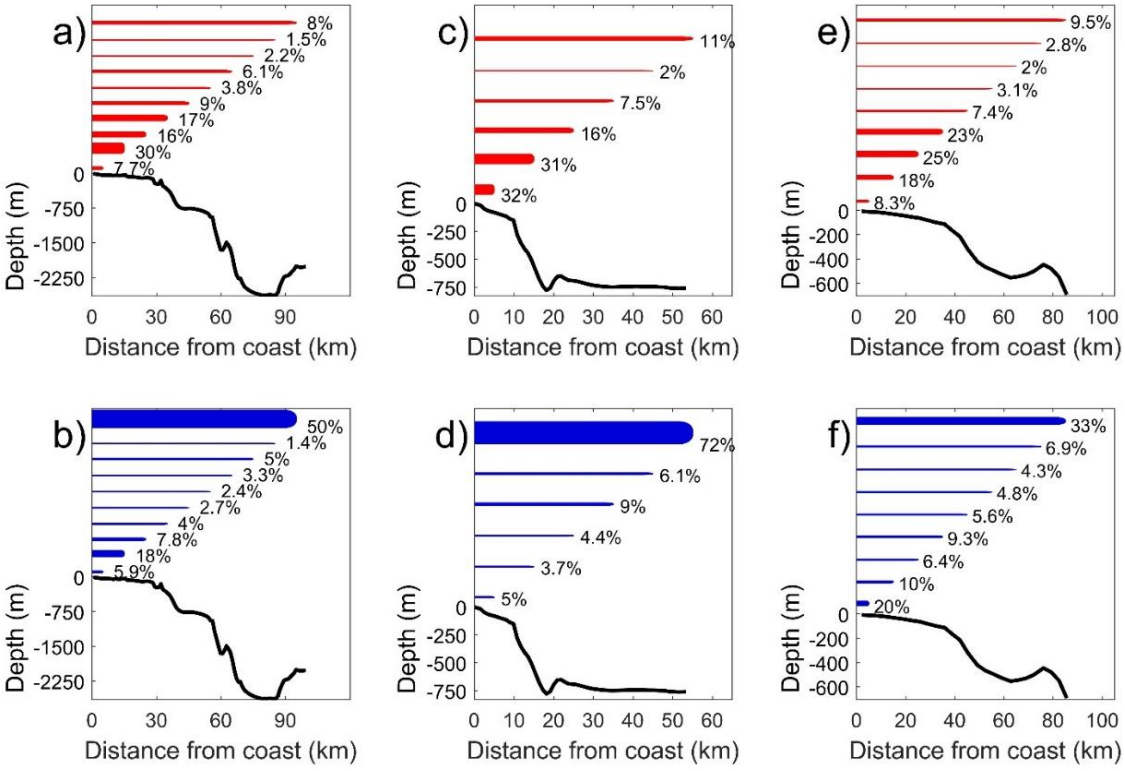

Figure 2.9 - Percentage of the offshore extent (from the coast) of alongshore flows (PF: red; EF: blue) at transects TrW (a-b), TrCSM (c-d) and TrE (e-f). Each bar represents the distance from the coast and bar thickness indicates the percentage. The along-transect bathymetry is represented as a black line.

2.6 Discussion

2.6.1 Slope Current

The present analysis of HFR subtidal currents shows that the mean surface circulation at the NMGoC is south-eastward and strongest over the slope at the so-called RIMC (Figures 2.5 and 2.6). Previous surveys have directly measured strong currents oriented along the slope with magnitude (0.15-0.2 $m.s^{-1}$) similar to the present observations (e.g., Figure 2.8; Cravo et al.,

2013; Relvas and Barton, 2005; Criado-Aldeanueva et al., 2009, 2006; García-Lafuente et al., 2006; García Lafuente and Ruiz, 2007; Peliz et al., 2009a). This current is a prominent feature of the spring-summer climatological geostrophic circulation (Sánchez and Relvas, 2003). Numerical modelling also predicts a temporally persistent slope current, the GCC, with equivalent magnitude in the upper layer (Peliz et al., 2014, 2009a, 2007).

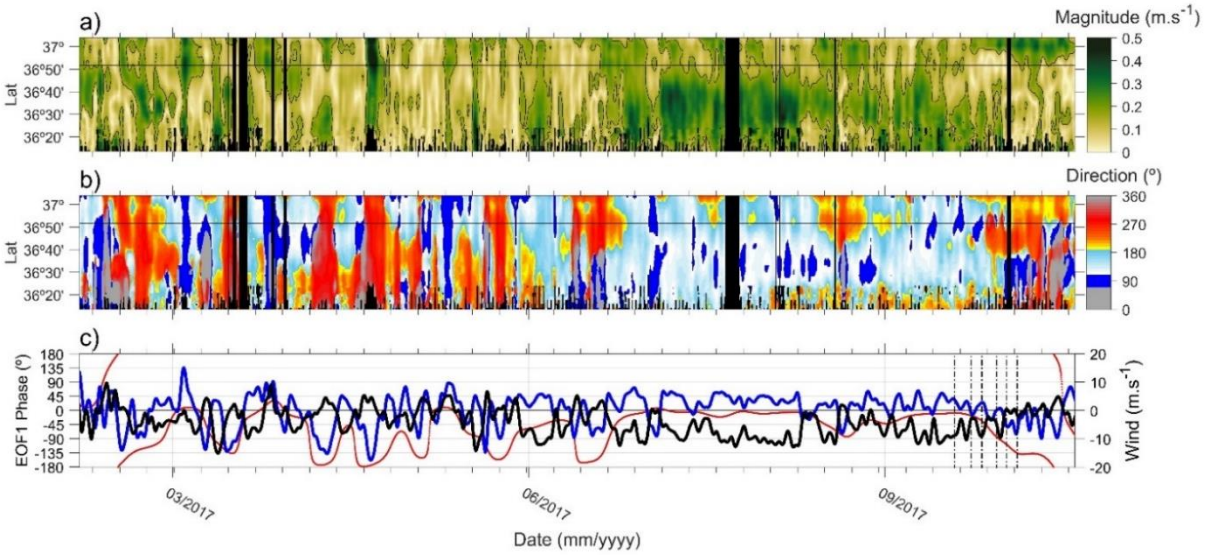

Figure 2.10 - Hovmöller diagram of (a) magnitude and (b) directions of currents at transect TrW; (c) zonal (blue line) and meridional (black line) of sub-inertial ERA5 wind (https://cds.climate.copernicus.eu, last access: 18 September 2021) extracted at 36◦45′ N, 8◦30′ W along with the phase of EOF mode 1 (red points). Dashed vertical lines indicate the day of each of the SST maps represented in Fig. 11. Major ticks on x axes represent the first day of the indicated month, and minor ticks represent 1-week interval.

The mean HFR flow at the RIMC follows rigorously the slope at the eastern bight, in agreement with previous studies, but not at west where it is oblique to the shelf break orientation. Yet, along shelf (i.e., eastward) currents develop frequently at the western bight, as indicated by the flow directional distribution (see the east-west elongated STD ellipses in Figure 2.5b). It is noted that the off-shelf flow variability is greatest at the western border of the GoC (Figure 2.7a-b), the region most exposed to north-westerlies. The predominance of north-westerlies during the upwelling season (de Oliveira Júnior et al., 2021; Garel et al., 2016; Sánchez et al., 2007) corresponds to a modulation of the slope circulation, which is stronger, broader and with the largest main variability in summer (Figure 2.6; Figure 2.7d, blue line). To evaluate the effect

of the wind on the off-shelf circulation, the ERA5 subtidal wind at 36°45'N 8°30'W (see Figure 2.1) is compared with the velocity along TrW in February-October 2017 (Figure 2.10). In Figure 2.10b, the colour scale of the flow direction is designed to highlight along slope flows (i.e., eastward, in dark blue), southeast flows (light blue) and broadly westward flows (red). In winter, the slope current alternates frequently with periods of westward circulation over the entire margin associated to Levanter wind (Figure 2.10b-c). In summer, north-westerlies dominate (Figure 2.10c), and the off-shelf flow is strong (dark green in Figure 2.10a); the slope current (dark blue) is shifted offshore and often rotated to the southeast (light blue) along the wind direction. It is noted that the south-eastward circulation over the western margin associated to strong north-westerlies is very similar to the mean circulation (compare Figure 2.5a with the example of Figure 2.11a which wind conditions are indicated in Figure 2.10c). The wind conditions that allow the development of the (eastward) along slope surface flow are not clear. However, these observations show that north-westerlies tend to deflect clockwise the surface slope current measured by HFR, as reported in other areas exposed to strong wind (e.g., Lipa et al., 2014).

At the eastern bight, CTD and SST observations suggest that the slope current constitutes the northern branch of a persistent large-scale anticyclonic cell (Sánchez and Relvas, 2003; Vargas et al., 2003). The HFR data coverage is too limited offshore to map such eddy. However, such recirculation is consistent with the strong enhancement of the cross-shelf flow component that was reported at the eastern limit of the study area (Figures 2.5a and 2.6a-d).

The CTD and SST data indicate that the slope current has a relatively low temperature and salinity in spring-summer, typical of upwelled Atlantic waters in the GoC (Fiúza, 1983; Folkard et al., 1997; Relvas and Barton, 2002; Sánchez and Relvas, 2003; Vargas et al., 2003; see also the SST in Figure 2.11). Coastal upwelling produced by Ekman transport under favourable local wind is often cited as the driver of the geostrophic jet over the slope, similar to the southward jet observed along the west Iberian coast (Relvas and Barton, 2002; Sánchez and Relvas, 2003). It has also been observed that the latter southward jet turns cyclonically at CSV due to conservation of potential vorticity and progresses eastward towards the Strait of Gibraltar, merging with locally upwelled water (García-Lafuente et al., 2006; Relvas and Barton, 2002; Sánchez and Relvas, 2003). In addition, wind stress curl produced at CSV is expected to affect the water circulation at the western bight during the upwelling season (Criado-Aldeanueva et

al., 2006a; García-Lafuente et al., 2006; Sánchez-Leal et al., 2020; Sánchez et al., 2007; Sánchez and Relvas, 2003), when northerlies are most frequent and intense over the west Iberian coast (Alvarez et al., 2008; Fiúza et al., 1982; Leitão et al., 2018). According to Castelao and Barth (2007), a geostrophic equatorward jet must develop offshore of the curl maxima as a response to Ekman pumping. Satellite observations in spring and summer indicate that the (monthly and seasonal) mean curl maxima may reach as south as 36°N over the western bight (Alvarez et al., 2008; Castelao and Luo, 2018; Criado-Aldeanueva et al., 2006a; Sánchez and Relvas, 2003), in agreement with the southward extent of the RIMC during these seasons (Figure 2.6 b-c). These processes may contribute to the development of the slope flow at the NMGoC during the upwelling season. Local upwelling in winter is also expected due to the eastward migration of the Azores high pressure cell, promoting westerlies over the GoC (Chase, 1951). Furthermore, numerical modelling simulations suggested that part of the Atlantic water is entrained by the denser Mediterranean outflow below, producing a slope current due to mass conservation (Kida et al., 2008; Peliz et al., 2009a, 2007). Since water exchange in the Strait of Gibraltar is continuous (García-lafuente et al., 2021; García-Lafuente et al., 2011), this mechanism could contribute to the observation of a slope current throughout the year, as reported in the present study.

Long-term (11 years) ADCP records at a sub monthly time-scale (i.e., low-pass filtered with a cut-off period of 40 days) over the eastern shelf slope (45 km South-eastward from TrE at 450m water depth) shows that reversals of south-eastward flows are wind driven (Criado-Aldeanueva et al., 2009). “Levanter” wind events typically blow north-westward at the study area without clear seasonality (de Oliveira Júnior et al., 2021; Losada, 1999; Ribas-Ribas et al., 2011). As exemplified in winter 2017, the south-eastward circulation over the entire NMGoC reverses during these (strong) events (see red in Figure 2.10b). In addition, the circulation described by EOF mode 1 when the phase is close to 180° (see Figure 2.7) is remarkably associated to strong Levanters (Figure 2.10c), indicating the reversal of the main flow pattern over the NMGoC. These events correspond to the ~10% of PFs occupying the entire margin on Figures 2.9a, 2.9c and 2.9e) and generally occur when the eastern component of ERA5 wind in the area is greater than 10 $m.s^{-1}$, approximately (not shown).

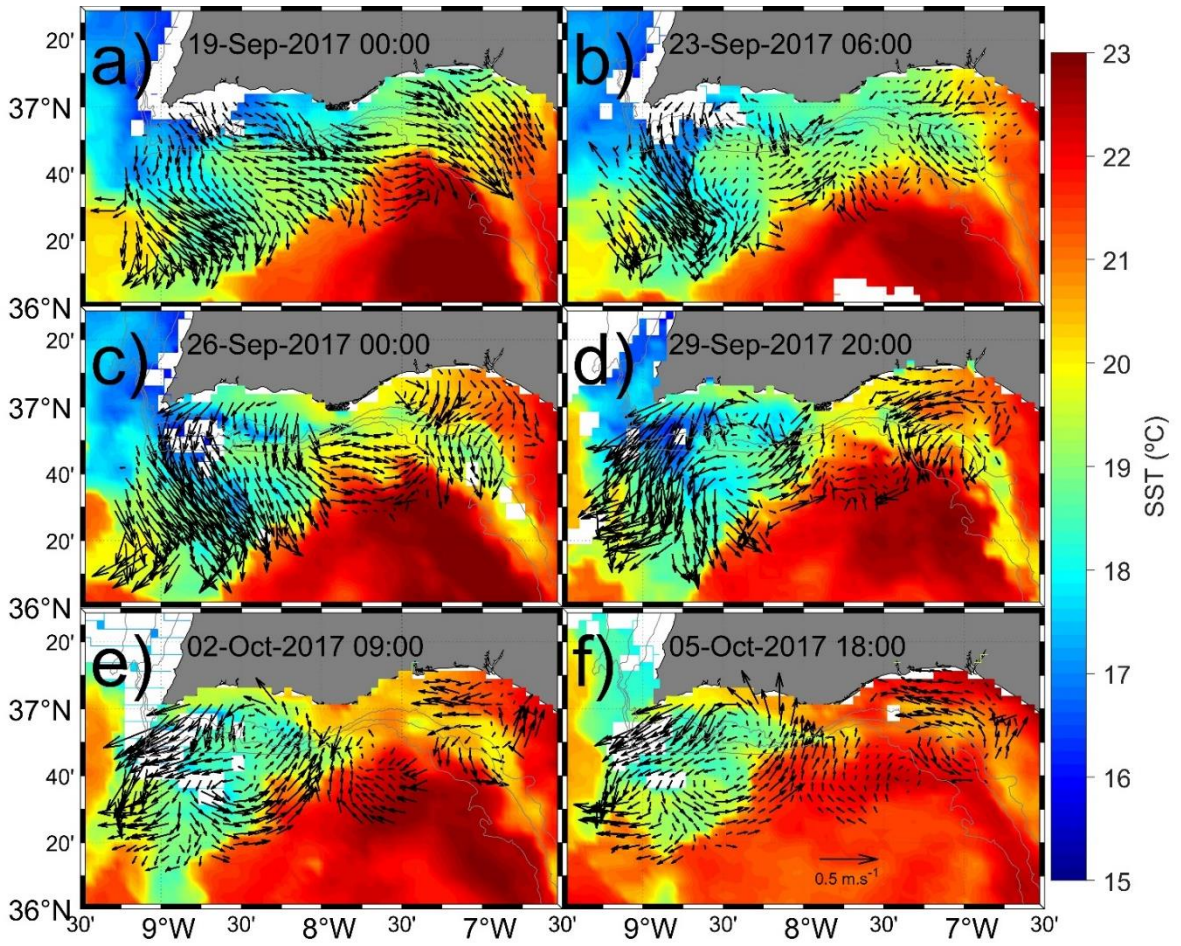

Figure 2.11 - SST from VIIRS-SNPP (https://oceandata.sci.gsfc.nasa.gov, last access: 15 November 2021) and HFR subtidal surface currents (as arrows, the scale of which is indicated in f). For clarity, arrows are represented every four grid node.

2.6.2 Shelf Circulation

The HFR and ADCP data analyses show that subtidal coastal currents are polarized in the alongshore direction at the NMGoC (Figures 2.4, 2.5, 2.7 and Table 2), generalizing similar findings from few ADCP mooring sites at the eastern bight (de Oliveira Júnior et al., 2021; Garel et al., 2016; Prieto et al., 2009). EOF modes 1 and 2 indicate that the circulation is generally a regional feature, continuous along the coast (Figure 2.7). This coastal circulation pattern opposes the frequent disruption of PFs near CSM proposed by García-Lafuente et al. (2006) which is often cited in the literature (.eg., Casaucao et al., 2021; de Castro et al., 2017; Hanebuth et al., 2018; Mestdagh et al., 2020; Navarro et al., 2013). In agreement with García-

Lafuente et al. (2006), the connection between PFs at both bights is not always clear (e.g., Figure 2.11). Comparison of the alongshore flow at various shelf locations, as exemplified in Figure 2.12, suggest that the PF circulation is continuous for relatively strong velocities (>0. 1 m.s-1). Conditioned mean maps based on the alongshore velocity at W2 show that PFs are continuous for Val >0.1 m.s-1 (Figure 2.13a-b). By contrast, EFs are always continuous (Figure 2.13c-d). Clearly, the setup of PFs at CSM occurs when these flows are well developed at the adjacent bights. This delay (see 7 and 19 of April 2017 in Figure 2.12) explains the predominance of EFs at CSM, while EFs and PFs are balanced elsewhere (Table 2) as previously observed at Armona Station (Garel et al., 2016). The delay is possibly due to cape-induced bathymetric and geographic effects (e.g., Gan and Allen, 2002). In particular, the slope current is very close to the coastline near CSM. In details, PFs from the eastern bight overshoot CSM and turn sharply northward to connect with the inner-shelf flow at the western bight, which results in the N-S elongated STD ellipses at west of CSM (Figures 2.5, 2.6; see also the spatial patterns of both EOF modes in Figure 2.7).

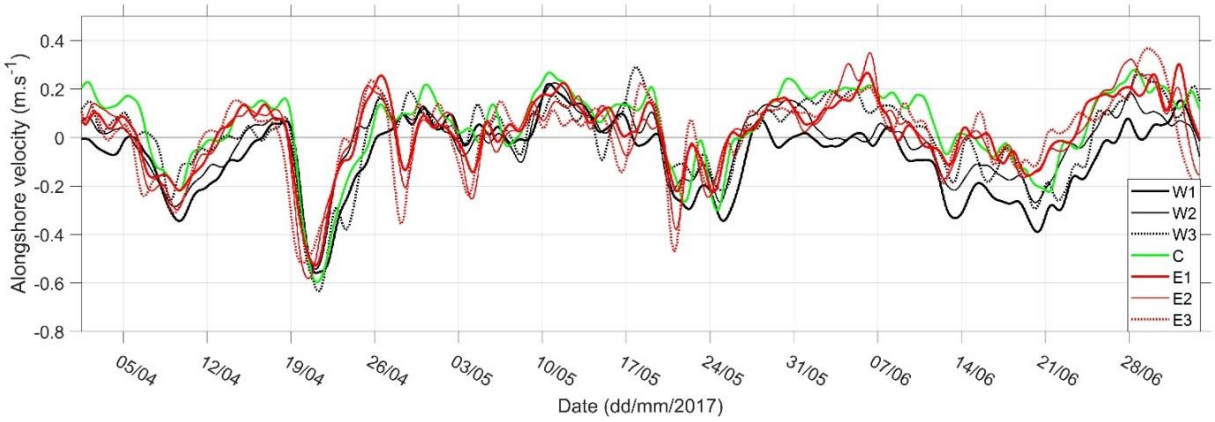

Figure 2.12 - Alongshore velocities at the 7 selected nodes. See Figure 2.1 for location. Alongshore velocities are obtained from the angle of maximum variance of velocity vectors at each node.

Based on SST images, it has been suggested that the PF signal propagates from the eastern to the western bight (see for example Figure 2.11); likewise, that EFs proceed at least partly from the west Portuguese coast (Relvas and Barton, 2002). Such propagation patterns are not conspicuous on the subset of alongshore velocities reported in Figure 2.12. To evaluate whether coastal flows develop preferentially at the eastern or western bights, the timing of EFs and PFs

development is analysed considering the 3 grid nodes W2, C, and E3 (for location, see Figure 2.1). Flow reversals were defined as events occurring at the 3 grid nodes within a 7-day period. To discard small oscillations in flow direction, an event was retained when, at each selected node, V_{al} was ≥ 0.05 m.s^{-1} before and after reversed flows lasting 36 h, at least. A total of 23 EFs and 25 PFs reversal events were detected. In total, 61% of EFs developed first at E3 (against 17% at W2) and 48% of PFs develop first at W2 (against 44% at E3). Sequential reversals at adjacent nodes (i.e., W2 then C then E3 for EFs; the opposite for PFs) were defined as propagation events; no propagation event was obtained for PFs (that tend to develop latter at CSM, as previously described) and only 3 events for EFs. Thus, coastal flows appear first at any of both bights, but tend to appear first at the bight towards which they are directed, as illustrated on 06 June 2017 (PF developed first at west) and on 21 June 2017 (EF developed first at east) in Figure 2.12 (see also the early development of PFs at the western bight in Figure 2.11b and 2.11c).

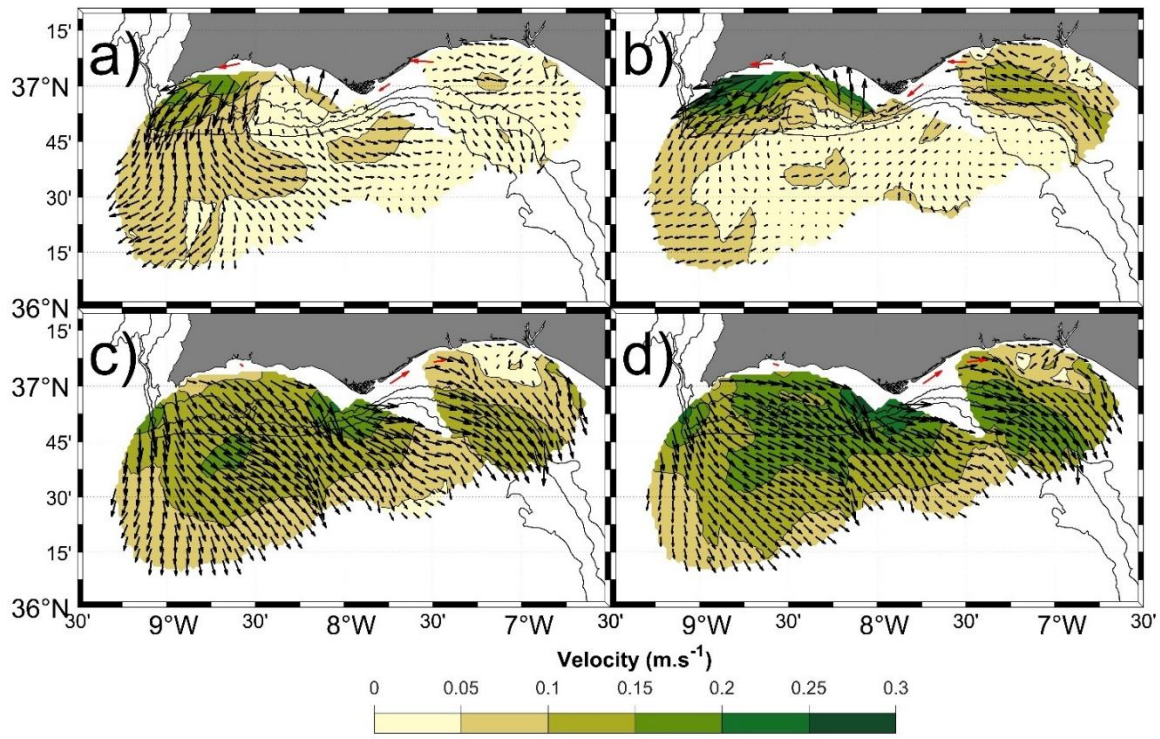

Figure 2.13 - Conditioned mean map computed from periods when the alongshore velocity at W2 was between 0.05 m.s^{-1} and 0.1 m.s^{-1} (a and c) and for periods with velocities >0.1 m.s^{-1} (b and d). Upper (lower) panel represent PFs (EFs). Red arrows indicate the mean velocity computed from available ADCP data for the same periods. For clarity, arrows are represented every four grid nodes.

CCCs have been suggested to be driven in summer by alongshore pressure differences due strong temperature gradient between Cadiz and Huelva (García-Lafuente et al., 2006). This small-scale thermal gradient, restricted to the eastern bight, fails to explain the early setup of PFs at the western bight (where alongshore temperature variations are comparatively weaker; e.g., Vargas et al., 2003; see also Figure 2.11). Instead, an alongshore pressure gradient of regional scale, from the region of the Guadalquivir mouth to CSV (Relvas and Barton, 2002), is consistent with the erratic-like setup of PFs along the coast. Finally, it is noted that the 44% of PFs that started at E3 developed at W2 with an average delay of 1.24 day. This represents an average propagation speed of 2 $m.s^{-1}$ which is within the range of coastal trapped wave propagation at other systems (Maiwa et al., 2010; Rivas, 2017).

As discussed in Section 2.6.1, about 10% of PFs correspond to a general north-westward circulation over the entire NMGoC associated to strong Levanter wind (>10 $m.s^{-1}$). In these cases, PFs observed at the coast are mainly wind-driven and should not be considered as CCCs. For weaker wind conditions, about 60% of PFs are restricted to the shelf (Figure 2.9), opposed to the dominant flow direction on the slope, and should therefore be regarded as CCCs. This spatial distribution is concordant with SST observations of warm water near the coast and cold waters further offshore in spring and summer (Fiúza, 1983; Folkard et al., 1997; Relvas and Barton, 2002, 2005; Reul et al., 2006) as exemplified in Figure 2.11. Comparisons of the flow direction at depths of 40 m and 500 m at the transects indicate that CCCs develop predominantly (>60%) during the upwelling season (with maximum in late summer-early autumn) and are the rarest (<10 %) in late autumn and winter. Consequently, PFs in winter are mainly wind-driven while they are often CCCs (i.e., alongshore coastal flows with direction opposed to the eastward slope current) driven by distinct processes in summer (de Oliveira Júnior et al., 2021; García-Lafuente et al., 2006; Garel et al., 2016; Relvas and Barton, 2002; Teles-Machado et al., 2007).

2.6.3 Recirculation Between Shelf and Slope Flows

Mode 2 of the EOF analysis (that represents 12% of the data variability) indicates episodic recirculation between the shelf and off-shelf regions over the western bight (Figure 2.7b). This recirculation is cyclonic and most frequent in summer and autumn when mode 1 is weak and mode 2 is in phase (see section 2.5.3). To highlight this recirculation, data are selected from June to October when mode 2 phase is between -65° and 65° and the ratio of mode 1 and mode

2 amplitudes is ≤ 2. The conditioned mean map obtained from these subsets outlines a cyclonic eddy over the entire western bight (Figure 2.14). The northern branch of the eddy consists of a CCCs (see also the ADCP current direction in the inner-shelf, red arrows in Figure 2.14) that strongly recirculates offshore near CSV. This recirculation provides a mean to transport offshore coastal water-borne material such as chlorophyll (see Figure 4 in Cristina et al., 2015). It is consistent with the rare observation (based on SST) of CCCs propagating around CSV and northward along the western coast during persistent Levanter wind conditions (Relvas and Barton, 2002). The shelf region with strong southward velocity near 8°40'W (Figure 2.5) which is best defined in summer results from this recirculation. The southern branch of the eddy is constituted by the slope current.

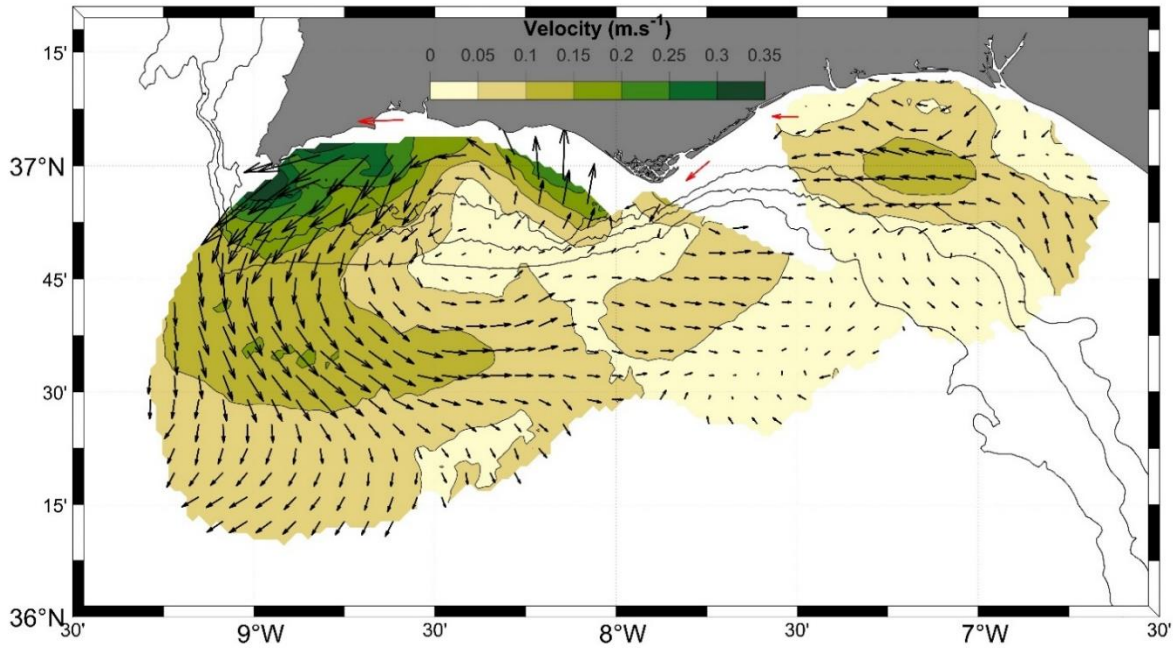

Figure 2.14 - Conditioned mean map computed from periods in June to October with mode 2 phase between -65° and 65° and the ratio of mode 1 and mode 2 amplitudes ≤ 2. For clarity, arrows are represented every four grid nodes. Red arrows indicate the mean velocity computed from available ADCP data for the same periods.

A cyclonic eddy was previously described as a quasi-permanent feature in spring and summer over the western bight (García-Lafuente et al., 2006). The positive vertical component of northerly wind curl at West of CSV produces ascending velocities resulting in an uprising of the isopycnic and advection of dense water from the ocean's interior towards the surface

(Sánchez and Relvas, 2003). Because of this upwelling process, a cyclonic circulation must develop to compensate the baroclinic pressure field (Criado-Aldeanueva et al., 2006a; García-Lafuente et al., 2006). To investigate the eddy occurrence, a vector geometry–based detection algorithm was applied to the HFR time series (for details about the method, see Nencioli et al., 2010). The dataset was subsampled at each 3 grid nodes and a reduced area focused on the western bight (8°W - 9°W and 36°30'N - 37°N) was selected. Eddy centres were detected at grid points where four constraints were satisfied. These constraints use two parameters (a and b) that can be specified in order to give flexibility to the algorithm. After several sensitivity tests, the most suitable values for a and b were defined to be 4 and 3 respectively. From the 708 detections, less than 2% occurred from November to March and more than 77% from June to October. An example is provided in August 2017 when the CCCs recirculated cyclonically after a period of general southeast flows (in Figure 2.15a-b). The eddy was briefly detected during the cyclonic recirculation period (blue dot in Figure 2.15c), followed by a period with strong offshore shelf flows (Figure 2.15d). Recirculation events (identified based on the EOF criteria defined in the previous paragraph) clearly correspond to the development of CCCs, i.e., opposed shelf and slope flows (see summer-autumn 2017 in Figure 2.15e, where recirculation events identified by the red triangles on top). The cyclonic recirculation develops after periods of relatively strong north-westerlies (Figure 2.15f-g). These conditions agree with the development of CCCs during the relaxation of upwelling favourable wind supporting that they result from the unbalance of a regional along-shore pressure gradient (de Oliveira Júnior et al., 2021; Garel et al., 2016; Relvas and Barton, 2002). The eddy is a transient feature (at least at the surface) detected during these periods, under low wind stress conditions (doted lines in Figure 2.15; Figure 2.15g; see also Figure 2.11).

García-Lafuente et al. (2006) also proposed the presence a quasi-permanent cyclonic eddy over the eastern bight. A cyclonic recirculation in this region is not apparent in the mean maps (Figures 2.5 and 2.6) and EOF analyses (Figure 2.7). Furthermore, the previously described algorithm yielded significantly less (60) detections at the eastern bight compared with the western bight (708). These eddies tend to develop when the western eddy is present (63%, within a time window of 36h), as exemplified in Figure 2.11f. Cyclonic recirculation of the CCC was also noted at TrCSM, but more rarely than at west (compare Figures 2.8a-b and 2.8c-d). Overall, the data suggests that a cyclonic recirculation between shelf and slope flows at the

eastern bight is less frequent than at west. However, it is not ruled out that this is due to the limited data coverage (see Figure 2.3).

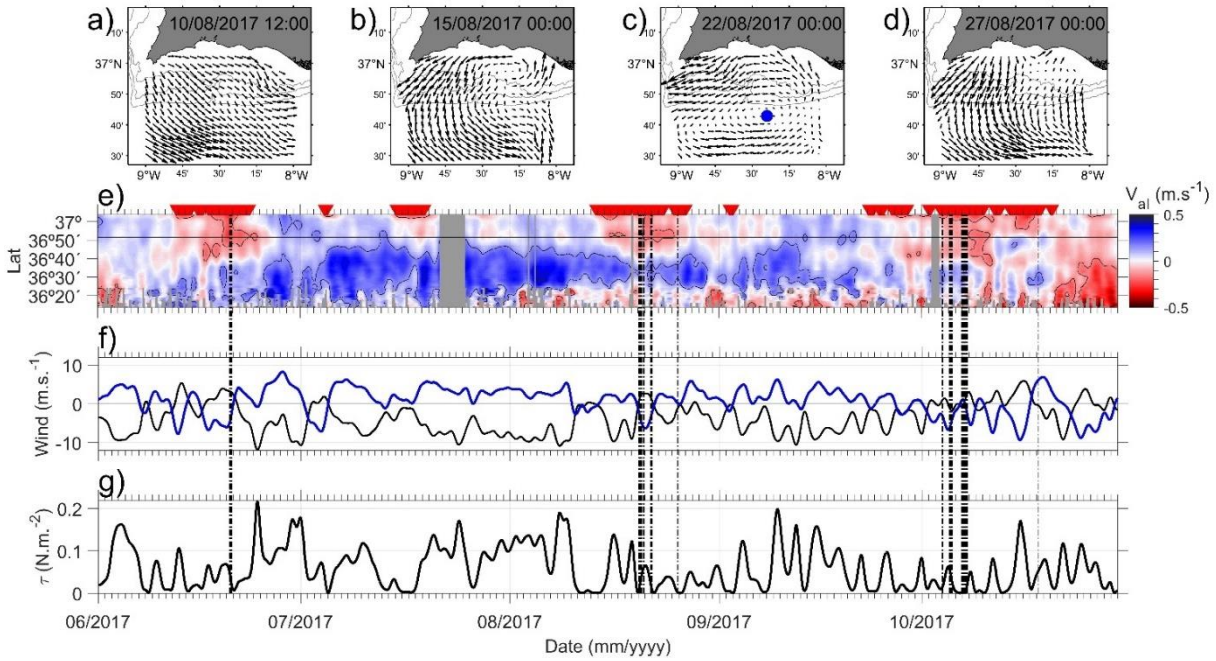

Figure 2.15 - Example of the cyclonic circulation evolution over the western region (a-d) and the detected cyclonic eddy centre (indicated by the blue dot in c). Hovmöller diagram of filtered V_{al} extracted at TrW (e). Red triangles on top represent recirculation periods identified based on EOF criteria (mode 2 phase between -65° and 65° and ratio of mode 1 and mode 2 amplitudes ≤ 2). Filtered ERA5 wind averaged at the box -9°E, -7°E, 36°45'N and 37N°, black and blue curves representing the meridional and zonal components, respectively (f). Wind stress magnitude (e). Black dotted vertical lines indicate periods when a cyclonic eddy was detected by the algorithm over the western bight. Major ticks represent the first day of the indicated month and minor ticks represent one-day interval.

2.7 Conclusions

The present study depicts the main patterns of the surface circulation at the NMGoC, based on the analysis of hourly HFR currents from 2016 to 2020. The following conclusions are drawn, which are used to update the previous circulation sketch of the surface circulation during the upwelling season proposed for this region for no storm conditions (Garcia-Lafuente et al., 2006). The main circulation patterns are represented as arrows which red (blue) colour indicates the direction of warm (cold) water advection (Figure 2.16); a wider arrow corresponds to a

greater flow magnitude and a difference in the double arrowhead size represents an unbalanced flow direction; dashed arrows indicate a transient (or sporadic) circulation.

- The background circulation over the NMGoC is south-eastward as a result of the dominant north-westerlies (grey arrows in Figure 2.16). This circulation episodically reverses as a result of strong easterlies. Overall, the circulation is weaker at the eastern than at the western bight (as represented with the distinct arrows size in Figure 2.16).

- An equatorward slope current (GCC in Figure 2.16, following Peliz et al., 2007) is observed along the continental shelf slope, which magnitude and width is seasonally modulated (stronger and broader in summer). This flow proceeds from the upwelling jet along the western coast. Strong north-westerlies tend to deflect this surface flow clockwise over the (exposed) western bight. At the eastern border of the study area, the observations support that the slope current partly recirculates anticyclonically (see Figure 2.16).

- Shelf flows are alongshore and balanced at the eastern and western bights (see the equal double head sizes in Figure 2.16), changing direction twice a week in average, without clear seasonality (Garel et al., 2016). PFs (EFs) advect warm (cold) water in summer (see the blue and red arrows in Figure 2.16, respectively). Contrarily to the SST, the alongshore flow signal does not propagate along the coast. Instead, it tends to develop first at the bight towards which the flow is directed (i.e., PFs tend to develop first at the western shelf and EFs at the eastern shelf), consistent with a regional alongshore pressure gradient inversion.

- EFs dominate near CSM (see the distinct double arrow sizes around the cape in Figure 2.16) due to a delay in the setup of PFs. The flow reverses when PFs are >0.1 $m.s^{-1}$ (approximately) at the adjacent bights. Since these magnitudes are frequently reached, PFs generally go around the cape and are continuous along the coast.

- The EFs observed near the coast often extend over the entire margin as they merge offshore with the slope current (GCC).

- The PFs observed near the coast in winter are mainly associated to strong easterlies and extend over the entire margin. During the upwelling season, they dominantly consist of CCCs,

i.e., alongshore coastal flows with direction opposed to the equatorward slope current (Figure 2.16).

- At west, CCCs constitute the northern branch of a cyclonic recirculation which is strongest near CSV, promoting significant offshore transport and explaining the sporadic advection of warm water to the north of CSV (see the dashed red arrow near the cape in Figure 2.16). This recirculation pattern (including CCCs) develops during the relaxation of upwelling favourable wind supporting that they result from the unbalance of a regional along-shore pressure gradient. For weak wind stress, a transient eddy is episodically formed, limited at south by the GCC and at east by onshore currents near CSM (see the dashed arrow near the cape in Figure 2.16).

- At East, the core of alongshore flows is detached from the coast, on the outer shelf (Figure 2.16). Cyclonic recirculation of CCCs seems less frequent than at west (see dashed arrows in Figure 2.16), although this result can be due to the limited spatial coverage of HFR data in this bight.

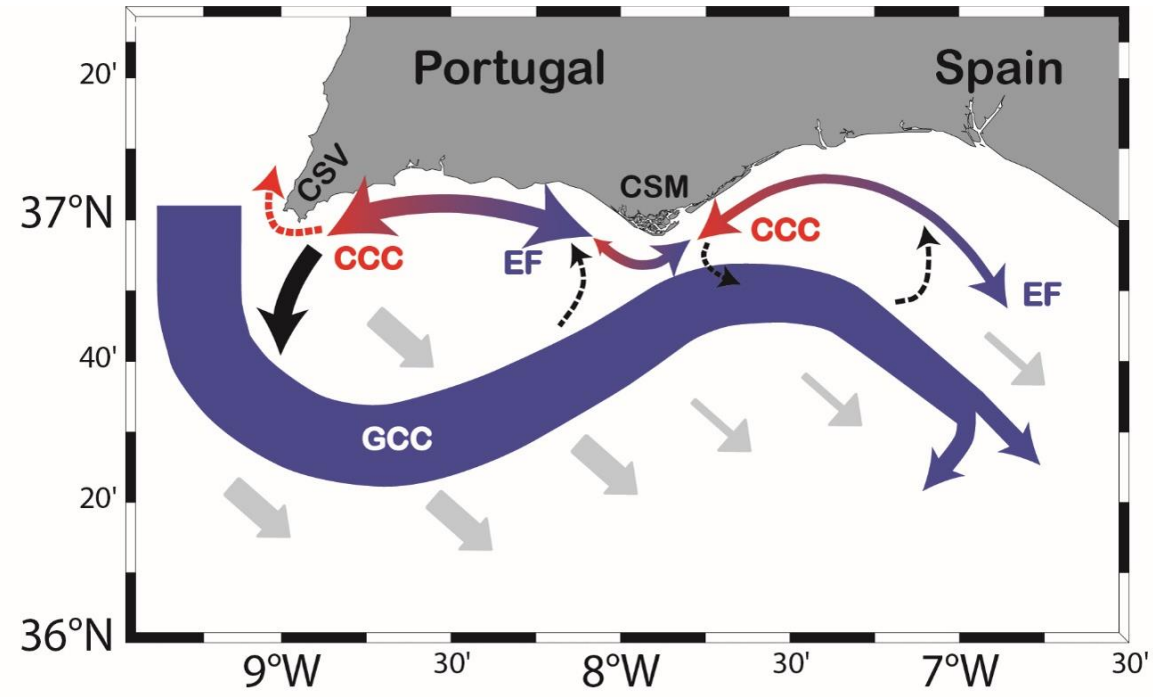

Figure 2.16 - Updated sketch of the main circulation patterns at the NMGoC during the upwelling season for no storm conditions. The flow magnitude (schematically represented by the size of the arrows) is larger at the western bight than at the eastern bight. Red (blue) arrows indicate the direction of warm (cold) water advection. Dashed arrows indicate a transient (or sporadic) circulation. An equatorward slope current (the Gulf of Cadiz Current, GCC) proceeding from the West Portuguese coast and advecting cold water is superimposed to the background south-eastward, wind-induced, circulation (grey arrows). The GCC partly recirculates anticyclonically at east. On the shelf, the flow is alongshore and balanced between the equatorward and poleward directions (as represented with equal double arrows head sizes), except near Cape Santa Maria (CSM). There, equatorward flows predominate (see the distinct double arrowhead sizes around the cape) as they reverse with some delay compared with the adjacent bights. However, the equatorward flows (advecting cold water) and poleward flows (advecting warm water) are generally continuous along the coast, reversing twice a week, in average. Poleward flows are Coastal Counter Currents (CCCs), i.e., with opposed direction than the GCC, which develop after periods of north-westerlies. At the western bight, they are associated to a cyclonic recirculation, strongest near Cape São Vicente (CSV), explaining the sporadic advection of warm water to the north of the cape (see the dashed red arrow near the cape). For weak wind stress, this recirculation depicts a short-lived eddy over the bight due to onshore recirculation near CSM (see the dashed arrow near the cape). At the eastern bight, the CCCs and equatorward flows are strongest at the outer shelf (rather than at the inner shelf at West). Cyclonic recirculation of CCCs occurs less frequently than at west (see dashed arrows).

Chapter 3 - Upwelling processes variability and water circulation along the Northern Margin of the Gulf of Cadiz

Abstract

Winds from SKIRON, a high-resolution weather forecast model, were used to estimate the Ekman transport and Ekman pumping and to explore their effects on the circulation at the northern margin of the Gulf of Cadiz, together with sea surface temperature, sea level anomaly and current observations. Upwelling favourable conditions occurs throughout the year along the NMGoC, with the strongest intensity near Cape São Vicente (CSV) due to a persistent positive wind stress curl. In winter the surface water divergence is restricted to the coastal boundary due to strong Ekman transport events and comparatively weaker Ekman pumping, resulting in a maximum cross-shore sea-level gradient close to the coast. Towards the summer, the gradient increases and extends further offshore (over the slope) at the western region due to the intensification of the Ekman pumping. Therefore, the seasonal and spatial variability of Ekman transport and Ekman pumping contributes significantly to the offshore position of the geostrophic Gulf of Cadiz Current over the western shelf slope. Furthermore, a permanent sea level depression corresponds to the location of the strongest Ekman pumping, near CSV. The dynamic adjustment of the sea level depression promotes the development of the cyclonic cell and alongshore poleward currents often observed in the area.

3.1 Introduction

Wind-driven coastal upwelling is an oceanic phenomenon that results from the divergence of surface waters at the coastal boundary due to alongshore winds and the earth's rotation in a

process called Ekman transport (Gill, 1982). If the wind blows with the coast on its left (right) side in the northern (southern) hemisphere, it will promote offshore surface transport that must be replaced by cold and nutrient-rich deeper waters in a relatively narrow band next to the coast (Capet et al., 2004). Since wind generally varies in space, so does the Ekman transport, and divergence arises in the ocean surface waters, forcing upward velocities independently of the coastal boundary (Gill, 1982). This upwelling mechanism is often called Ekman pumping and is associated with positive wind stress curl typical of regions with prominent topographic features. Compared to Ekman transport, Ekman pumping drives weaker upwelling over a much larger area (Capet et al., 2004), that may extend hundreds of kilometres offshore. Nonetheless, vertical velocities from Ekman pumping when integrated over some distance offshore can be similarly important (Pickett and Paduan, 2003). At the California upwelling system, the integration of the Ekman pumping over 300 km offshore using modelled winds to resolve the curl associated with relatively small-scale topographic features, revealed that it can be as important as Ekman transport from coastal alongshore winds (Pickett and Paduan, 2003). However, at some specific locations, such as the southern California Bight, Ekman pumping associated with one of the major promontories in the California upwelling system was largely dominant. Similarly, the dominance of integrated Ekman pumping over Ekman transport was also demonstrated in other places associated with prominent topographic features such as along the south-eastern Brazilian coast (Castelao and Barth 2006), in Chile (Bravo et al., 2016) and in the south-eastern Arabian Sea (Jayaram and Jose, 2022).

The effect of the Ekman pumping has also been demonstrated to be a determinant factor that controls other aspects of the water circulation. Castelao and Barth (2007) used a high-resolution numerical model to study the importance of spatial variability in the wind forcing to the separation of a coastal upwelling jet at a cape. Their results showed that, as positive wind stress curl drives Ekman pumping upwelling, isotherms are tilted upward in the offshore region, thus forcing southward current velocities via the thermal wind balance. Numerical experiments that include idealized and realistic scenarios also indicated that the gradient of wind stress curl promotes an alongshore pressure gradient that consequently drives alongshore poleward flows (PFs) in the Santa Barbara Channel (SBC, Oey, 1999, 1996). Moreover, the localized effect of Ekman pumping may cause an overall doming of the isopycnals in regions at some distance

from the coast, which promotes a cyclonic circulation to compensate for the baroclinic pressure field (Münchow, 2000; Di Lorenzo, 2003; Wang, 1997).

At the Northern Margin of the Gulf of Cadiz (NMGoC), at the southern limit of the Iberian upwelling system, the effect of the wind stress curl associated with Cape São Vicente (CSV, Figure 3.1) may also be relevant. Some authors suggest that the baroclinic compensation of curl-driven upwelling could be responsible for the recurrently observed cyclonic gyre at the NMGoC (García-Lafuente et al., 2006; Criado-Aldeanueva et al., 2006a; de Oliveira Júnior et al., 2022), as described at the SBC (Münchow, 2000; Di Lorenzo, 2003; Wang, 1997) where the coastline orientation and circulation patterns are similar to the NMGoC. It was also argued that Ekman pumping near CSV could enhance local upwelling and condition the SST fields (Sánchez et al., 2007) and possibly promote an alongshore pressure gradient that drives the coastal counter currents (CCCs) poleward (Sánchez et al., 2006).

Although some efforts have been made in the NMGoC to estimate the effect of curl-driven upwelling (Sánchez and Relvas, 2003; Sánchez-Leal et al., 2020; Alvarez et al., 2008; Castelao and Luo, 2018; Criado-Aldeanueva et al., 2006a), no study has been designed specifically to understand and characterize its variability in the region and assess its direct impact on the circulation. Previous assessments of curl-driven upwelling in the NMGoC were mainly based on satellite scatterometer which covers only regions relatively far from the coast and lacks sufficient resolution to resolve small-scale wind patterns associated with the presence of CSV. In the present study, winds from SKIRON - a high spatial (5 km) and temporal (1 h) resolution model - are used to compute the Ekman transport and the Ekman pumping along the NMGoC. The main objectives are to characterize the Ekman transport and Ekman pumping and evaluate their impact on the circulation. To derive the main conclusions, the transport patterns obtained from the estimated mechanisms are compared with ancillary sea surface temperature (SST), sea level anomaly (SLA) and currents observations. It is shown that Ekman pumping is an important factor for the circulation in the NMGoC affecting both shelf and slope currents as it produces strong upwelling and shapes the sea level slope in both the alongshore and cross-shore directions.

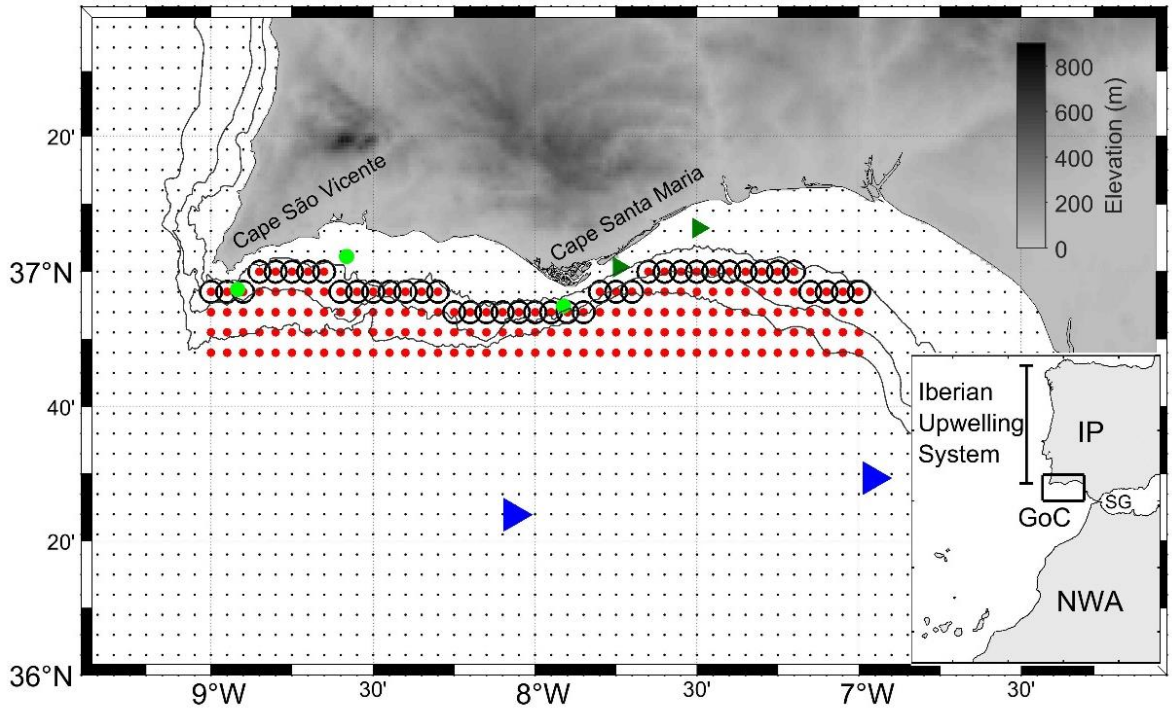

Figure 3.1 - Study area showing the SKIRON grid nodes (black dots). The black circles indicate the grid nodes nearest to the 50 m isobath where the cross-shore Ekman transport (Ek_T) was extracted for comparison with the Ekman pumping transport (EkP_T). Red dots represents nodes from the 50 m isobath to the fixed offshore latitude of 36°48' N representative of the shelf slope region where Ekman pumping velocities (w_{Ek}) were integrated to compute EkP_T (see section 3.3.4). Blue triangles indicate the locations of the in-situ wind measurements used for validation of modelled wind data. Green (dark green) dots (triangles) represent the position of in-situ surface (depth-averaged) currents from HFR (ADCP) observations. The isobaths of 50 m, 100 m and 200 m are represented as thin black lines. The land topography is represented in shades of grey. For the general location, see inset (IP: Iberian Peninsula; NWA: northwest of Africa; GoC: Gulf of Cádiz; SG: Strait of Gibraltar).

3.2 Background to the area

3.2.1 Geographical setting

The NMGoC lays along the southern Atlantic coast of Portugal and Spain. It extends from CSV, where the coastline orientation changes from meridional to zonal at the southwest tip of the Iberian Peninsula, to the Strait of Gibraltar in the east (Figure 3.1). The topography of the region

is marked by the presence of a zonally orientated coastal mountain range. The continental shelf consists of two distinct physiographic elements separated by Cape Santa Maria (CSM) where the shelf is the narrowest (5 km wide): a western bight, characterised by a relatively narrow shelf (<30 km) with a steep slope, and an eastern bight where the shelf is comparatively wider (>40 km), and the slope is gentler (Figure 3.1). The shelf break roughly corresponds to the 200 m isobath.

3.2.2 Wind patterns

The wind regime in the NMGoC region is mainly regulated by the Azores anticyclonic high-pressure cell position and intensity (Chase, 1951). During spring and summer (from March to August, typically) the Azores high displace north, increasing the pressure difference between the centre of the anticyclone and the Iberian Peninsula. This atmospheric set up produces a dominant wind regime characterized by relatively strong northerlies along the west coast of Portugal and at the Gulf of Cádiz entrance (Mazé et al., 1997; Fiúza et al., 1982). Due to the development of a thermal low in the centre of the Iberian Peninsula (Hoinka and De Castro, 2003) and to the presence of the coastal mountain range (Relvas and Barton, 2002; Fiúza, 1983), the northerlies rotate anticlockwise to north-westerlies towards the east of the gulf (de Oliveira Júnior et al., 2021; Sánchez and Relvas, 2003). During winter the Azores High displaces southward and weakens while the Iceland Low intensifies. This pattern favours the development of westerlies and an increased number of frontal systems that causes an overall variable wind regime (Chase, 1951; Losada, 1999) in the region.

Another recurrent wind pattern that is often observed in the region is the so-called “Levanter” produced by a variety of atmospheric set up (Trigo and DaCamara, 2000; Losada, 1999) but is highly controlled by the complex interaction of the wind with the local topography at the Strait of Gibraltar (Dorman et al., 1995; Capon, 2006). Levanter typically blows from the east or southeast (Peliz et al., 2009b, 2014) along the NMGoC without clear seasonality (de Oliveira Júnior et al., 2021; Ribas-Ribas et al., 2011).

3.2.3 Circulation patterns

Observations and numerical experiments have shown the existence of an equatorward current (so-called the Gulf of Cadiz Current, GCC hereafter) along the continental slope of the NMGoC

all year round (de Oliveira Júnior et al., 2022; Cravo et al., 2013; García-Lafuente et al., 2006; Peliz et al., 2009a, 2007; Criado-Aldeanueva et al., 2006a; Garcia et al., 2002; Criado-Aldeanueva et al., 2009; Peliz et al., 2009b). Over the western bight, the GCC magnitude and width are seasonally modulated being strong and extending significantly offshore in summer, but weak and restricted to the upper slope in winter (de Oliveira Júnior et al., 2022; García-Lafuente et al., 2006). Over the eastern bight, the flow veers anticyclonically following the slope orientation (Relvas and Barton, 2002; Criado-Aldeanueva et al., 2009, 2006a; Fiúza, 1983; Peliz et al., 2009a, 2007; Sánchez and Relvas, 2003; Garcia et al., 2002). The year-round presence of the GCC suggests that it results from the temporal alternation of different forcing. The flow is often described as the continuation of the geostrophic upwelling jet that originated along the western coast that turns cyclonically at CSV to satisfy potential vorticity conservation (Sánchez et al., 2006; Relvas and Barton, 2002; García-Lafuente et al., 2006; Sánchez and Relvas, 2003). Numerical simulations suggest that part of the Atlantic water is entrained by the denser Mediterranean outflow below and stirs the GCC due to mass conservation (Kida et al., 2008; Peliz et al., 2007, 2009a). Moreover, wind stress curl produced near CSV probably affects the slope circulation at the western bight during the upwelling season (Criado-Aldeanueva et al., 2006a; García-Lafuente et al., 2006; Sánchez et al., 2007, 2006; Sánchez and Relvas, 2003; de Oliveira Júnior et al., 2022).

Near the coast, the circulation is characterized by polarised alongshore subtidal flows which are generally balanced in the poleward (broadly westward) and equatorward (broadly eastward) directions (except in the vicinity of CSM where equatorward flows, EFs hereafter, dominate) without seasonality (Garel et al., 2016; de Oliveira Júnior et al., 2022, 2021). EFs are generally associated with upwelling events, generated locally or remotely, and advect cold water over the margin (Relvas and Barton, 2002; Fiúza, 1983). High-frequency radar observations show that these flows typically extend across the entire shelf and merge with the GCC (de Oliveira Júnior et al., 2022). By contrast, PFs are generally confined to the shelf and are associated with the advection of warm water in a narrow band of about 20–30 km leaning along the coast in summer (de Oliveira Júnior et al., 2022; Relvas and Barton, 2002; García-Lafuente et al., 2006; Fiúza, 1983). PFs are often referred to as CCCs as they have opposed directions to the permanent GCC over the slope (de Oliveira Júnior et al., 2022). These CCCs are produced by the imbalance of an alongshore pressure gradient during the relaxation (or reversal) of upwelling-favourable

winds (Relvas and Barton, 2002; García-Lafuente et al., 2006; Garel et al., 2016; Sánchez et al., 2006) and are enhanced by easterlies (Teles-Machado et al., 2007). At the western bight, the CCCs and GCC form of a cyclonic recirculation cell that develop during the relaxation of upwelling favourable winds (de Oliveira Júnior et al., 2022) and occupies most of the shelf and upper slope water column (García-Lafuente et al., 2006). At the eastern bight, scarce observations also support that the CCCs and GCC form a similar cyclonic cell (García-Lafuente et al., 2006).

3.3 Data and methods

3.3.1 Wind

Wind data was obtained from the regional weather forecasting system SKIRON, developed at the Helenic National Meteorological Service (Kallos et al., 2006; Papadopoulos et al., 2002). SKIRON is a non-hydrostatic numerical weather prediction model (Janjic et al., 2001) that includes a 3D data assimilation package to produce 7 days forecasts of high-resolution (5 km) analysis fields (wind, air temperature, specific humidity, total cloud cover, sea level pressure, total precipitation, upward and downward long wave flux, evaporation, latent heat flux and sensible heat flux). For the present study, only the daily forecast outputs of hourly wind data at 10 m height (u and v components) for the 2013-2020 period are considered. During the downloading process, some files were corrupted, producing some gaps in the time series up to 4 months in 2017. For unbiased seasonal comparisons, the entire year of 2017 was discarded (grey band in Figure 3.2a). The remaining 75 gaps (dots in Figure 3.2a) range from 2 h to 241 h (total of 2,160 h, representing 3.6% of the considered time series), with most gaps (87%) shorter than 26 h (Figure 3.2b).

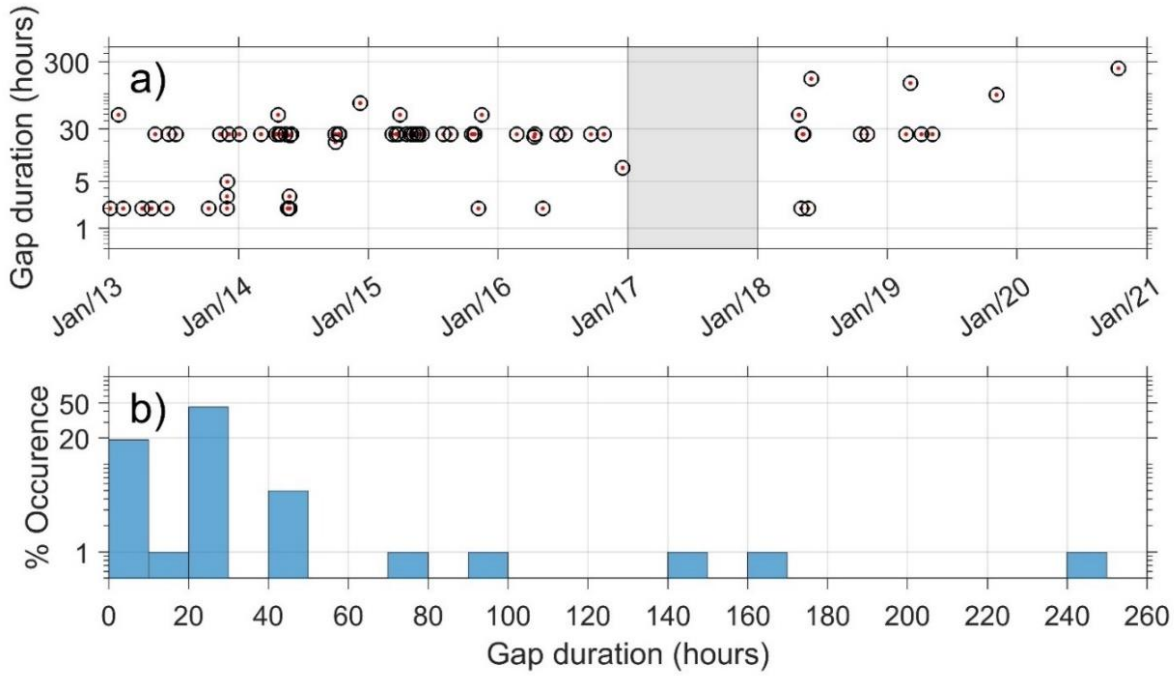

Figure 3.2 - SKIRON gaps duration throughout the considered time series (a). Percentage of occurrence of the gaps classed by durations of 10 h (b).

For validation at the NMGoC, the u and v components of the SKIRON wind were compared with concomitant hourly measurements from the ASCAT scatterometer (on board of MetOp-A satellite) and two offshore buoys. ASCAT records were obtained from the daily L3 files at the Remote Sensing Systems website (https://remss.com/, last access 10 January 2023) in grids with 0.25° (28 km) spatial resolution which includes measurements of u and v component and rain flags from both the descending and ascending passes. In-situ observations originate from the Faro buoy, operating since 2014 at the centre of the Gulf of Cadiz, and the Cadiz buoy installed further east in 2008 (see Figure 3.1). The measurements, at 3 m high, were extrapolated to 10 m considering a typical Hellmann exponential law. The validation was performed using approximately 5,000 concomitant records from ASCAT, 39,134 records from the Faro buoy and 52,992 records from the Cadiz buoy.

The SKIRON outputs and measurements compare well (Figure 3.3), with a Pearson's correlation coefficient (R) $\geq$ 0.7 for both the u and v components. In particular, the model reproduces with accuracy the daily wind fluctuations (Figures 3.3a and 3.3b). Minimum correlations are found for the ASCAT u component near CSV (R = 0.73, Figure 3.3c) where northerlies dominate, and near CSM (R = 0.7, Figure 3.3d) where the v component is relatively

weak. This overall good correlation between modelled and measured winds shows that SKIRON can reproduce reasonably well the main features associated with the wind variability over the NMGoC.

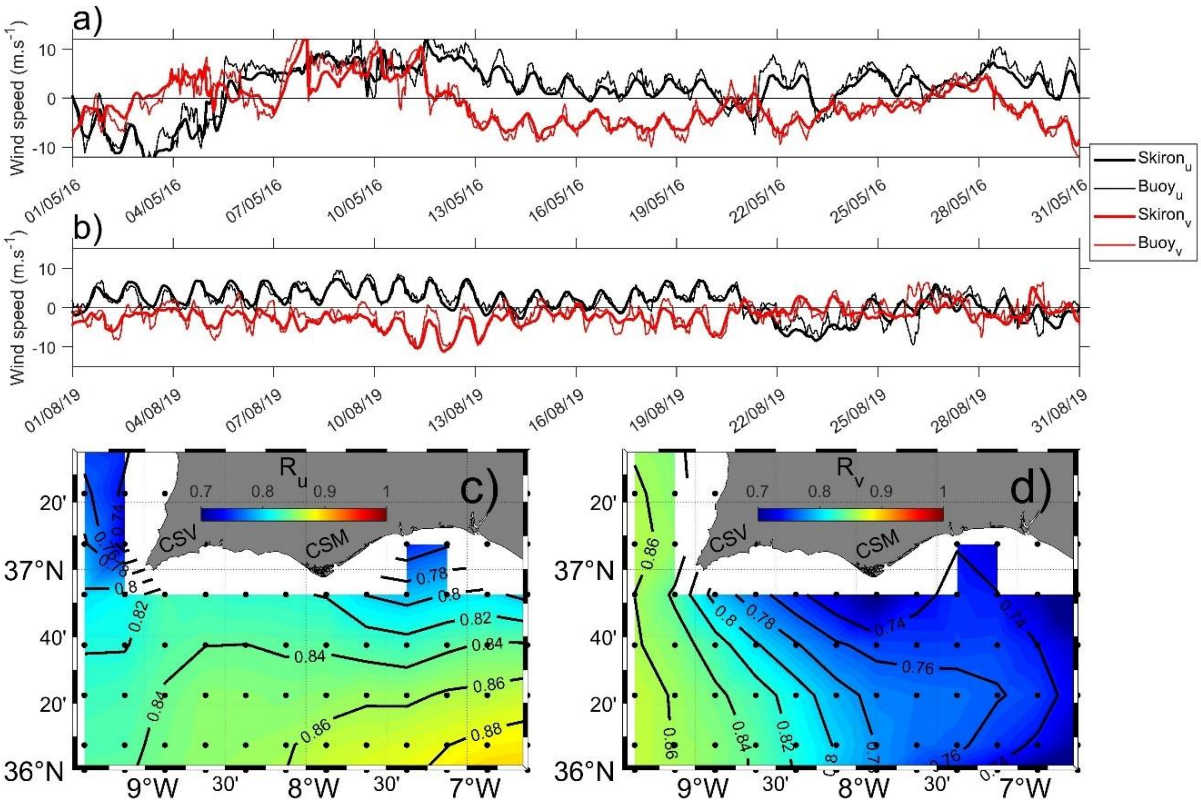

Figure 3.3 - Comparisons of SKIRON winds (thick lines) with buoy measurements (thin lines) at Faro buoy (a) and Cadiz buoy (b). Black (red) represents the u (v) component. Pearson's correlation coefficient between SKIRON and Ascat winds for the u (c) and v (d) components.

3.3.2 Ancillary data

Daily satellite altimeter SLA produced by AVISO were downloaded from CMEMS (Copernicus Marine Environment Monitoring Service). The SLA (product identifier: SEALEVEL_EUR_PHY_L4_MY_008_068) is an L4 gridded reanalysis product with 0.125° (14 km) spatial resolution computed with respect to a twenty-year mean (1993-2012). It is estimated by optimal interpolation merging the L3 along-track measurements from different altimeter missions.

The daily SST was obtained from an L4 product (identifier: SST_MED_SSTA_L4_NRT_OBSERVATIONS_010_004) consisting of merged multi-sensor

data and optimally interpolated SST fields, also available at CMEMS. The data is provided at 0.0083° (<1 km) spatial resolution and is representative of night-time SST values (00:00 UTC), the so-called foundation SST, nearly free of diurnal warming.

Hourly surface currents measured by High-Frequency Radars (HFR) with a spatial resolution of approximately 1.5 km were obtained from Puertos del Estado for the 2016-2020 period. In-situ hourly current records were also obtained from ADCPS (TRDI Workhorse 600 kHz and Sentinel V 500 kHz) deployed near the bed at 2 stations on the inner shelf in water depths of 20–23m (see Armona and Cacela, green triangles in Figure 3.1).

3.3.3 Processing

ASCAT records with detected rain and wind speed less than 2 $m.s^{-1}$ were discarded due to imprecisions of the sensor under these conditions (KNMI, 2007). The ADCP velocities were depth-averaged after a thorough quality check (for details, see Garel et al. 2016). Likewise, for details on the HFR data processing (i.e. verification of gaps, interpolation, and data validation) see de Oliveira Júnior et al. (2022). To remove high-frequency oscillations, the data (wind, SST, SLA and currents) were low-pass filtered using a Butterworth filter with a 7-day cut-off period. This cut-off period removes high fluctuations of the wind that are not important and allows for the larger fluctuations (about one week or more) that correspond to the period of significant temperature changes observed in the region (for example see Figures 3c and 8c in Garel et al. 2016). The seasonal analysis was performed considering each season to be defined as winter: 1 December–28 February; spring: 1 March–31 May; summer: 1 June–31 August; and autumn: 1 September–30 November).

3.3.4 Quantification of Ekman Transport and Ekman Pumping

The Ekman theory assumes that the ocean is forced by a steady wind and that the only forces acting are the frictional stresses between layers and the Coriolis force. This assumption corresponds to a linear, homogenous ocean in a steady state, with no lateral gradients and a laterally infinite domain (Bakun, 1973; Simpson and Sharples, 2012). For these conditions, using a locally valid Cartesian coordinate system with x, y, and z aligned eastward, northward,

and upward, respectively, and with the corresponding fluid velocity components denoted by u, v, and w, respectively, the equations of motion are:

$$\mathrm{fu} = -\frac{1}{\rho}\frac{\partial \tau_y}{\partial z}, \mathrm{fv} = \frac{1}{\rho}\frac{\partial \tau_x}{\partial z} \quad (1)$$

where f is the Coriolis parameter, ρ is the density of seawater and τ_x and τ_y represent wind stresses in the eastward and northward directions, respectively, with:

$$\tau_x = \rho_a \mathrm{Cd}|V_a|u_a \quad (2)$$

$$\tau_y = \rho_a \mathrm{Cd}|V_a|v_a \quad (3)$$

$V_a = (u_a, v_a)$ represents the wind speed vector, ρ_a the air density and Cd a wind stress drag coefficient based on Large and Pond (1981) modified for low wind speeds as in Trenberth et al. (1990):

$$\mathrm{Cd} = 0.00218 \text{ for } |V_a| \leq 1 \text{ m}.s^{-1}$$

$$\mathrm{Cd} = (0.62 + 1.56|V_a| - 1)\, 0.001 \text{ for } 1 \text{ m}.s^{-1} < |V_a| < 3 \text{ m}.s^{-1}$$

$$\mathrm{Cd} = 0.00114 \text{ for } 3 \text{ m}.s^{-1} \leq |V_a| < 10 \text{ m}.s^{-1}$$

$$\mathrm{Cd} = (0.49 + 0.065|V_a|)\, 0.001 \text{ for } |V_a| \geq 10 \text{ m}.s^{-1}$$

Integrating Eq. (1) over the Ekman depth (i.e., where the surface stress is acting significantly) results in relationships for the northward and eastward volume transports per unit of length called the Ekman transport $\overline{\mathrm{Ek_T}}$ = (Ek_{Tx}, Ek_{Ty}; units of $m^3.s^{-1}$ per meter of coast) as a function of the eastward and northward surface wind stress, respectively:

$$\mathrm{Ek}_{Tx} = -\frac{\tau_y}{\rho f}, \mathrm{Ek}_{Ty} = \frac{\tau_x}{\rho f} \quad (4)$$

Eq. (3) predicts an integrated transport directed 90° to the right (left) of the surface wind stress in the northern (southern) hemisphere. For winds parallel to the coast, offshore (onshore)

Ekman transport results in cross-shelf mass flux divergence (convergence) that must be compensated by mass flux convergence (divergence) in the vertical direction. Thus, the cross-shore wind-driven Ekman transport is equal to the vertical transport into the Ekman layer. Similarly, divergence (convergence) also occurs away from the coastal boundary under a spatially heterogeneous wind field that generates vertical velocities, called Ekman pumping velocities (w_{Ek} in m.s^{-1}), that is proportional to the wind stress curl:

$$w_{Ek} = \left(\frac{1}{\rho f}\right) \nabla \times \tau \quad (5)$$

Where $\nabla \times \tau = \frac{\partial \tau_y}{\partial x} - \frac{\partial \tau_x}{\partial y}$ and $\times$ represents the cross-product and ∇ the nabla operator.

$\overline{Ek_T}$ and w_{Ek} were calculated at every wind grid node using Eq. (4) and Eq. (5), respectively, with ρ = 1025 kg.m^{-3}. Comparisons between Ekman transport and Ekman pumping mechanisms were made in terms of alongshore variability of upwelling intensity considering the shelf region between 9°W and 7°W of longitude. It is noted that the coastline and shelf break are roughly orientated in the east-west direction within the selected limits and that bathymetry and topographic features are generally smaller than the ~25 km local Rosby radius of deformation (Sánchez and Relvas, 2003).

Hence, the upwelling intensity from the cross-shelf Ekman transport was represented as EkT_y along the 50 m isobath (Figure 3.1 black circles), where the depth is assumed to be greater than the Ekman depth. The upwelling intensity due to the pumping mechanism was estimated by converting w_{Ek} to Ekman pumping transport (EkP_T in m^3.s^{-1} per meter of coast) in order to directly compare the two upwelling processes (Pickett and Paduan, 2003). w_{Ek} was integrated from the 50 m isobath to a selected offshore limit at 36°48'N latitude that corresponds to the shelf slope (Figure 3.1, red dots) and roughly to the offshore limit of the cold water signal along the NMGoC during upwelling events (see Vargas et al., 2003). Following the Cartesian coordinate system, positive values of Ek_{Ty} represent downwelling favourable conditions while positive EkP_T represent upwelling favourable conditions. For simplification, Ek_{Ty} is multiplied by -1 (for positive values to represent upwelling conditions as EkP_T) and will be referred to as Ek_T (without the overbars). Finally, the total alongshore upwelling intensity (or total transport) was calculated as the sum of Ek_T and EkP_T.

3.4 Results

3.4.1 Upwelling and downwelling favourable conditions

The variability of the low-pass filtered wind over the NMGoC is briefly described in this section to aid the visualization of the seasonal wind variation and the typical conditions for upwelling and downwelling events associated with Ekman transport and Ekman pumping mechanisms. The seasonal wind roses presented in Figure 3.4 show the clear year-round dominance of the winds from the north (mostly from 300° to 360°) over the western region. Eastward, the dominant wind direction is generally from west - northwest. The most distinct seasonal patterns are observed between winter and summer (Figures 3.4a and 3.4c). In summer, in regions west of 9°W, winds are from the north and often >7.5 $m.s^{-1}$ producing strong and persistent upwelling favourable conditions over the Portuguese west coast. The dominant northerly rotates anticlockwise and weakens importantly. Such an inhomogeneous field causes surface divergency and promotes upwelling due to pumping mechanism independent of the coastline orientation. An example of a typical summer day with highly heterogeneous wind is presented in Figure 3.5a. The variability of wind magnitude and direction near CSV and east of CSM creates a positive and negative wind stress curl, respectively (Figure 3.6d). It is also noted that in summer easterlies are scarce.

In winter (Figure 3.4a) wind directions are the most variable, with velocities often above 5 $m.s^{-1}$ along the NMGoC. The importance of easterlies (Levanter) increases practically everywhere in comparison to the other seasons. At the NMGoC, easterly events (Figure 3.5b) promote downwelling conditions through onshore $\overline{Ek_T}$ and negative wind stress curl that is generally moderate along the coast (Figure 3.5e). Despite the overall variable winds in winter, winds from the north quadrant largely prevail over the western region.

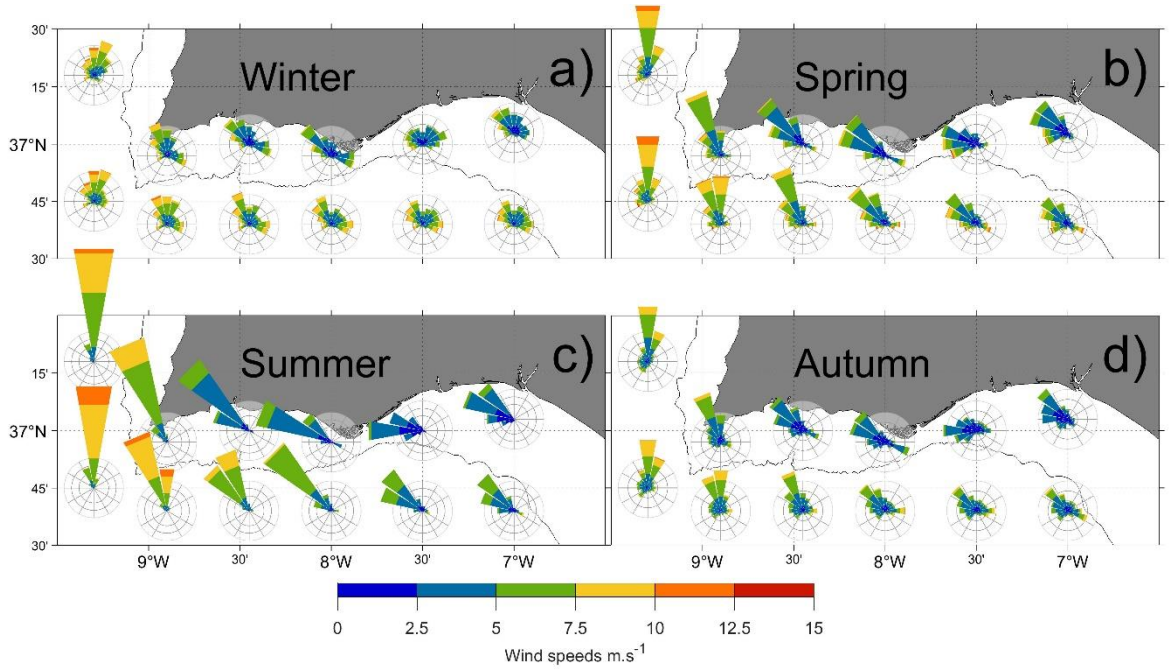

Figure 3.4 - Seasonal wind roses from the hourly SKIRON modelled data (low-pass filtered at 40h), represented with the meteorological convention (i.e. wind provenance). Rings represent 5% 10% and 20% of occurrence.

Also relevant for this study are the events associated with westerlies that promote significant upwelling through offshore $\overline{\mathrm{Ek_T}}$ as winds are parallel to the coast (as exemplified in Figure 3.5c). The associated wind stress curl in the coastal region is generally weak and is confined to a narrow band over the shelf (Figure 3.5f). Strong westerly events occur generally in winter and spring as indicated by the magnitude of winds from the 270° direction (Figure 3.4a-b). In summer and autumn, the western component is weak, however dominant (Figure 3.5c-d), and prolonged events may also be important to promote coastal upwelling through offshore $\overline{\mathrm{Ek_T}}$.

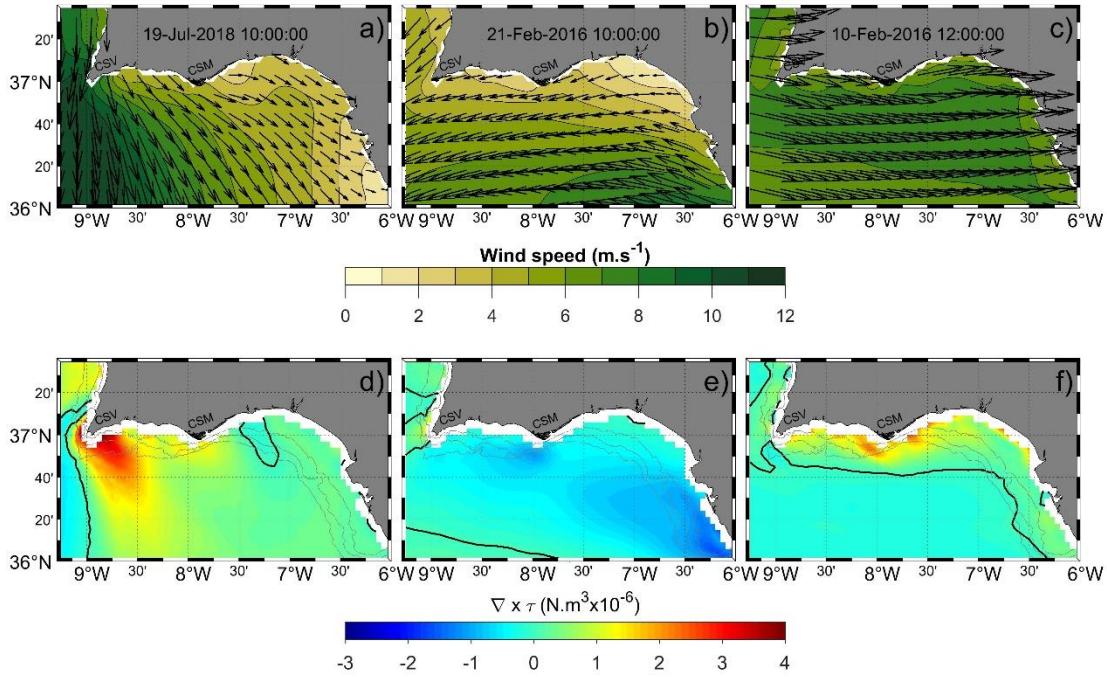

Figure 3.5 - Upwelling and downwelling favourable conditions from low-pass-filtered SKIRON modelled wind data (top) and the associated wind stress curl magnitude (bottom). Positive (negative) values in red (blue) represent upwelling (downwelling) patterns.

3.4.2 Patterns of the $\overline{Ek_T}$

The overall pattern of the $\overline{Ek_T}$ at the NMGoC is defined by westward transport in regions west of 8°W that veers to the south or south-westward at east (Figure 3.6a-d). This pattern is modulated seasonally with westward transport at the western region being strongest during spring and summer (Figures 3.6b and 3.6c) and weakest in winter and autumn (Figures 3.6a and 3.6d). The region of strongest westward mean summer transport is in the vicinity of CSV with values ≥ 0.9 $m^3.s^{-1}.m^{-1}$ (red contours in Figure 3.6c). At this location (approximately at 9°W 37°N) the shelf is narrow, and the slope is oriented in the NS direction indicating that significant upwelling takes place at this region of maximum offshore transport. Strong upwelling also extends further south of CSV due to the divergence of transport magnitude. For instance, $\overline{Ek_T}$ differences about 0.3-0.5 $m^3.s^{-1}.m^{-1}$ exists between 8°30'W 36°50'N and 9°W 36°50'N which are less than 25 km apart.

Compared to the CSV region, the magnitude of the $\overline{\mathrm{Ek_T}}$ is generally weak year-round at the eastern region, especially over the shelf where the mean transport is typically below 0.3 $m^3.s^{-1}.m^{-1}$. However, this weak transport is broadly in the cross-shore direction, thus upwelling favourable, along the entire coast.

3.4.3 w_{Ek} patterns

Along the shelf w_{Ek} are mostly weak and positive (upward), except for a small weakly negative region around 7°30'W and the region near CSV that are always associated with the strongest positive values (Figure 3.6e-h). w_{Ek} near CSV are strongest in spring and summer with the highest values >1x10^{-5} m.s^{-1} and >1.5x10^{-5} m.s^{-1} respectively (Figure 3.6e-f). This upwelling centre is skewed in the eastward direction, indicating that curl-driven upwelling will be more important along the southern than the western Portuguese coast. Offshore, w_{Ek} are generally positive and weak, except at the south-western region which is marked by permanent weak negative (downward velocities) in all seasons.

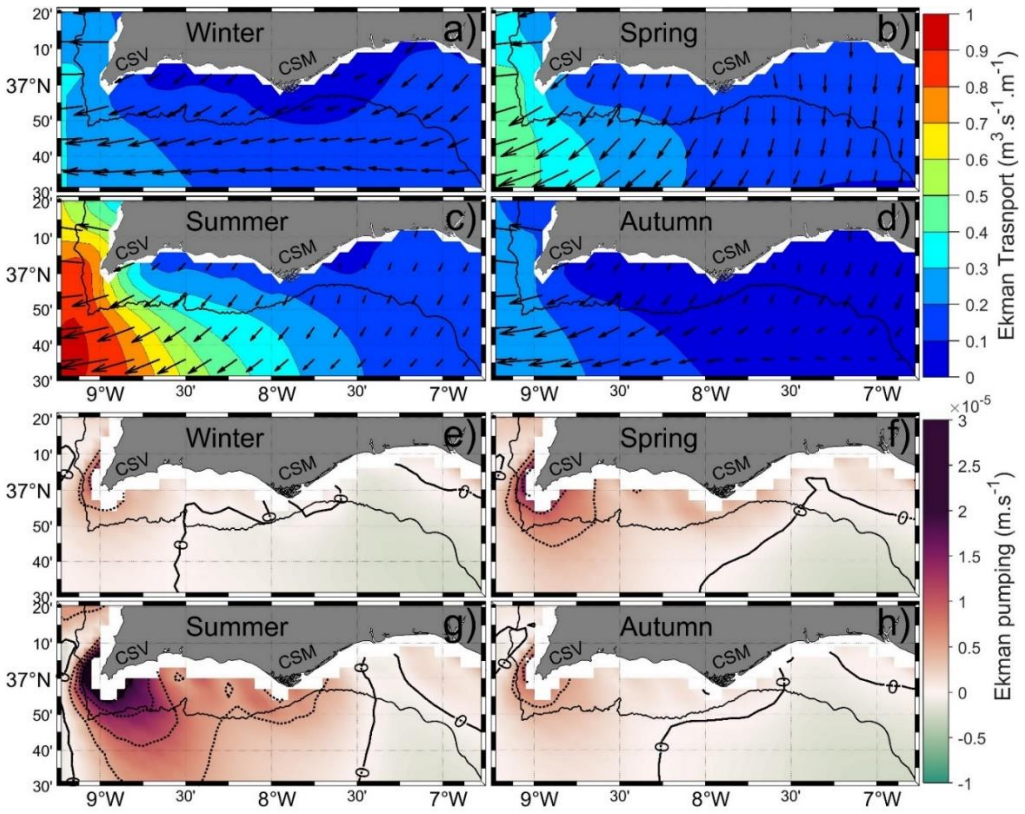

Figure 3.6 - Seasonal $\overline{Ek_T}$ (a-d) and w_{Ek} (e-h) with doted coutours representing 0.5x10^{-5} m.s^{-1} intervals and solid black contour representing the zero w_{Ek} line.

3.4.4 Alongshore variability of upwelling intensity

To assess the seasonal variability of the contributions from both Ek_T and EkP_T mechanisms to the total upwelling intensity over the shelf, these parameters are plotted alongshore for each season in Figure 3.7. Ek_T is twice as strong in spring and summer (about 0.2 $m^3.s^{-1}.m^{-1}$) than in autumn and winter (Figure 3.7a). Although the $\overline{Ek_T}$ magnitudes in spring and summer are largest at the west (Figure 3.6 b-c), the clockwise rotation of vectors diminishes the contribution to the cross-shore component, justifying the invariant Ek_T observed along the shelf. The Ek_T standard deviation (STD) is evenly distributed along the coast with the highest values observed in spring and winter (approximately 0.4 $m^3.s^{-1}.m^{-1}$) and lowest in summer ($\leq$ 0.2 $m^3.s^{-1}.m^{-1}$, Figure 3.7b).

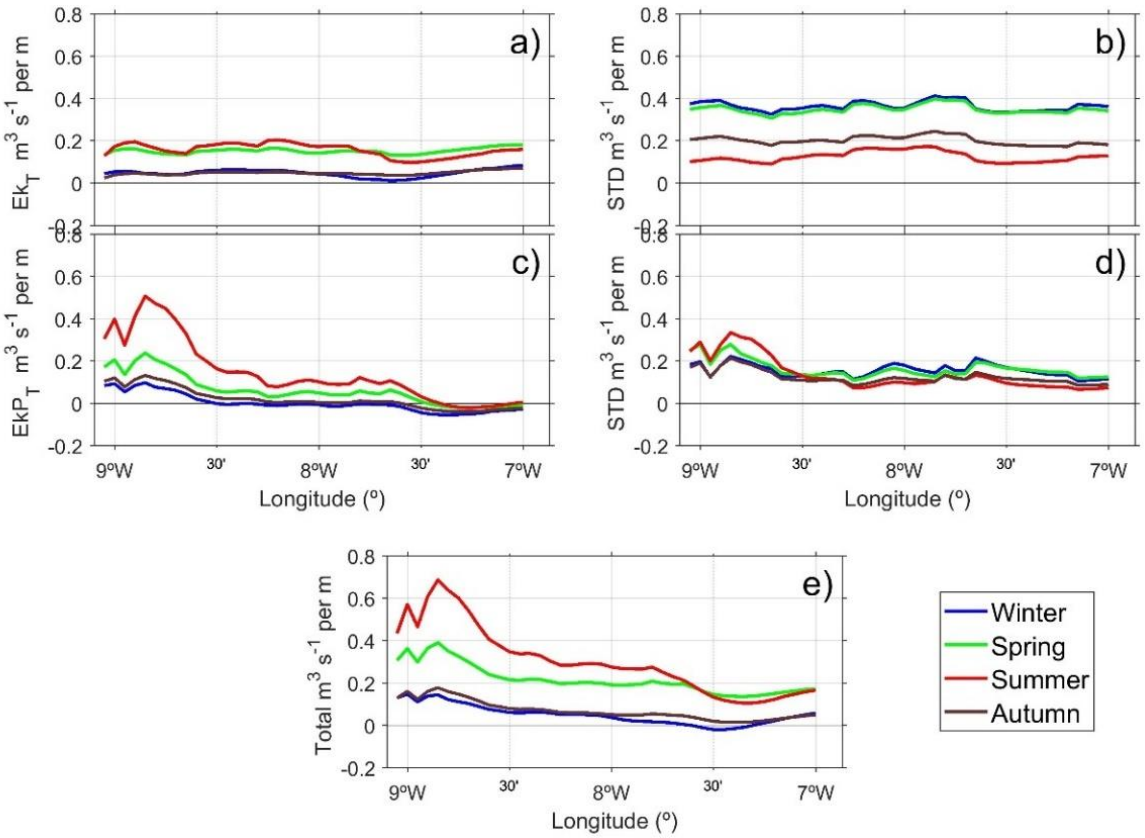

Figure 3.7 - Seasonal estimates of wind-driven alongshore upwelling intensity due to Ek_T (a) and EkP_T (c). Seasonal Total transport (e) and modulus of the STD from Ek_T and EkP_T (b and d respectively).

The low Ek_T STD in summer is explained by the steady wind pattern over the region that causes persistent weak (generally <0.5 $m^3.s^{-1}.m^{-1}$) upwelling favourable conditions sometimes lasting more than a month (see blue in Figure 3.8 from the end of June to the end of July 2018), being eventually interrupted by transient easterlies events that last around four days (i.e., 20 June,3 August 2018 and 20 August in Figure 3.8a). The relatively high values of STD in winter and spring are due to the alternation of events with strong (often >0.5 $m^3.s^{-1}.m^{-1}$) upwelling and downwelling favourable conditions (See Figure 3.9a). It is noted that the duration of downwelling events remains about four days.

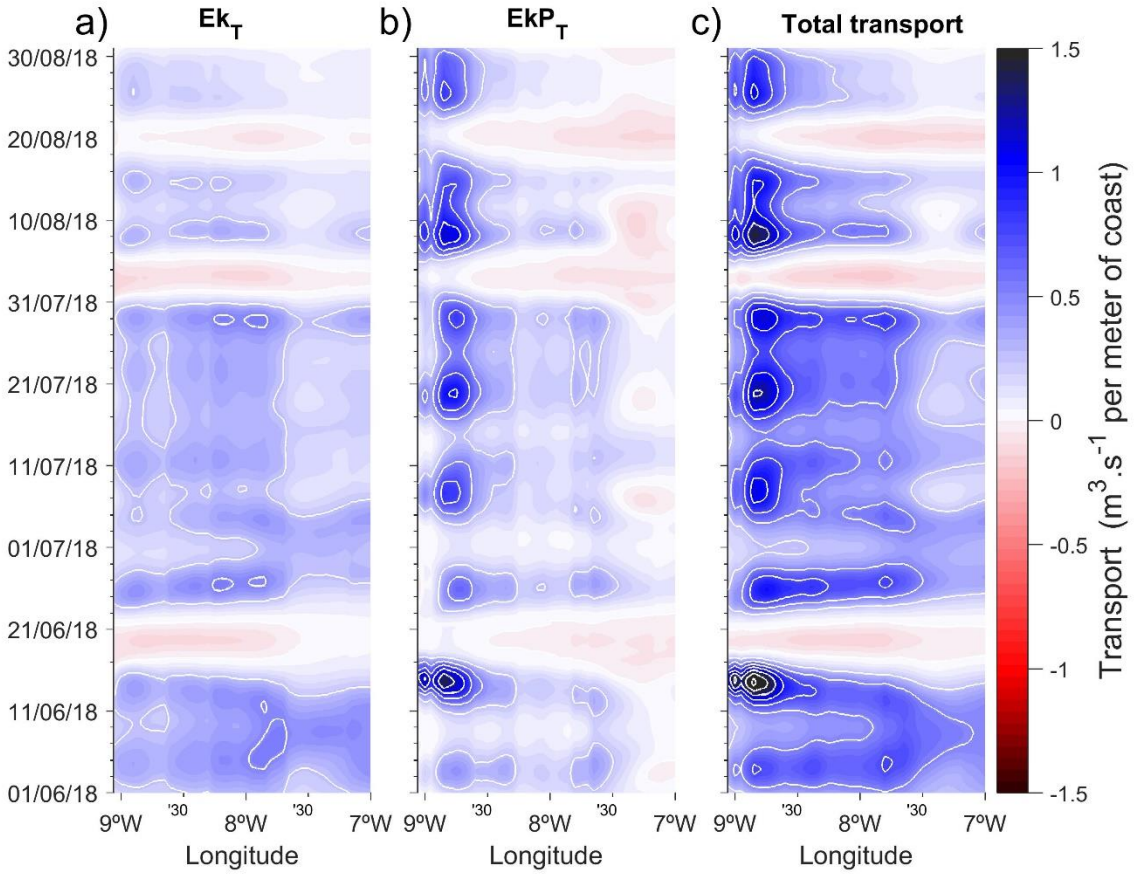

Figure 3.8 - Time variability of Ek_T (a), EkP_T (b) and Total transport (c) during the summer of 2018. Upwelling (downwelling) favourable conditions are represented in blue (red). Contours indicate 0.25 $m^3.s^{-1}.m^{-1}$ intervals and minor ticks indicate 2 days intervals.

EkP_T is strongest in summer and weakest in winter (Figure 3.7c). In all seasons, the highest values are observed near CSV, between 8°30'W and 9°W, and the lowest (broadly negative) values are observed east of 7°30'W. The maximum values (Figure 3.7c in red) are 0.5 $m^3.s^{-1}$

.m^{-1}, 2.5 times larger than the concurrent Ek_T. In this region near CSV, summer events are in general strong and often reach values >0.75 $m^3.s^{-1}.m^{-1}$ (see Figure 3.8b) supporting the dominant contribution from this mechanism to local upwelling. The overall low EkP_T STD values express low variability in time and along the coast. In winter, despite the alternation between upwelling and downwelling favourable conditions, EkP_T values are generally weak (often <0.25 $m^3.s^{-1}.m^{-1}$ see Figure 3.9b) and keep STD values low, while in summer low STD values are due to persistent upwelling favourable patterns (see Figure 3.8b).

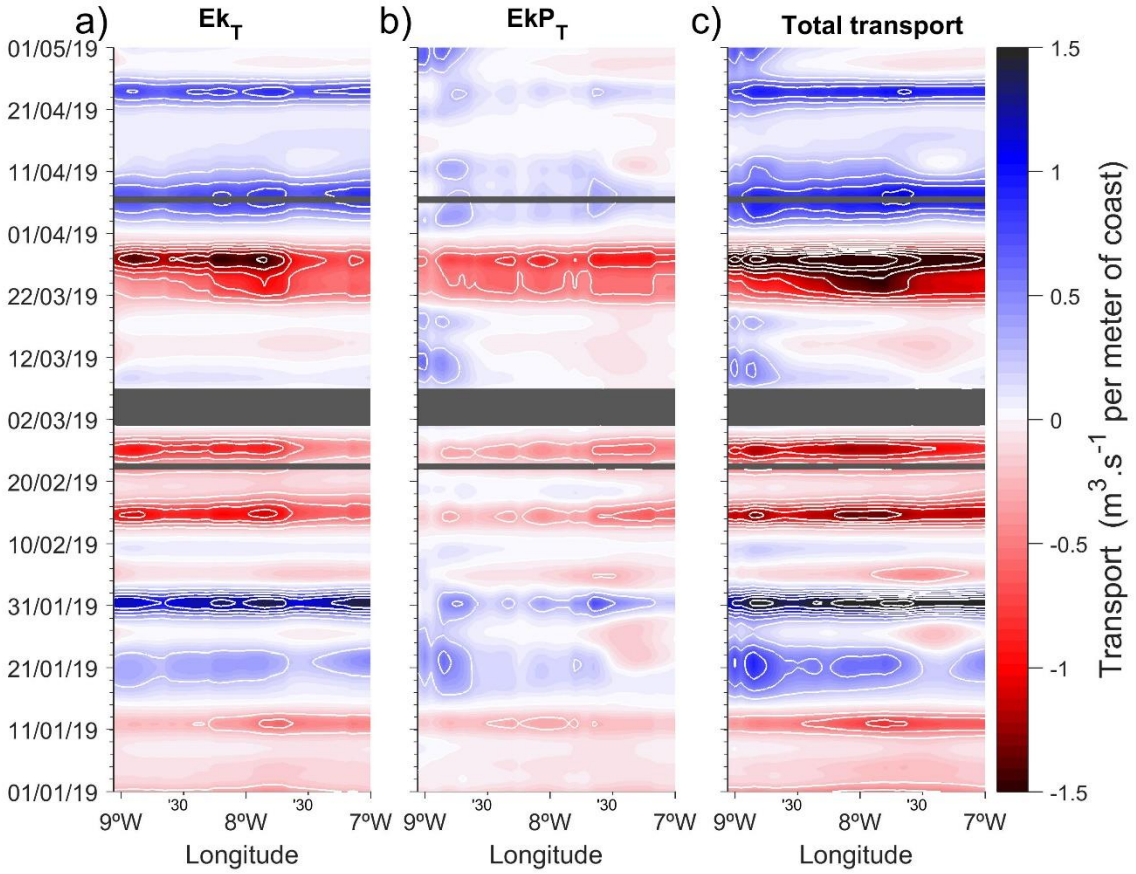

Figure 3.9 - Same as in Figure 3.8 but for the winter of 2015 and 2016.

The combined effects of Ek_T and EkP_T result in upwelling favourable conditions along the entire coast except in winter between 7°15'W and 8°W (Figure 3.7e) where the transport is negligible. Although the total transport is weakest in winter, it also results from the alternation of relatively strong positive and negative events (Figure 3.9c). Overall, the NMGoC has year-round coastal upwelling favourable conditions that are strongest near CSV with total transport reaching often 1 $m^3.s^{-1}.m^{-1}$ in summer (Figure 3.9c) due to strong EkP_T contribution. The overall

sharp decrease of EkP_T eastward of 8°30'W results in an alongshore gradient of the total upwelling intensity that is steepest in summer and smoothest in winter.

3.5 Effect of Ekman transport and Ekman pumping on the circulation

3.5.1 Shelf circulation

To evaluate the effect of Ek_T and EkP_T on the alongshore shelf circulation, the total transport is compared with SST, alongshore currents from HFR and ADCP, and SLA considering a 5-month period, from May to September 2019 (Figure 3.10). The selected period includes events with significant wind stress curl near CSV that produce an alongshore gradient in the total transport and events with upwelling favourable conditions evenly distributed along the coast (reflecting the effect of Ek_T). In general, when upwelling favourable events (blue in Figure 3.10) with moderate magnitude (<1 $m^3.s^{-1}.m^{-1}$) are observed along the entire coast, SST cooling is also observed over the corresponding area (see events on 08 May, 18 May and 7 July, blue arrows in Figure 3.10b), while for periods with strong upwelling favourable conditions restricted to the CSV region, the SST cooling is mostly observed west of 8°W (see events on 18 July, 02 August and 17 August, red arrows in Figure 3.10b). In the NMGoC the shelf circulation was previously described to respond to wind stress in the sense that westerlies prevent or hamper the westward progression of the pool of warm water from the eastern region (García Lafuente and Ruiz, 2007). The various examples presented in Figure 3.10 indicate that the extent of the warm (cold) water westward (eastward) is related to the intensity and the alongshore extent of upwelling favourable conditions. Multi-year SST statistical analyses of SST presented by Vargas et al. (2003) have shown that in winter cold waters are found stretching along the shelf following the patterns of the strong events with evenly distributed positive Ek_T along the coast (Figure 3.9a). Their results also indicate that in summer the coldest coastal waters are observed over the western bight and extend further south over the slope, following closely the pattern of w_{Ek} (Figure 3.6g). Towards the east, w_{Ek} tend towards zero at 7°30W in spring and summer (Figure 3.6f-g) resulting in a weak total upwelling intensity eastward of this location (Figure 3.7e). This specific position also delimits the extent of negative SST anomalies (Vargas et al., 2003) and the area with a probability to find upwelling spots

based on remotely sensed chlorophyll and SST (Ruiz and Navarro, 2006). The spatial and temporal correspondence between the SST and upwelling intensity supports that both Ekman transport and Ekman pumping affect importantly the shelf water circulation throughout the year.

The overall correspondence between upwelling favourable conditions (blue in Figure 3.10a) and the coastal EFs (Figure 3.10c) indicate that these flows are wind-driven as shown based on long-term in situ observations at Armona station (de Oliveira Júnior et al., 2021). On the contrary, the setup of PFs were mainly associated with weak transport at the eastern bight (white, Figure 3.10a) and persistent and strong upwelling favourable conditions at the western bight (i.e., 28 May, 30 June, 22 July and 05 August, indicated by black arrows nr. 1-4 in Figure 3.10c). At the end of Period 1, weak downwelling conditions prevailed along the entire shelf. However, PF reversals were observed before these downwelling conditions (see arrow nr. 5) confirming that these flows are not triggered by direct wind action. In most of these cases, PF reversals were associated with a SLA slope (Figure 3.10d) that seemed to be sustained by the persistent and strong upwelling favourable conditions at the western bight during June, July and August (Period 1 in Figure 3.10). During Period 1, SLA differences could reach up to 4 cm for approximately 110 km (between 7°30'W and 8°30'W), similar to estimates from tide gauges between the eastern and western bights (Relvas and Barton, 2002). In addition, such slope if acting alone on the flow (i.e. ignoring all the other terms of the momentum equation) produces a poleward acceleration of 2.6×10^{-6} $m.s^{-2}$ that is of the same order of magnitude as the acceleration during PFs reversals at Armona station (de Oliveira Júnior et al., 2021) and further supports that poleward CCCs are driven by an alongshore pressure gradient (de Oliveira Júnior et al., 2021; Garel et al., 2016; Relvas and Barton, 2002; García-Lafuente et al., 2006; Sánchez et al., 2006).

The correspondence between the SLA alongshore gradient and the alongshore gradient of total transport, which is largely dominated by the EkP_T in summer, suggests that the pressure gradient is partly produced by the wind stress curl, as proposed by Sánchez et al. (2006). Numerical simulations in the SBC have shown that the alongshore gradient of wind stress curl is an essential factor to produce an alongshore pressure gradient and consequently PFs (Wang, 1997; Oey et al., 2001; Oey, 1999). It is important to stress that additional factors than the wind stress curl may also generate an alongshore pressure gradient. For instance, a pressure gradient

may develop along the NMGoC due to buoyancy inputs at the eastern bight (Bellanco and Sánchez-Leal, 2016) resulting from the tidal pumping of warm water from large intertidal areas in summer (García-Lafuente et al., 2006) and anomalous river discharges in winter (Sánchez et al., 2006). The interaction of the upwelling jet generated at the Portuguese west coast with the alongshore variations in the topography may also induce a significant sea level variation in the vicinity of capes. At the Californian coast, this topographic effect was shown to produce negative alongshore pressure gradients and accelerate poleward coastal currents when the main upwelling favourable winds relax (Gan and Allen, 2002).

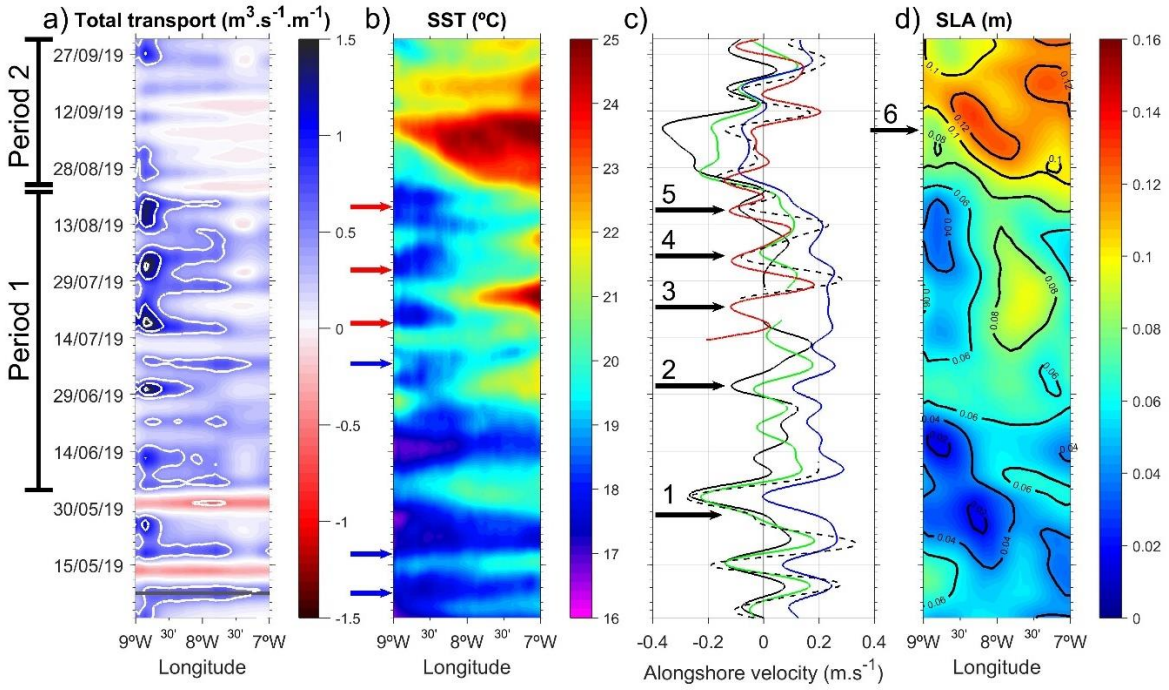

Figure 3.10 - (a) Hovmöller diagram for the Total transport (Ek_T + EkP_T). White contours represent 0.5 m.^{3}s^{-1}.m^{-1} intervals. (b) Hovmöller diagram for the SST averaged from the coast to the 36°48'N line that broadly represents the shelf break limit. Blue and red arrows represent different upwelling responses to the eastward extent of total transport. (c) Surface alongshore currents from HFR near CSV (black solid line), near 8°30'W (green solid line) and at CSM (blue solid line). Depth-averaged alongshore ADCP currents at Armona (black dashed line) and Cacela (red solid line) stations. For locations of current velocities see Figure 3.1. Black arrows from 1-5 represent poleward flow reversals as indicated in the text. (d) Hovmöller diagram of the SLA at the 36°56'N line. Contours represent 0.02m intervals. Black arrow nr. 6 represent a specific event of westward propagation of the sea level slope (see text). All data have been lowpass filtered using a (Butterworth) filter of 7 days cutoff period.

During Period 2 (from 21 August onwards in Figure 3.10), the transport was variable and alternated between weak upwelling and weak downwelling conditions. The (poleward) currents

were weak (<0.1 $m.s^{-1}$), except near CSV where their strong (>0.2 $m.s^{-1}$) magnitude was comparable to the situation during the well-developed downwelling events on 14 May and 01 June. The magnitude difference between currents at the west and at the east observed from 29 August to 08 September (Figure 3.10c) can be explained by the fact that the maximum alongshore pressure gradient has moved westward, being significant only over the western region between 8°49'W and 8°10'W (arrow nr. 6 in Figure 3.10d). This propagation of the sea level slope is consistent with continental shelf-wave dynamics for which a pressure perturbation propagates along an isobath with the coastline on its right. For example, during spring and summer in the region of SBC, the intensification of the alongshore wind stress and Ekman pumping promotes the shoaling of isopycnals which depth anomalies tend to propagate as Rossby waves when winds weaken at the end of the season (Di Lorenzo, 2003). The strong and localized effect of wind stress curl near CSV may therefore trigger the generation of a coastal trapped wave as suggested by Sánchez et al. (2006) and influences the circulation further north.

At the western bight, a cyclonic circulation cell is recurrently observed at the water surface when the wind relaxes (de Oliveira Júnior et al., 2022). This structure was shown to extend up to 300 m depth (García-Lafuente et al., 2006) and could result from the effect of the wind stress curl. A geostrophic cyclonic circulation is expected to develop as positive w_{Ek} should uprise the isopycnals in a circular shape (Criado-Aldeanueva et al., 2006a) as observed at the SBC (Di Lorenzo, 2003; Münchow, 2000). At the NMGoC, a permanent circular depression in the seasonal SLA (Figure 3.11) corresponds remarkably to the spatial and temporal patterns of the positive w_{Ek} (Figure 3.6), especially in summer (Figure 3.11c and Figure 3.6g). This depression produces a permanent alongshore slope along the NMGoC and a cross-shore-slope over the western bight. Further evidence of the wind stress curl effect on the mesoscale pressure field is provided by the dynamic topography computed in the vicinity of CSV during a synoptic survey in summer (Figure 5d in Relvas and Barton, 2005). A similar circular depression in the sea level is reported and is marked by a sharp alongshore gradient at 8°30W where the gradient of Ekman pumping is also the strongest (see Figures 3.6 and 3.7). Therefore, it is argued here that a similar response of the isopycnals to wind curl as observed in the SBC occurs at the NMGoC.

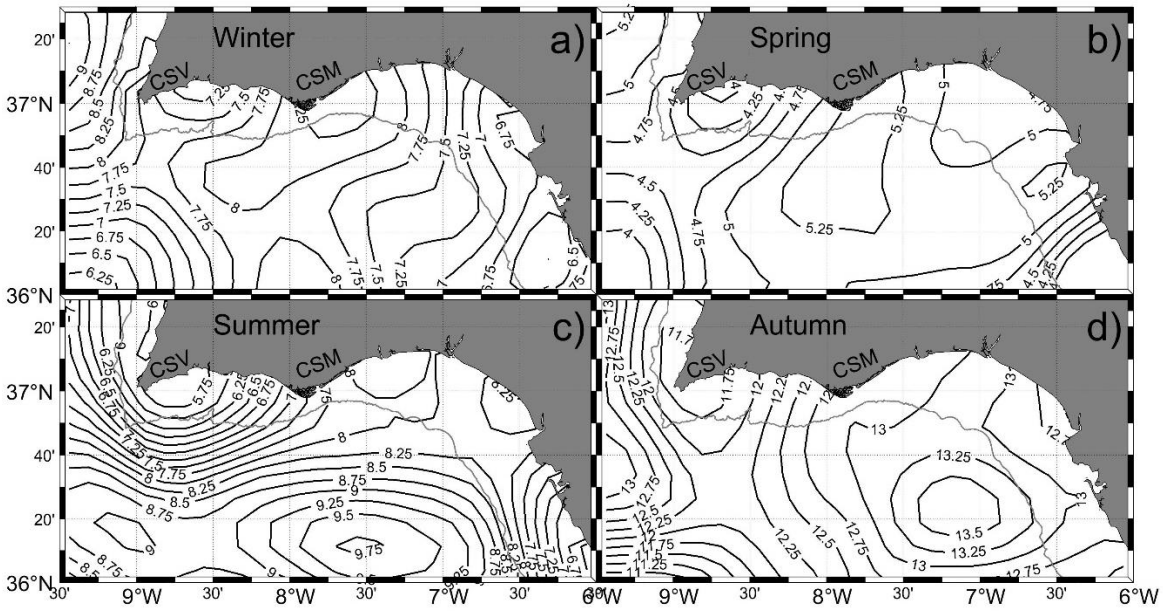

Figure 3.11 - Seasonal mean SLA. Contour lines represent 0.25 cm intervals.

3.5.2 GCC modulation

A recent study based on 4.5-year HFR data showed that the slope current, the GCC, is seasonally modulated at the western bight possibly due to seasonal changes in Ekman transport and Ekman pumping mechanisms (de Oliveira Júnior et al., 2022). This modulation is observed in the seasonality of the SLA (Figure 3.11) with a weak cross-shore pressure gradient over the shelf in winter (Figure 3.11a) and a strong pressure gradient over the shelf and slope in summer (Figure 3.11c). Owing to the similarities between SLA and w_{Ek}, the wind stress curl effect may be involved in the process that modulates the position and intensity of the GCC. Simplified two-dimensional modelling experiments performed to explore the role of wind stress curl in the separation of a coastal upwelling jet along the Oregon coast (Castelao and Barth, 2007), considered two different scenarios including and omitting the curl effect on the idealized upwelling favourable conditions. It was shown that southward (upwelling favourable) alongshore wind stress intensification and zero curl, promote an equatorward jet geostrophically balanced with the tilted isopycnals centred at the shelf break and slope (no separation). Simulations that included wind stress curl intensification, showed that the curl-driven upwelling causes isotherms to tilt upward in the offshore region, thus sustaining an intensification of the southward velocities via the thermal wind balance and controlling the

separation of the jet from the slope. To further explore the relationship between the different upwelling mechanisms and the slope circulation, an example containing an offshore migration of the GCC observed from HFR measurements is presented in Figure 3.12 together with the spatial and temporal variability of w_{Ek}, SST, Ek_T and SLA gradient along a cross-shore transect (at 8°30'W, approximately).

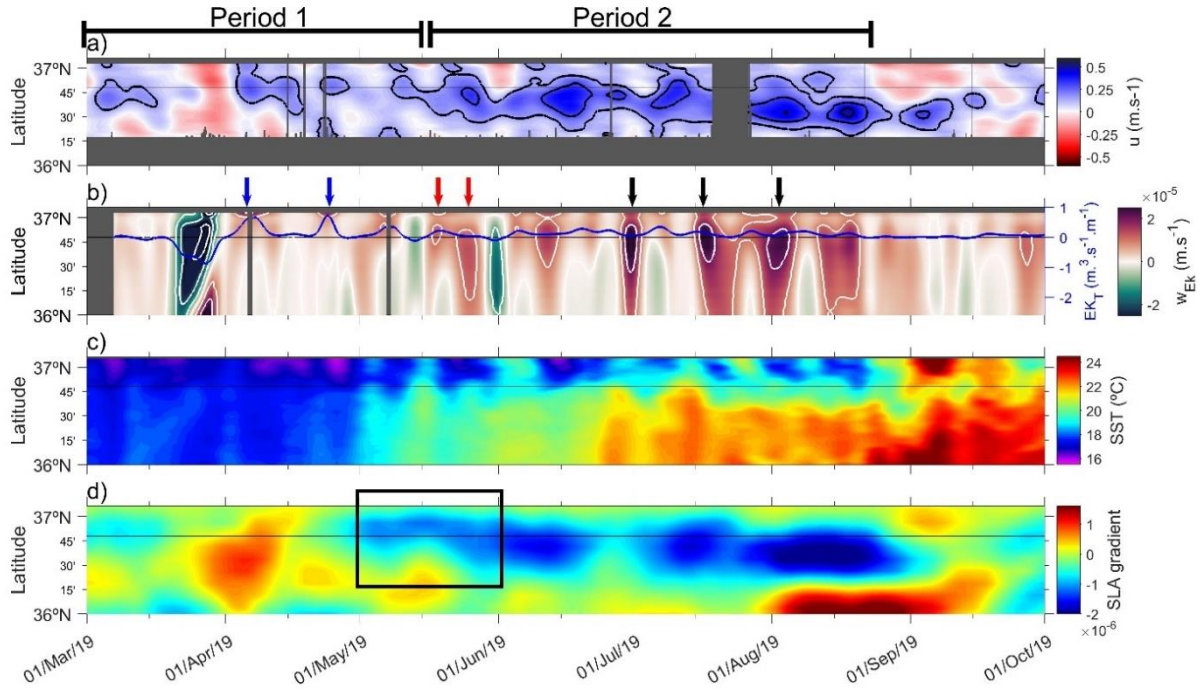

Figure 3.12 - Hovmöller diagram for the (a) zonal component of the surface current, (b) w_{Ek} and EkT_v (blue line right axis), (c) SLA gradient and (d) SST along a cross-shelf transect near 8°30'W for spring and summer 2019. The contour in (a) represent 0.15 m.s^{-1}, 0.3 m.s^{-1}and 0.45 m.s^{-1}. Contours in (b) represent 1x10^{-5} m.s^{-1} intervals and contours in (c) represent 0.02 m intervals. The horizontal black line indicates the 200 m depth, indicative of the shelf break limit that is 30 km from the coast. On the right axis in (b) black line also represents the zero EkT_v transport line. All data have been lowpass filtered using a (Butterworth) filter of 7 days cutoff period.

From 1 March to 15 May (Period 1 in Figure 3.12), the circulation was marked by several periods with a well-developed GCC (outlined with black contours in Figure 3.12a) close to the 200 m isobath (horizontal black line, indicating the shelf break limit at 30 km from the coast). During this period, w_{Ek} was mostly positive (upwelling favourable) and relatively weak (<1x10^{-5} m.s^{-1}, Figure 3.12b) with few strong events (w_{Ek} >1x10^{-5} m.s^{-1}) being observed at the inner shelf. Similarly, Ek_T was mostly positive (upwelling favourable) and two strong events were registered in April (blue arrows in Figures 3.12b). The coldest SST (Figure 3.12c) was always near the coast, and a moderate negative (higher sea level offshore) SLA gradient (-

0.5×10^{-6}) was generally observed over the shelf break (Figure 3.12d) in response to the overall upwelling favourable conditions. An exception to this pattern occurred at the end of March due to a strong downwelling (negative w_{Ek} and Ek_T) event that caused the slope to reverse sign and promoted westward currents along the entire transect. Therefore, the hydrographic features of the western NMGoC during Period 1 in Figure 3.12, corroborate the theoretical explanation for the development of a typical coastal upwelling circulation. More specifically, when the surface water divergence is restricted to the coastal boundary (due mainly to Ek_T and no significant curl off-shore), the cross-shore pressure gradient develops close to the coast and the circulation is marked by the development of a geostrophic upwelling jet over the shelf break (Castelao and Barth, 2007; Capet et al., 2004). Additional evidence that divergence restricted to the coastal boundary affects the NMGoC circulation is provided by the recurrently observed upward tilted isopycnals near the coast during winter surveys at the eastern bight (Santos, 2005; Silva et al., 2008). This stratification profile, typical of coastal upwelling, contributes to the persistence of the GCC in winter (Criado-Aldeanueva et al., 2009; de Oliveira Júnior et al., 2022).

In the example presented in Figure 3.12, the Ekman pumping effect became important during the second half of May (beginning of Period 2 in Figure 3.12) with the development of two strong events with w_{Ek} >1x10^{-5} m.s^{-1} (see red arrows in Figure 3.12b). These events were closely associated with the steepening and broadening of cross-shore SLA gradient (see black box in Figure 3.12d) and also the strengthening and widening of the GCC (Figure 3.12a). In the following months up to the end of September, w_{Ek} intensified and reached velocities >2x10^{-5} m.s^{-1} (see black arrows in Figure 3.12b) off the shelf break and caused the cross-shore SLA gradient to further increase. As a result, the GCC core moved offshore (up to 20 km from the shelf break) reaching velocities >0.45 m.s^{-1} (at the end of Period 2). The concomitant timing of the separation and w_{Ek}intensification, together with the overlapping area occupied by offshore strong w_{Ek} and SLA gradient support that the GCC at the western bight is affected locally by the wind stress curl effect following the dynamics proposed by Castelao and Barth (2007). Additional processes acting on the GCC include, amongst others, the effect of the west coast upwelling jet that is forced to turn cyclonically due to the conservation of potential vorticity near CSV (Sánchez and Relvas, 2003) and the mixing between the Atlantic water and the Mediterranean outflow over the eastern Gulf of Cadiz (Kida et al., 2008; Peliz et al., 2007, 2009a).

3.6 Conclusions

Winds from SKIRON, a high-resolution weather forecast model, were used to estimate the Ekman transport and Ekman pumping and to explore their effects on the circulation at the NMGoC. Due to the model's high spatial resolution, it was possible to resolve small-scale wind patterns induced by the irregular coastline and coastal topography. In general upwelling favourable conditions occurs along the study area. The strongest upwelling intensity occurs near CSV due to a persistent positive wind stress curl that promotes an alongshore gradient of upwelling intensity throughout the year but strongest in summer.

Over the western bight, due to strong Ekman transport events and comparatively weaker Ekman pumping (with highest values over the shelf) in winter, the surface water divergence is restricted to the coastal boundary. Consequently, the development of a cross-shore pressure gradient occurs close to the coast, and the offshore circulation is marked by a geostrophic upwelling jet, the GCC, at the upper slope. In summer, the Ekman pumping intensifies and promotes upwelling off the shelf. In response the sea level gradient extends offshore and contributes to the separation of the GCC. Therefore, the seasonal and spatial variability of the Ekman transport and Ekman pumping contributes significantly to the offshore position of the GCC at the western region.

The permanent and strong effect of Ekman pumping anchored at CSV is argued to sustain an overall circular depression in the sea level over the western bight as evidenced by satellite altimetry. The dynamic adjustment of this depression may favour the recurrently observed cyclonic circulation in the area. A permanent alongshore pressure gradient, which the magnitude in summer is comparable with tide gauge observations, is also associated with the depression and could effectively drive the alongshore poleward currents.

Overall, this study indicates that the circulation at the NMGoC is highly affected by the atmosphere-ocean interaction through modulation of the pressure field induced by spatially and temporally variable upwelling processes. Future work should be oriented towards obtaining long-term direct observations of the sea level variability.

Chapter 4 - The structure of incipient coastal counter currents in South Portugal as indicator of their forcing agents

Abstract

The alongshore subtidal water circulation along the South Portugal inner shelf is characterized by the temporal alternation of equatorward (i.e., broadly eastward) flows related to coastal upwelling processes and poleward (i. e., broadly westward) Coastal Counter Currents (CCCs). The objective of this study is to get insights about the main drivers of CCCs based on kinematic parameters describing the structure of the flow at the moment it changes direction. The parameters are derived from an extensive bottom-mounted ADCP dataset (16 de- ployments; 34,121 hourly records) collected at a single mooring (23 m water depth). Results show that the so-called incipient flows present contrasted general patterns whether they turn from equatorward to poleward or the opposite. Complementary observations at a nearby station indicate that these characteristics are spatially consistent along the studied area. Although 70% of CCCs are generated under favourable wind conditions (Levanter), these flows generally develop through the bed layer, in particular in summer. Hence, the Levanter wind - expected to promote flow setup through the surface layer - is not the main driver of CCCs in most cases. The general structure of incipient CCCs strongly suggests that the dominant force competing with the wind stress is an alongshore pressure gradient (APG). Furthermore, the maximum equatorward flow magnitude before CCCs setup is significantly correlated with the following (poleward) acceleration of incipient CCCs near the bed. Such relation is consistent with the development of CCCs due to the unbalance of an APG (produced during active upwelling) when wind relaxes. This process is further supported by an analysis of the depth-averaged momentum equation which suggests that the coastal circulation is mainly driven by linear dynamics in the region.

4.1 Introduction

At regions affected by coastal upwelling driven by intense and persistent favourable winds, the shelf circulation is characterized by an alongshore flow roughly aligned with the wind direction, dynamically linked to the upwelling process through geostrophic adjustment (Ekman, 1905; Kämpf and Chapman, 2016). Some of the major coastal upwelling systems worldwide, such as the Benguela (Boyd and Nelson, 1998; Fawcett et al., 2008), California (Largier et al., 1993; Melton et al., 2009; Send et al., 1987; Washburn et al., 2011) and Canary (Fiúza, 1983; Garel et al., 2016; Relvas and Barton, 2002) Currents, are characterized by frequent temporarily replacement of the upwelling circulation over the inner shelf by alongshore flows of opposite direction, referred to as coastal counter current (CCCs; Sverdrup and Fleming, 1941, cited in Hickey, 1979).

CCCs advect water (poleward, at eastern boundary systems) along the coast, displacing the previously upwelled, cool and nutrient-rich water offshore (Send et al., 1987). As such, these flows are typically observed as a tongue of relatively warm water, a few tens of km wide, leaning against the coast (Relvas and Barton, 2002; Send et al., 1987; García-Lafuente et al., 2006; Sordo et al., 2001; Boyd and Nelson, 1998; Stevenson, 1977). The alongshore advection of water from adjacent and shallow areas may cause rapid changes in water properties at short spatial and temporal scales over the inner shelf (Send et al., 1987; Melton et al., 2009; Relvas and Barton, 2002; Garel et al., 2016), with implications for ecosystem health and economic activities in the coastal zone (Wing et al., 1995; Mace and Morgan, 2006; Dudas et al., 2009; Washburn and McPhee-Shaw, 2013).

So far, the forcing mechanisms of CCCs have been mostly studied at the California Current upwelling system based on extensive sets of hydrographic and meteorological observations across and along the continental shelf. In particular, the coastal circulation in southern central California and in the Santa Barbara Channel (SBC) has been described in great detail (e.g., Harms and Winant, 1998; Winant et al., 2003, 1987) along with its relationship with wind conditions (Melton et al., 2009; Washburn and McPhee-Shaw, 2013). These studies have established that CCCs are mainly driven by poleward alongshore pressure gradients (APGs) that result from differences in sea level along the coast. The persistence of upwelling favourable winds may produce large scale alongshore sea surface slopes constituting the intermediate

mechanism by which the effects of remote winds are manifested in local currents (Largier et al., 1993). Numerical studies have further indicated that interactions between the upwelling circulation and alongshore variations in the coastline and shelf bathymetry promote the development of small scale poleward APGs in the lee (i.e., equatorward in California) of capes and promontories (Gan and Allen, 2002). CCCs are triggered when these (local or regional) APGs become unbalanced during wind relaxation events, i.e., during the weakening or even reversal of usually strong upwelling favourable winds (Huyer and Kosro, 1987; Melton et al., 2009).

At the Canary Current system, CCCs have been occasionally reported at north of the Iberian Peninsula, from the central western Portuguese coast up to the southern margin of the Gulf of Biscay (Ferreira Cordeiro et al., 2018; Sordo et al., 2001). However, these flows are mainly described along the northern margin of the Gulf of Cadiz (GoC), at the southwestern extremity of the Iberian Peninsula, where they constitute a prominent feature of the coastal circulation (Criado-Aldeanueva et al., 2009; García-Lafuente et al., 2006; Garel et al., 2016; Relvas and Barton, 2002; Sánchez et al., 2006; Teles-Machado et al., 2007). These studies have mainly focused on the role of (local and remote) atmospheric conditions and APGs in driving CCCs, without reaching a clear consensus in favour of one forcing.

The present study aims at obtaining new evidence about the dominant drivers of CCCs at the GoC. Kinematic parameters are defined to characterize the structure of alongshore flows at the very moment they change direction. Despite some intrinsic variability, the general patterns of these incipient flows are identified based on the analysis of an extensive (multi-year) dataset of current observations over the inner shelf. For comparison, the characteristic signatures of both poleward (i.e., broadly westward) and equatorward (i.e., broadly eastward) incipient flows are considered. Overall, the results provide new arguments that an APG is generally the main force responsible for CCC setup, contributing to improve the understanding of the inner shelf dynamics in coastal areas affected by upwelling events.

4.2 Background to the area

4.2.1 Geographic setting

The GoC is an embayment of Atlantic water located between the NW African coast and the SW tip of the Iberian Peninsula (Figures 4.1a). Its northern margin is limited at east by the Strait of Gibraltar and at west by the Cape São Vicente (CSV), where the Portuguese coastline changes direction from zonal to meridional (Figures 4.1a). Cape Santa Maria (CSM) separates a narrow western shelf (<30 km, referred to the 200 m isobath, hereafter) and a much wider eastern one (>40 km; Figures 4.1a). The discharge of the main rivers, located in the eastern region, is relatively low due to strong flow regulation by dams (Díez-Minguito et al., 2012; Garel and D'Alimonte, 2017). In particular, the largest river flowing into the GoC is the Guadalquivir, which mouth constitutes, along with Cadiz Bay saltmarshes, a region with extended intertidal areas.

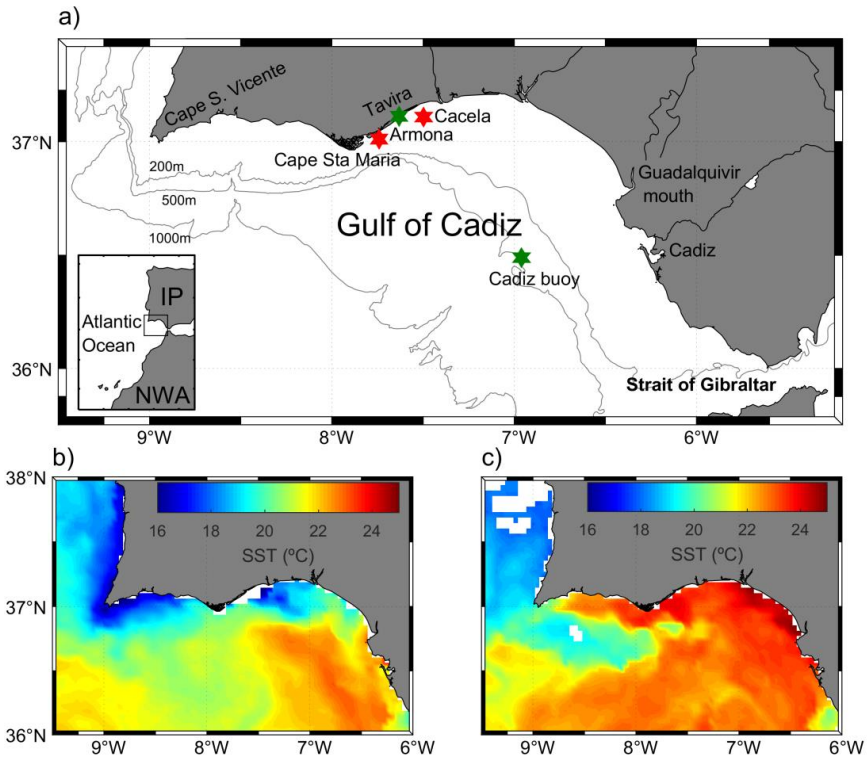

Figure 4.1 - (a) Northern region of the Gulf of Cadiz with indication of the ADCP moorings (red) and wind stations (green); SST (°C) signature of b) EFs on 01 July 2017 and c) CCCs on 30 August 2018. For general location, see inset in a) (IP: Iberian Peninsula; NWA: North West of Africa).

4.2.2 Wind patterns

The subtidal wind regime at the GoC is characterized by the alternation of westerly and easterly (so-called "Levanter") at a time-scale of 2-3 days during the entire year. The westerly may produce coastal upwelling along the South Portuguese coast, in particular in spring and summer (e.g., Figures 4.1b), although not as frequently and intensively as along the West coast (Relvas and Barton, 2002). The upwelling activity diminishes eastward of CSM with the widening of the shelf and vanishes at east of 7ºW, very broadly (Garel et al., 2016).

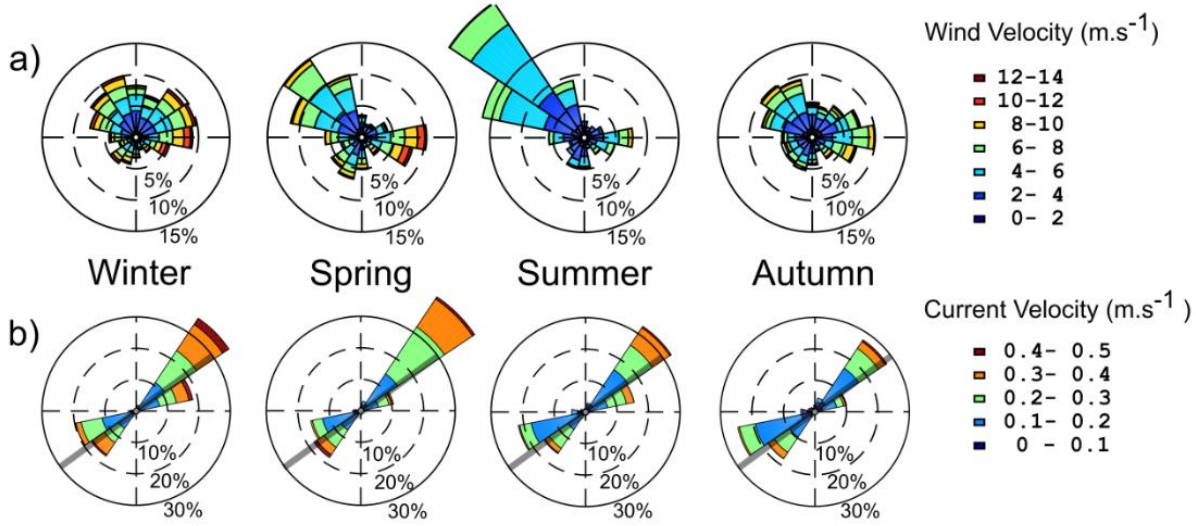

Figure 4.2 - Sub-diurnal seasonal (a) wind roses with meteorological convention (i.e., wind provenance) from Cadiz offshore buoy and (b) current roses (depth-averaged values at Armona station) with oceanographic convention (i.e., current direction) and coastline orientation (thick grey lines). The (wind and current) roses were constructed with hourly data spanning the ADCP deployment dates (01/03/2008-09/10/2018; Figure 4.3) that were low-passed filtered as described in Section 4.3.1. For locations, see Figure 4.1.

The seasonal wind regime in the GoC is characterized based on sub-diurnal records (2008-2018) from Cadiz buoy (Figures 4.2a). This offshore station is generally considered to be representative of wind conditions at the basin scale(Criado-Aldeanueva et al., 2009, 2006b; García-Lafuente et al., 2006; Garel et al., 2016 for location, see Figure 4.1a). Hereafter, winter corresponds to December-February; spring to March-May; summer to June-August; and, autumn to September-November. Summer is marked by weak wind conditions and a strong

dominance of NW winds. Such dominance is less marked at spring, when stronger events may occur in particular from the east. In autumn-winter, the wind direction is highly variable, with typically, more energetic events in winter.

4.2.3 Coastal circulation

The subtidal coastal circulation along the northern inner shelf of the GoC is mostly alongshore and bipolarized (e.g., Figures 4.2b). Typically, maximum (subtidal) alongshore depth-average velocities are about 0.4 $m.s^{-1}$ while cross-shore ones are one order of magnitude weaker (Garel et al., 2016).

Equatorward flows (EFs) along the southern coast of Portugal are generally considered to be related to the upwelling process, occurring either off the western coast under northerly winds or locally under westerly winds. Southward geostrophic flows associated to the upwelling off the west coast turn cyclonically around CSV due to bathymetric steering (conservation of the potential vorticity) and propagate eastward along the south coast (Figures 4.1b), where they eventually merged with locally upwelled water (Fiúza, 1983; Sánchez and Relvas, 2003; Relvas and Barton, 2002, 2005; García-Lafuente et al., 2006).

In opposition, CCCs flow poleward as a narrow band (15-20 km) along the southern coast and rarely propagate north of CSV (Relvas and Barton, 2002). Contrary to the cool EFs, CCCs typically raise the temperature along the coast in summer (e.g., Figures 4.1c), due to the advection of warm water from a pool located around the Guadalquivir mouth and Cadiz areas (García-Lafuente et al., 2006). In winter, the temperature contrast between equatorward and poleward flows is weak (Garel et al., 2016; Vargas et al., 2003). At Armona mooring (Figures 4.1a), CCCs are observed 40% of the time (mean duration of about 3 days) with no significant differences between winter and summer. This coastal current is suspected to alter water properties, in particular through nutrient depletion (Navarro and Ruiz, 2006; Rosa et al., 2019) and advection of pollutants (including trace metals) from the rivers (e.g., Guadalquivir see Figure 4.1a) and industrial areas (e.g., Cadiz) at East (González-ortegón et al., 2019; Laiz et al., 2020).

Based on SST satellite imagery, coastal wind and tidal gauge data, Relvas and Barton (2002) proposed that CCCs in southwestern Iberia are driven by a background APG that becomes

unbalanced during wind relaxation events, like at the SBC. Both regions correspond to a sharp change in coastline orientation from meridional to zonal at the southern extremity of a coastal upwelling system (Central California and Iberia). Yet, physiographic differences at both sites (e.g., the Channel Islands at the SBC; the Strait of Gibraltar and relatively large rivers at the GoC) may affect the mechanisms involved. For example, an APG may develop at the GoC due to buoyancy inputs (Bellanco and Sánchez-Leal, 2016), with potential contribution in summer of the pool of warm water (at East) through thermal expansion (García-Lafuente et al., 2006). Besides, water exchange across the Strait of Gibraltar - that has no counterpart in the Californian system - imposes an eastward drift of Atlantic waters into the Mediterranean basin (Peliz et al., 2007, 2009a; Sánchez-Leal et al., 2017), which may influence the dynamics of the coastal circulation. Furthermore, it is worth noting that the wind regime is quite distinct at the two locations: at the SBC, the relaxation of upwelling favourable wind often corresponds to calm wind conditions (e.g., Melton et al., 2009; Fewings et al., 2016) while it is generally associated to energetic Levanter at the GoC, hence making it difficult to discriminate the dominant driving process (Garel et al., 2016). Based on a numerical study, Teles-Machado et al. (2007) proposed that CCCs require the onset of Levanter wind to fully develop. Observations confirm that the Levanter influences the duration and intensity of CCC events, but also show that the latter may be triggered during calm wind conditions (Garel et al., 2016). Alternatively to local wind stress, the importance of wind conditions outside the Gulf (i.e., along the West Portuguese coast) for the development of CCCs has been pointed out (Sánchez et al., 2006). Coastal trapped waves forced by remote meteorological forcing may also produce poleward coastal flows in the studied region (Sánchez et al., 2006; Garel et al., 2016).

4.3 Data and methods

4.3.1 Data collection and processing

Hourly Acoustic Doppler Current Profiler (ADCP) observations at 23 m water depth were obtained through 16 deployments (from 1 to 6 months-long) between 2008 and 2018 at Armona station (37°00'38.88"N; 7°44'28.80"W; Figure 4.1a; Figure 4.3). Most of the data were collected with a Workhorse 600 kHz except for 2 deployments that employed a Sentinel V 500 kHz (both from TRDI). The time series (34,121 hourly records) is the same as the one analysed in Garel et al. (2016), completed with 9 additional deployments. The sampling effort was

stronger during the second semesters of each year, but all months were sampled. No monitoring was performed in 2009, 2011 and 2012.

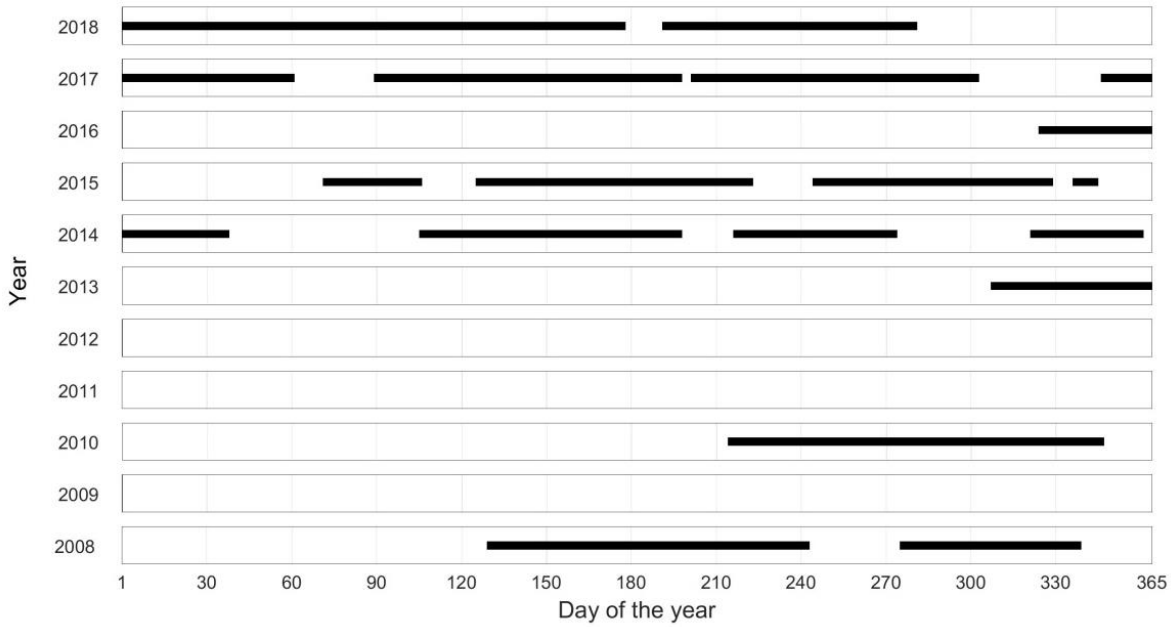

Figure 4.3 - ADCP deployments between 2008 and 2018 at Armona Station as indicated by the thick black line.

For each deployment, the instrument was bottom mounted on top of a concrete artificial reef at 1.4 m from the bed. Velocities were recorded within cells of 0.5 m (for 14 deployments) or 1 m (for the 2 deployments in 2008) in thickness along the water column. The expected standard deviation (accuracy, σ) of the horizontal velocity from the ADCP setup was generally less than 0.02 $m.s^{-1}$ (except in Aug.-Oct. 2014, <0.03 $m.s^{-1}$) with a mean value of 0.013 $m.s^{-1}$.

Data quality was ensured by independent validation of each ensemble following the procedure described in Garel et al. (2016). Validated cells were generally from 3 m off the bed to 80% of the total water depth. The semi-diurnal tidal and other higher frequencies were removed from the time series using a Butterworth low-pass filter with a 40-h cut-off period. The filtered data were then rotated in cross-shore and alongshore components using the angle of the coastline orientation in front of the deployment site (i.e., 36° counted counter-clockwise from east, hereafter; see the thick grey lines in Figure 4.2b). The angle of maximum variance of the velocity records generally corresponds to the coastline orientation, with a slight variation (from 28° to 38°) between deployments. It was verified that the choice of the rotation angle (e.g.,

coastline orientation or angles of maximum variance) does not affect the results of the present study. Only the alongshore current component is considered hereafter, with positive values for EFs and negative values for CCCs. Three flow layers were selected for analysis: the near-surface flow (u_{surf}), defined as the mean velocity of the two uppermost cells; the depth-averaged flow (u), computed as the mean velocity of all cells; and the near-bed flow (u_{bed}), defined as the mean of the two cells closest to the bottom. For analyses of the vertical profiles, the velocities along the water column were normalized to the water depth using an interval of 0.025 between 0.075 and 0.75 (where 0 is the bed and 1 is the water surface). The upper limit corresponds to the maximum normalized depth with valid cells (i.e., non-contaminated by the surface boundary) which was common to all deployments.

4.3.2 Characterisation of the turn of the flow

By convention, a change in the flow direction from equatorward to poleward, corresponding to a switch of the alongshore flow component from negative to positive values, is termed "EP" in the following; likewise, a change from poleward to equatorward (i.e., from positive to negative alongshore flow component) is termed "PE". EPs therefore correspond to the setup of CCCs and PEs to the setup of EFs. The time of the turn of the flow was defined based on the zero crossing of the depth-averaged velocity. A total of 160 events were selected, for which both the near-bed and near-surface velocities changed direction (i.e., crossed zero) 48 h before or after the depth-averaged velocity. From those, only events with subsequent depth-averaged velocity >0.05 m.s^{-1} were retained, corresponding to a total of 138 EPs and 135 PEs.

The mean vertical structure of incipient flows (i.e., when the depth-averaged velocity crossed zero) was computed from the depth normalized velocities. In addition, a principal component analysis (PCA) was performed using the correlation matrix with the mean removed as in Stacey et al. (2001) and Garel et al. (2016) to identify the main source of variability of the velocity profiles when the flow changes direction. Furthermore, the following parameters were defined to characterize EP and PE events: the Flow Acceleration, the Peak Velocity, the Event Duration, the Peak Delay, the Layers Time Lag and the Vertical Shear. These parameters are defined below and exemplified in Figure 4.4 (see also Figure S4.1 in supplementary material).

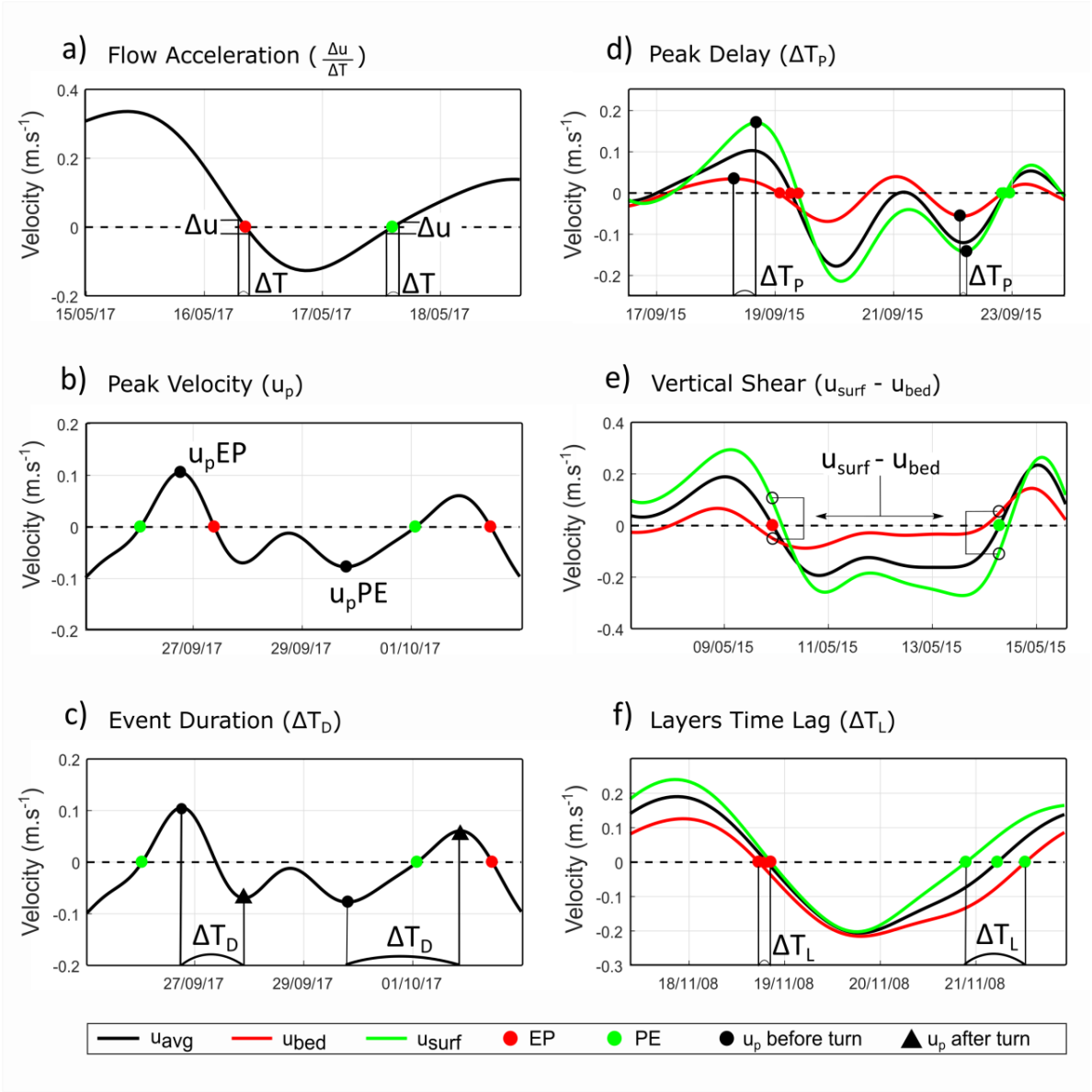

Figure 4.4 - Representation of the parameters used to describe the turn of the flow (based on observed events): a) Flow Acceleration, b) Peak Velocity, c) Event Duration, d) Peak Delay, e) Vertical Shear, and f) Layers Time Lag.

The Flow Acceleration ($\Delta u/\Delta T$, in $m.s^{-2}$; Figure 4.4a) was computed considering the difference in the velocity magnitude (Δu) one hour before and after it crossed zero (i.e., ΔT = 2 h); thus, this parameter represents how fast a flow layer changes direction. The Peak Velocity (u_p, in $m.s^{-1}$; Figure 4.4b) corresponds to the first zero value of the velocity derivative before a zero-crossing; this parameter characterizes the velocity of the flow when it starts to decelerate at the beginning of a turning event. The acronyms u_pEP and u_pPE refer to the Peak Velocity before EP and PE events, respectively. An event is considered to end when the flow reaches a

maximum in the opposed direction; hence, the Event Duration (ΔT_D in hours; Figure 4.4c) corresponds to the time interval between the peaks of the (depth-averaged) velocity before and after the zero-crossing. The Peak Delay (ΔT_P in hours; Figure 4.4d) is the time difference between the Peak Velocity (u_p) of the surface and bed layers; this parameter indicates which layer starts to decelerate first, with a positive (negative) value when it is the bed (surface) layer. The Peak Delay is considered null when the absolute difference is <2 h. The Vertical Shear (u_{surf}-$u_{bed,}$ in $m.s^{-1}$; Figure 4.4e) represents the difference between the near-surface and bed velocities when the depth-averaged velocity crosses zero; this parameter indicates which layer changes direction first. The flow was considered as unidirectional (i.e., simultaneous change of direction along the water column) when the Vertical Shear was less than the total velocity accuracy (σ_{total}), derived from the velocity accuracy as:

$$\sigma^2{}_{total} = 2\sigma^2 \qquad (1)$$

Finally, the Layers Time Lag (ΔT_L, in hours; Figure 4.4f) corresponds to the delay between the zero crossing of u_{surf} and u_{bed} and thus represents the time required for the entire water column to change direction; the Layers Time Lag was considered as null when the absolute difference was <2 h. Linear relationships between pairs of parameters were evaluated using the Spearman's correlation coefficient (denoted R) at a 95% confidence interval.

Since the alongshore flow is a vector component (EFs are positive, CCCs are negative), the Flow Acceleration, Peak Velocity and Vertical Shear have opposite signs for EPs and PEs. For straightforward comparisons, these parameters were multiplied by -1 in the case of PEs. Then, independently of the direction of the current reversal, the Flow Acceleration and Peak velocities have always positive values, and a positive Vertical Shear indicates that the bed layer changed direction first.

4.4 Analysis of flow reversals

4.4.1 Mean profiles and variability.

The mean profile of EPs consists of a 2-layer flow, positive (i.e., equatorward) near the surface (Figure 4.5a). By contrast, the mean profile of PEs is close to zero along the entire water column

(Figure 4.5b). For both cases, the standard deviation displays an hourglass envelope with minimum values around mid-water and maximum values near the surface and bed.

The dominant PCA component (PC1) of reversing flow profiles contains 72% and 70% of the data variability, respectively. The Eigenvectors that represent the amplitude of variation of PC1 along the water column represent a 2-layer flow for both cases (Figure 4.5c). This indicates that the vertically sheared mean profile of EPs (Figure 4.5a) results from the predominance of a 2-layer flow oriented poleward near the bed. For PEs, the number of 2-layer flows with opposite direction is similar, producing a mean vertical profile around zero (Figure 4.5b).

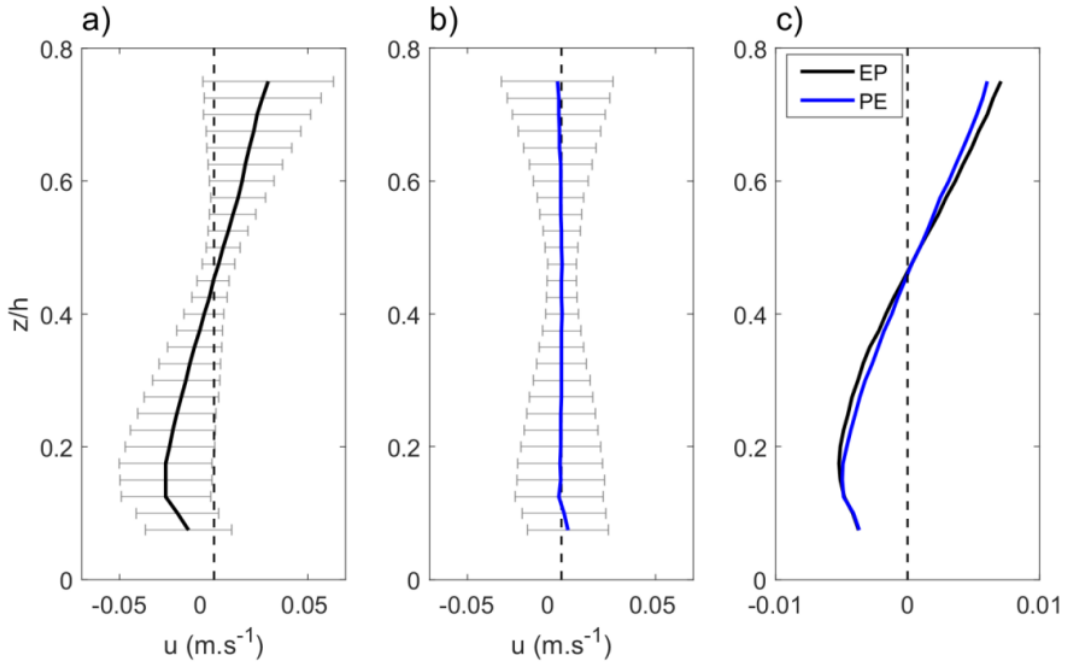

Figure 4.5 - Mean vertical velocity profile (m.s^{-1}) and standard deviation (error bars) along the normalized depth (z/h) for (a) EPs and (b) PEs; c) PC1 Eigenvectors of EPs (black) and PEs (blue).

The above results show that CCCs develop predominantly near the bed first, while the setup of EFs through the bed and surface layers is approximately balanced. Snapshots of these incipient flows are displayed in Figure 4.4 (see also Figure S4.13 in supplementary material). Similar patterns are observed when the velocity profiles are sorted by seasons (Figure 4.6). In this case, PC1 (2-layer flow) represents >63% of the data variability (red in Figure 4.6). CCCs clearly initiate more often near the bed in spring-summer than in autumn-winter. In comparison, the

mean profiles of PEs are weakly sheared for all seasons (as EFs develop more equally through both the surface and bed layers), except in winter. For the latter season, incipient EFs appear predominantly near the surface first (Figure 4.6e).

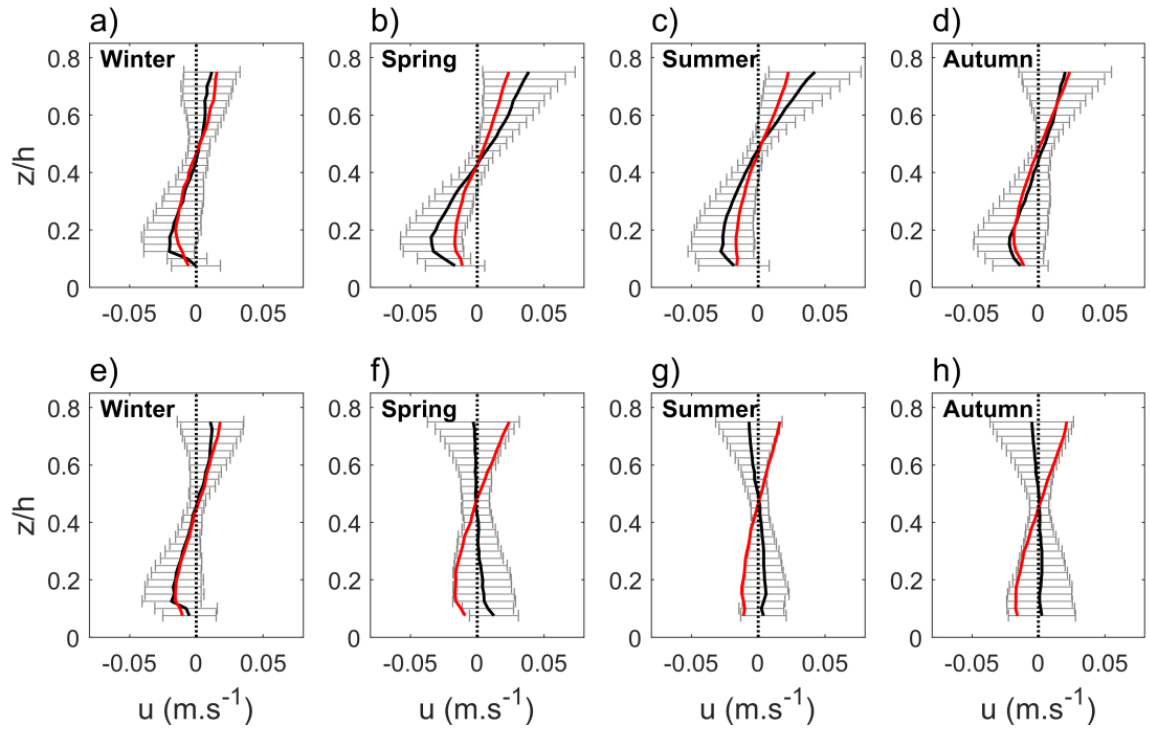

Figure 4.6 - Mean seasonal vertical velocity profiles (m.s^{-1}, black), standard deviation (error bars) and PC1 Eigenvectors (red, divided by 0.3 for representation) along the normalized depth (z/h) for EPs (upper row, a-d) and PEs (lower row, e-h).

4.4.2 Parametric characterization of incipient flows

4.4.2.1 Vertical Shear

The Vertical Shear (see Figure 4.4e) ranges between -0.05 m.s^{-1} and 0.17 m.s^{-1} for EPs and ±0.15 m.s^{-1} for PEs (Figure 4.7a). The positively skewed distribution of EPs confirms that CCCs develop predominantly through the bed layer (Figure 4.7a, pink); likewise, the (more) symmetric distribution of PEs reflects that EFs tend to initiate evenly near the surface and bed (Figure 4.7a, grey). These distribution patterns remain unchanged when the velocity accuracy is accounted for (Table 1). In particular, 66% of CCCs develop near the bed first, against 39% for EFs; likewise, CCCs rarely initiate through the surface layer (10%) compared to EFs (37%).

For EPs, positive Vertical Shears predominate remarkably in spring-summer in terms of both frequency (about 80%; Table 1) and mean magnitude (Figure 4.7b). By contrast, the setup of CCCs in winter is characterized by a weak positive shear reflecting the predominance of unidirectional flow profiles during this season (57%; Table 1). Autumn seems to be a transitional season (e.g., 57% of positive Vertical Shear), but also presents the largest occurrence of CCCs setup near the surface (17%; Table 1).

For PEs, the seasonal variability is relatively weak (Figure 4.7c). Still, winter stands out with a negative mean value, as EFs develop most often near the surface first (Figure 4.7c; Table 1). As for EPs, the percentage of EFs initiating near the bed in autumn (39%) is intermediate between spring/summer and winter (Table 1). Overall, EFs develop more often near the surface layer than CCCs, whatever season is considered.

4.4.2.2 Peak Delay

While the Vertical Shear and Layers Time Lag describe the flow at the moment it changes direction, the Peak Delay (see Figure 4.4d) gives insights about the flow structure when it starts to decelerate, at the beginning of the turning event. In general, the multi-year and seasonal patterns of the Peak Delay are fairly similar to the ones of the Vertical Shear and Layers Time Lag. Mostly, the flow slows down near the bed first, especially for EPs (53%, while 40% for PEs; Figure 4.7g). This trend is well-marked in spring and summer, while winter is characterized by a smaller variability and more events decelerating near the surface first (Figure 4.7h-i).

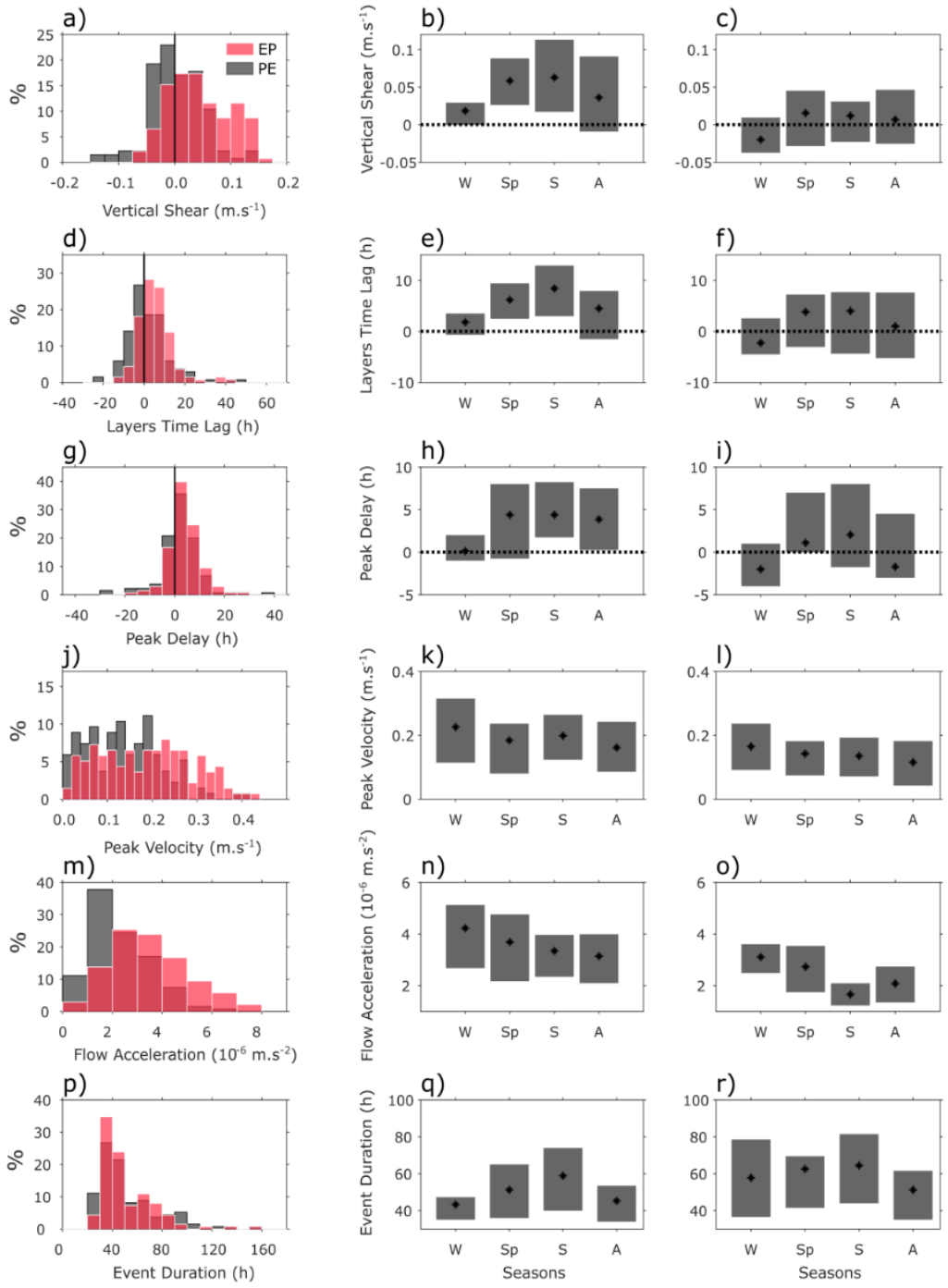

Figure 4.7 - Parametric characterization of EPs and PEs: a-c) Vertical Shear ($m.s^{-1}$); d-f) Layers Time Lag (h); g-i) Peak Delay (h); j-l) Peak Velocity ($m.s^{-1}$); m-o) Flow Acceleration (10^{-6} $m.s^{-2}$); and, p-r) Event Duration (h). The left column represents the distribution of all data, with EPs in pink, PEs in grey and the superimposition of both in red. The middle and right columns represent the interquartile range by season for EPs and PEs, respectively (W: winter; Sp: spring; S: summer; A: Autumn) and asterisks represent the season mean.

Table 4.1 - Percentage of incipient flows developing through the bed layer (positive), through the surface layer (negative) and at once through the whole water column (i.e., unidirectional flows, as defined in section 4.3.2) during EPs (i.e., CCCs setup) and PEs (i.e., EFs setup) at Armona station.

	% EPs (CCCs setup)			% PEs (EFs setup)		
	Positive (bed 1st)	Negative (surface 1st)	Unidirectional	Positive (bed 1st)	Negative (surface 1st)	Unidirectional
All data	66	10	24	39	37	24
Winter	39	4	57	15	54	31
Spring	80	3	16	50	33	17
Summer	81	10	8	49	34	17
Autumn	57	17	26	39	32	30

4.4.2.3 Layers Time Lag

The Layers Time Lag (see Figure 4.4f) features patterns similar to the Vertical Shear at both the multi-year average and seasonal timescales (Figure 4.7d-f). For instance, considering all the data, EPs present a significantly larger occurrence of positive lags than PEs (67% and 42%, respectively) as CCCs develop more often than EFs through the bed layer. By seasons, the Layer Time Lag also reflects the large predominance of CCCs setup near the bed in spring-summer compared to winter; likewise, the more balanced pattern for PEs, except in winter. In fact, the Layer Time Lag and Vertical Shear are significantly correlated for both EPs and PEs ($R>0.88$, $p<0.05$), indicating that long (short) turnarounds of the entire water column are generally associated to strongly (weakly) sheared flows. This is somehow expected as both parameters compare the surface and bed layers at the time of the (depth-averaged) zero-crossing.

The positive Layers Time Lag is often remarkably large, frequently exceeding 10 h (22% for EPs and 15% for PEs), compared to the negative lag (Figure 4.7d). This pattern indicates that the entire water column tends to switch direction significantly faster when it starts near the surface (2 h for EPs and 5 h for PEs, in average) than near the bed (9 h for EPs and 11 h for PEs, in average).

Similar to the Layer Time Lag, the positive Peak Delay is relatively large, being for example >10 h for about 12% of the flow reversing events. Furthermore, the (surface or bed) layer that decelerates first also changes direction first in the majority (66%) of cases.

4.4.2.4 Peak Velocity

The Peak Velocity (see Figure 4.4b) shows no clear seasonal patterns (Figure 4.7k-l). However, it indicates that the velocity is generally larger at the start of EPs than PEs (Figure 4.7j). For example, 17% of u_PEP is >0.3 m.s^{-1}, while only 4% of u_PPE. This distinct pattern is due to the fact that EFs and CCCs tend to be strongest towards the end and start of their occurrence, respectively. This is well-evidenced by histograms of the time of maximum velocity for alongshore flows lasting more than 2 days (Figure 4.8, where the time is normalized to the flow duration: 0 is the start and 1 is the end of the flows). For CCCs, the maximum velocity occurs mainly during the first half of their development; for EFs, it rather occurs towards the end of the flow (i.e., shortly before EP events).

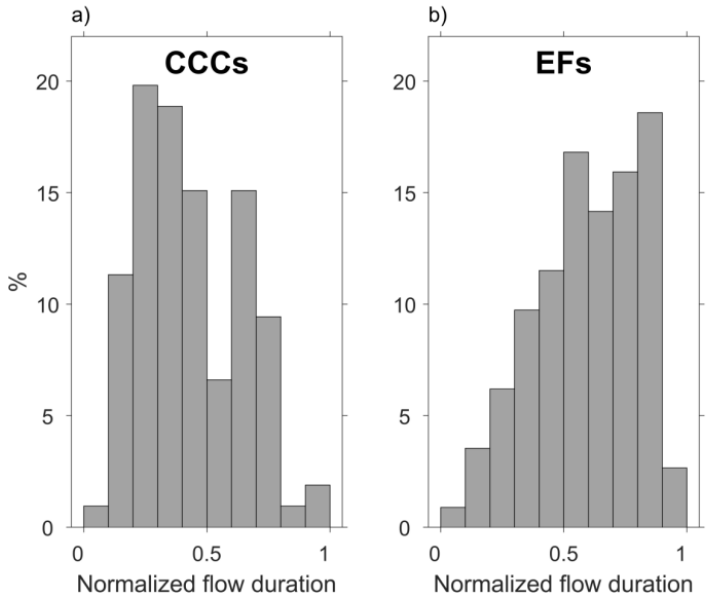

Figure 4.8. Histogram of the time of maximum velocity during CCCs (a) and EFs (b) lasting more than 2 days. The duration of each flow period is normalized between 0 (start) and 1 (end).

4.4.2.5 Flow Acceleration

The Flow Acceleration (see Figure 4.4a) tends to be larger for EPs than PEs (Figure 4.7m). For example, the mean acceleration of EPs is 3.5×10^{-6} $m.s^{-2}$, representing a change of velocity of 0.025 $m.s^{-1}$ in 2 h; For PEs, it is 2.3×10^{-6} $m.s^{-2}$, representing a change of velocity of 0.017 $m.s^{-1}$ in 2 h. Similarly, the Flow Acceleration tends to be larger for EPs than PEs for each season (Figure 4.7n-o). Thus, EPs are in general more dynamic than PEs, in the sense that velocity changes occur faster. This characteristic is explained by the previously observed tendency for maximum EF and CCC velocities to occur shortly before and after EPs, respectively (Figure 4.8).

4.4.2.6 Event Duration

The Event Duration (see Figure 4.4c) is in average 58 h for PEs and 50 h for EPs (Figure 4.7p). No clear seasonal pattern is noted for PEs (Figure 4.7r); for EPs, the seasonal variability is somewhat similar to the one of the Vertical Shear, Layers Time Lag and Peak Delay (compare Figure 4.7q with Figures 4.7b, 4.7e and 4.7h). In particular, the Event Duration of EPs tend to be significantly shorter in autumn/winter than in spring/summer (e.g., from 43 h in winter to 58 h in summer, in average).

4.5 Discussion

4.5.1 Main patterns of incipient flows

The above results indicate a large variability of the structure of incipient flows. Such variability reflects the intrinsic complexity of the flow dynamics, in particular when dealing with (weak) reversing currents. In this case, small variations of the forcing agents may affect significantly their balance and thus the resulting flow structure. Yet, the present statistical approach based on an extensive dataset shows that incipient flows feature distinct general patterns whether they turn from poleward to equatorward or the opposite.

Overall, PEs are relatively smooth events, i.e. characterized by relatively weak parameters, such as the Vertical Shear and Layers Time Lag, occurring equally near the bed and surface (Figure 4.7). By contrast, EPs are more dynamic, associated to stronger parameters; they develop

predominantly near the bed first with a strong vertical shear, and an extensive time (often >10 h) is generally required for the entire water column to change direction. Such distinct structures were also reported when the flow starts to decelerate. Thus, the observed patterns correspond to temporally consistent structure of incipient flows rather than short “noisy” oscillations. The contrasting patterns of EPs and PEs suggest that these events are driven by distinct factors, in particular during the upwelling season (in spring and summer), when these differences are contrasted the most.

The spatial consistency of the alongshore incipient flow structure at Armona is examined using data from a twin ADCP station (Cacela) located 24 km eastward at the same water depth (37° 6'26.82"N; 7°29'47.64"W; Figure 1a). The analysis of this dataset (5 deployments of 3 to 6 months-long between 2015 and 2017) shows similar trends than at Armona. Overall, 67% of EPs and 45% of PEs at Cacela started through the bed layer, with a large discrepancy between summer (90%) and winter (50%). The same layer reversed first at both stations for 64% of the coinciding events (42 EPs and 44 PEs). This indicates that the previously described general characteristics of incipient flows maintain along the eastern region adjacent to CSM. It is noteworthy that the development of CCCs through the bottom layer was also reported based on observations at the central California upwelling system (see Figure 2 in Gan and Allen, 2002).

In the following, the main drivers responsible for the opposite vertical structures of incipient flows (i.e., initiating near the surface or near the bed) are discussed. The focus is on the drivers of CCCs, which is the main issue addressed in this paper; the results for EFs are used for comparisons to support the argumentation.

4.5.2 Incipient near-surface flows

Overall, the analysed kinematic parameters are markedly different in winter compared to the other seasons (Figure 4.7). In particular, the near-surface layer of incipient flows is clearly promoted in winter (when PEs develop dominantly at the surface and EPs have a relatively weak Vertical Shear; Figures 4.6, 4.7b and 4.7c). Typically, winter is characterized by the frequent occurrence of gales in both the eastward and westward directions (Figure 4.2a), and with generally short (<one week) transitory periods with weak wind (Garel et al., 2016). The wind regime is overall milder during the other seasons. As the wind blows across a free water

surface, the induced frictional drag accelerates the near-surface layer first (Csanady, 1984; Thorpe, 2004; Kudryavtsev et al., 2008). Hence, the above observations strongly suggest that incipient flows developing at the surface are generally the manifestation of a dominant local wind forcing.

Yet, no direct relation could be established between the incipient flow parameters and wind stress τ_w (computed according to Large and Pond, 1981). For both EP and PE, a large majority (70%) of incipient flows develop with favourable wind stress, independently of which layer turns first (Figure 4.9). Only for strong favourable wind (>0.025 Pa, equivalent to 4 $m.s^{-1}$), PEs start dominantly near the surface (Figure 4.9b). By contrast EPs associated to such strong favourable wind mainly develop near the bed (Figure 4.9a). Likewise, CCCs rarely develop through the surface layer at spring, despite the large occurrence of strong Levanters during this season (Figure 4.2a); as a matter of fact, CCCs develop slightly more often at the surface in summer, when Levanters are infrequent (Table 1). Clearly, wind events, including strong ones, have a lesser effect on incipient surface flows of CCCs than of EFs. The low occurrence of surface incipient flows and their poor relations with wind indicate that CCCs are generally not driven by local wind.

The above discussion assumes that Cadiz offshore buoy is representative of the local wind condition, in particular when the flow changes direction, despite being at 90 km away. To verify this correspondence, the wind from Tavira, the land station closest to Armona mooring, was considered (for location, see Figure 4.1). Hourly time series at Tavira concomitant with our dataset (available in 2008 and 2013/2014, only) were low-passed filtered similar to the Cadiz buoy wind (see Section 4.3.1). The correlations between the two wind sources are very good ($R>0.72$, $p<0.05$), especially for the eastern component ($R=0.91$; see also the comparisons in Garel et al., 2016). However, the wind at Tavira is weaker than offshore, indicating that the land is sheltering the mooring site, in particular from the eastern component (e.g., Figure S4.14 of supplementary material). To assess the effect of such wind differences on the present results, Figure 4.9 was reproduced with the (shorter) concurrent time-series from both wind sources (Figure S4.15 of supplementary material). The results confirm that the alongshore wind component (i.e., with similar alongshore orientation than at the ADCP station), at the moment the flow changes direction, is weaker at Tavira than at Cadiz buoy, but the relations with incipient flows are similar for both stations. These results are also similar to those obtained with

the full time-series at the offshore buoy (compare Figure S4.15 with Figure 4.9). In addition, despite differences in intensity, the mean alongshore wind velocity pattern during the few days preceding the flow reversal is highly similar at both stations (Figure S4.16 of supplementary material). In particular, the mean wind is favourable when the flow turns, as previously observed; it is notably weak during EPs at the land station. Overall, these observations support that PEs are more wind driven than EPs. The sheltering of the wind near the coast may partly explain why the vertical structure of incipient CCCs is not affected by strong wind at the offshore buoy.

The wind effect signature on the surface flow is also probably undermined by the complicated nature of the coastal ocean response to time-varying wind-stress (e.g., Dickey and Simpson, 1983). Furthermore, due to inherent equipment limitations, the ADCP near-surface velocity is at some distance below the surface (about 20% of the water depth), excluding from the analysis the uppermost water column where wind stress is the strongest. There are also other competing factors (remotely produced fully-develop flows, stratification, lateral instability, buoyancy inputs, etc.) that could contribute to mask the wind signature. However, the key finding of the proposed analysis is that CCCs rarely develop near the surface, even under strong favourable wind, contrary to EFs. Another force competing with the surface wind stress drives the setup of CCCs through the bed layer. Wind is generally not the main driver of CCCs, in particular in spring and summer when about 80% of CCCs develop through the bed layer.

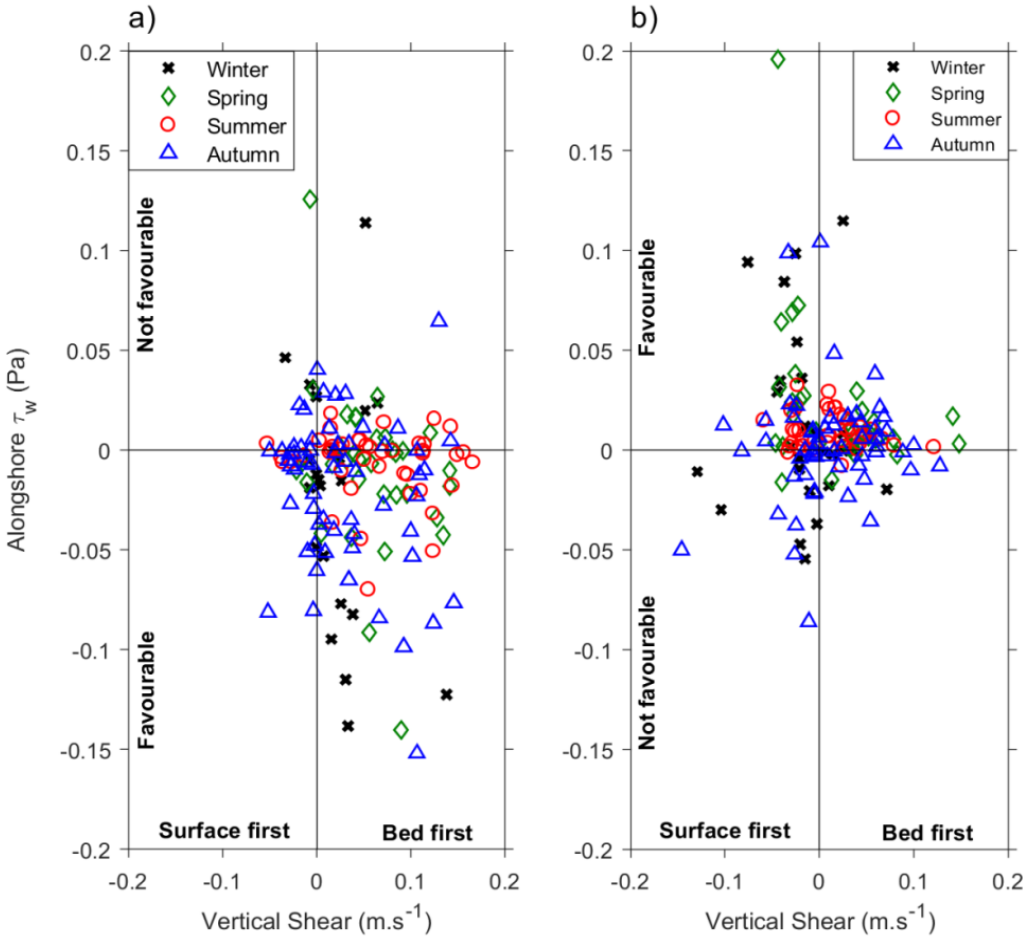

Figure 4.9 - Vertical shear (>0 for an event developing through the bed, m.s^{-1}) against alongshore wind component from Cadiz offshore buoys (>0 north-eastward, m.s^{-1}) at the time of zero crossing for EPs (a) and PEs (b).

4.5.3 Incipient near-bed flows

The available literature about flow developing through the bed layer indicates that this feature is essentially related to pressure variations (Oertel, 2004; Dronkers, 2005). For instance, within regions of the Irish Sea where the flow is close to unidirectional, tidally-driven changes in current direction occur 2 h to 4 h earlier at the bed than at the surface, depending of mixing conditions (Simpson et al., 1996). The faster adaptation of near-bed flows to fluctuations in the pressure gradient is related to the depth dependence of the turbulence length scale. The turbulent eddies generated by shear stress on the bottom get larger as they propagate upward. The dissipation rate of the turbulent kinetic energy is therefore more efficient near its source than

above (Rippeth et al., 2003) and maximum dissipation occurs later at greater heights off the seabed (Simpson et al., 1996; Burchard et al., 2002). Consequently, the surface velocity keeps longer its momentum than the bed velocity.

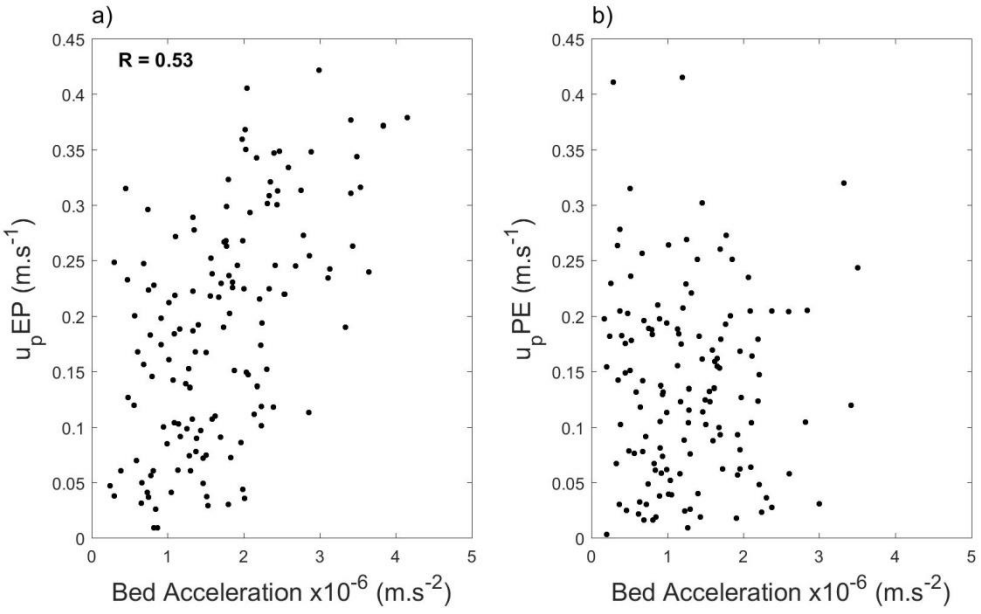

Figure 4.10 - Flow Acceleration (10^{-6} m.s^{-2}) of the near-bed layer Vs Peak Velocity (u_p, m.s^{-1}) for (a) EPs and (b) PEs.

Combining tidal gauge data with dynamic height estimates, Relvas and Barton (2002) provided strong arguments that equatorward flows are associated to the development of an APG (positive eastward) all year round along the South Portuguese coast. Besides, García-Lafuente et al. (2006) predicted that an APG would favour the development of CCCs through the bed layers first. They claimed that the eastward wind drag opposes the pressure gradient force, thus delaying the setup of a westward counter flow through the surface layer; at the same time, the water further below is able to move down this pressure gradient as the wind stress effect reduces with water depth. This process may explain about 30% of the present observations, where CCCs develop mainly near the bed with opposed wind direction (Figure 4.9). However, for the 70% left, EPs develop under favourable wind conditions. In this case, it is probable that the flow turns predominantly near the bed due to the larger momentum of the upper layers. The remarkably large time lag between bed and surface layer is attributed to the small subtidal

pressure variations along the coast, corresponding to water level amplitudes of the order of 5 cm per 100 km (Relvas and Barton, 2002).

It was previously noted (Section 4.2.4) that the maximum velocity occurs at a different time for EFs and CCCs (Figure 4.8). This pattern reveals a distinct intrinsic nature of both alongshore flows. The increase of EF velocity through time (Figure 4.8b) is associated with a relatively constant mean alongshore wind that weakens towards the end of the flow development (see Figure S4.17 in supplementary material). The geostrophic adjustment is difficult to assume over the inner shelf, where the water depth is far less than the Ekman layer and the wind stress forcing overlaps with the bottom friction. Nevertheless, the EF velocity trend is consistent with the development of an upwelling (quasi-geostrophic) circulation under persistent favourable wind. Contrarily to EFs, CCCs rapidly reach a maximum velocity after their setup (Figure 4.8a). This pattern suggests that the main driver of CCCs is strongest when the flow starts to develop; in agreement, a balanced APG is expected to have the greatest action on the flow when it becomes unbalanced during wind relaxation (i.e., when the water level slope is the largest). Insights about APG dynamics can be inferred from the significant correlation ($R=0.53$, $p<0.05$) between the Peak Velocity and Flow Acceleration near the bed during EP events (Figure 4.10a). Remarkably, EFs with large velocity tend to be associated to large acceleration of incipient CCCs in the opposed direction. By contrast, no significant correlation was obtained between these parameters for PEs (Figure 4.10b). Assuming that EFs are involved in the development of APGs (as proposed by Relvas and Barton, 2002), stronger EFs should be associated to larger APGs that oppose them. In turn, a steeper surface slope is expected to produce larger westward flow acceleration during wind relaxation (when the APG becomes unbalanced). This effect is clearer near the bed layer, which is less affected by the wind stress. This singular feature of EP is hardly explained by other potential driving factors of CCCs (such as lateral buoyancy inputs, wind or mid-shelf processes) but supports that EFs and the development of APGs are dynamically related.

4.5.4 Momentum analysis

In order to get more insights about the setup of CCCs, solutions of the depth-averaged momentum equation in the alongshore (x) direction are examined. The coordinate system is the same as for currents (positive in the equatorward direction), with u the depth-averaged velocity

measured at Armona station. Typically, assuming barotropic conditions and constant mean depth H, the equation can be expressed as (Sánchez et al., 2006; Li, 2011; Gan and Allen, 2002; Lentz and Winant, 1986)

$$\frac{\partial u}{\partial t} + NLX - fv = \frac{\tau_w - \tau_b}{\rho_{0H}} + \frac{Hg\partial\rho}{\rho_0 \partial x} + F - g\frac{\partial \eta}{\partial x} \qquad (2)$$

where t is the time, τ_b is the bottom stress, ρ is the water density (with subscript 0 for mean value), f is the Coriolis parameter, v is the cross-shore velocity, g is the gravitational acceleration, F is the divergence of the horizontal Reynold stress in the x direction and η is the sea level. In Equation 2, left hand side terms represent respectively the local acceleration ($\frac{\partial u}{\partial t}$), the nonlinear advection (*NLX*) and the Coriolis terms, which are balanced by the surface and bottom stress, alongshore density gradient, Reynold stress and free surface slope terms on the right hand side. On a first approach, the relation between the surface and bottom stresses and the local acceleration is examined, lumping the other terms in a residual term (*Res*):

$$\frac{\partial u}{\partial t} = \frac{\tau_w}{\rho_0 H} - \frac{\tau_b}{\rho_0 H} + Res \qquad (3)$$

The bottom stress is calculated as $\tau_b = \rho_0 C_d u$ with a bottom drag coefficient C_d = 1.25x10^{-4} , following a similar analytical approach at the study site (Sánchez et al., 2006).

The general patterns of the terms in Eq. (3), representative of most flow reversals, are exemplified in spring 2014 and winter 2016 (Figure 4.11) for both EP (red boxes on the 22/05/2014, 17/12/2016 and 20/12/2016) and PE (blue boxes on the 18/05/2014 and 18/12/2016). The local acceleration is generally balanced by the residual term, except during periods of strong wind, such as on the 21/05/2014 (Figure 4.11a-c) and 17-18/12/2016 (Figure 4.11d-e). The residual reaches a maximum during flow reversal since this is when the acceleration is strongest. In general, the contribution of residual terms tends to be stronger during EP than PE, despite similarly weak wind intensity (e.g., 22/05/2014 and 18/05/2014 in Figure 4.11a-c). Considering the whole dataset, 52% of EPs occur with a residual acceleration >2.5×10^{-6} m.s^{-2} while 22% for PEs. A peak in residual is also observed during EP events with significant wind stress (and reversing near the bed first) such on the 17/12/2016 (Figure 4.11d-e). Even in such case, the local acceleration is not produced by the wind stress alone and a residual must exist to balance the momentum equation.

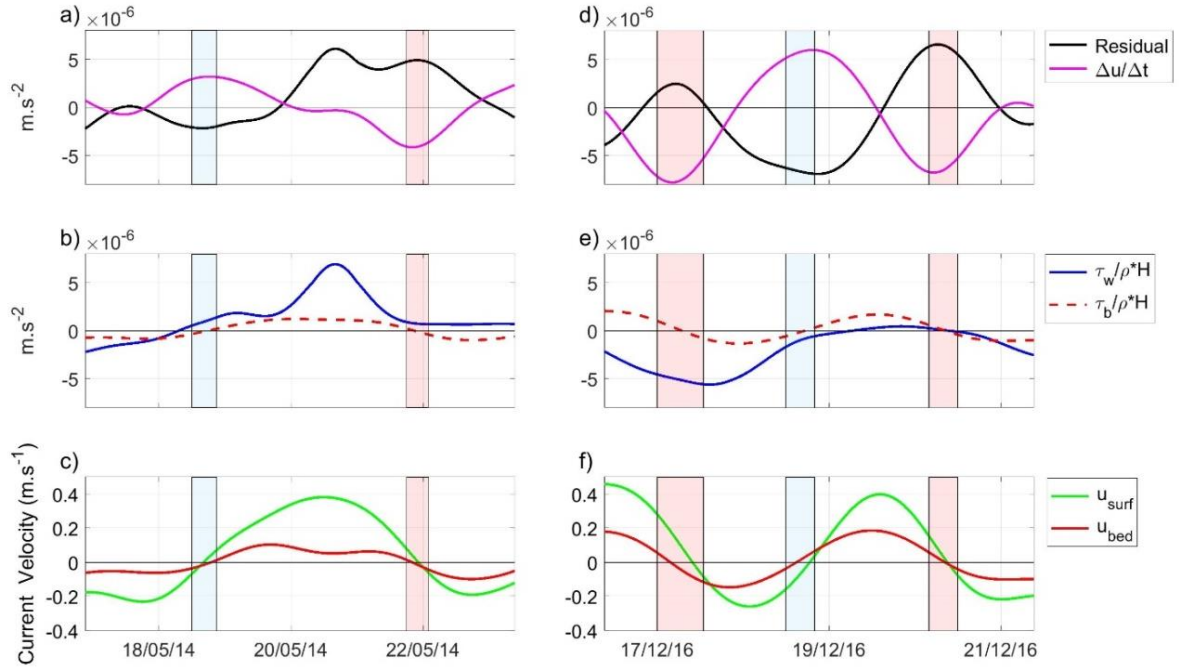

Figure 4.11. Terms of the momentum equation formulated as Eq. (3) in 2014 (left column) and 2016 (right column), with (a, d): local acceleration (pink) and residual (black) terms; and, (b, e): wind (blue) and bottom (dashed red) stress terms. (c, f): near-bed (red) and near-surface (green) alongshore velocities). EP and PE events are indicated with red and blue boxes, respectively.

The above observations confirm that the wind is not the main driver of current reversals, especially during EP events. Through scaling of the momentum equation with ADCP data collected nearby Armona station, Sánchez et al. (2006) concluded that the advective, Coriolis, Reynold stress and alongshore density gradient terms are secondary compared to local acceleration and stress, and can be neglected. Coriolis can reasonably be assumed to be zero, at least for EP due to the proximity of the coast impeding significant northward cross-shore flow. Advection is also expected to be small, as the alongshore flow remains in similar water depth and do not show strong acceleration along the coast. This is supported by comparison of Cacela and Armona concomitant deployments, where advection is 2-3 orders magnitude lower than the terms presented in Eq. (3). Based on climatological analysis of a local historic hydrographic database, Sánchez et al. (2006) estimated that the alongshore density gradient between CSM and the Guadalquivir is about 0.4 kg.m^{-3}. Such gradient would produce an acceleration which is 1 order of magnitude lower than the mean local acceleration observed during EP (3.5×10^{-6} m.s^{-2}). Yet, alongshore temperature variations of 5°C over 100 km (like on the 01/07/2017, Figure 4.1b) may produce a theoretical density-driven acceleration of the same order as the

local acceleration (considering the salinity field as homogeneous); likewise, for alongshore salinity variations of about 2 (and constant temperature). On the other hand, significant alongshore temperature variations are only observed in summer, and the river discharge is generally weak (due to strong flow regulation and to the regional rain regime) except for seldom high discharge events occurring episodically in winter and spring (Díez-Minguito et al., 2012; Garel and D'Alimonte, 2017). These seasonal patterns contrast with the observed development of CCCs near the bed all year round. Furthermore, by analogy with the estuarine circulation, the density gradient produced by such temperature and salinity variations is negative eastward and should promote equatorward (poleward) near-bed (surface) flows (Savenije, 2012; Geyer and MacCready, 2014), opposite to the main characteristics of EPs. Thus, it is reasonable to assume that alongshore density gradient is generally too weak to play a major role in the setup of CCCs, except for (probably infrequent) periods of strong gradient development.

From the above discussion, the main term driving EP events is assumed to be the alongshore pressure due to sea level variations. Such simplification of the momentum equation suggests that the circulation is mainly driven by linear dynamics, as generally assumed along the Southern Californian coast (Oey, 1999; Hickey, 2003). Along the southern Portuguese coast, Relvas and Barton (2002) estimated a surface slope of about 5 cm over 100 km using tidal gauge data. Simplified momentum analyses similar to the present study confirmed this order of magnitude, which was also corroborated by additional tidal gauge data, satellite altimetry estimates and outputs from numerical models (Sánchez et al., 2006). For comparison, the water surface elevation over 100 km is computed (Eq. 3) for the entire Armona time series assuming that residuals consist solely of the alongshore pressure gradient (Figure 4.12). The elevation is generally larger for EP than PE and skewed toward positive values, with a range of -3 cm and 10 cm and a mean of 3 cm (Figure 4.12b, c). These values are in agreement with previous estimates and support that an alongshore pressure gradient, positive eastward, is the main driver of CCCs.

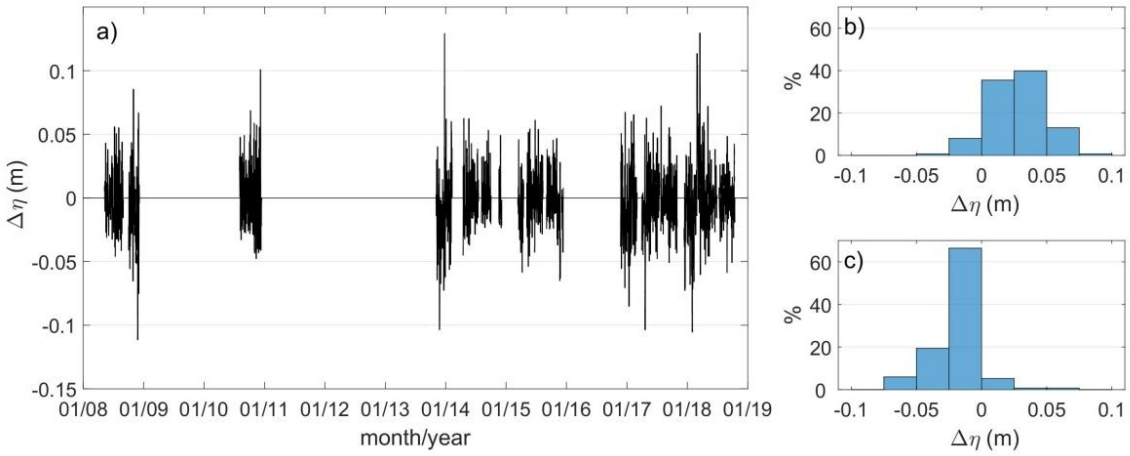

Figure 4.12 - a) Alongshore sea level elevation difference (Δη, in m) over 100 km inferred from Armona ADCP time series; b and c) histograms of Δη for EP and PE events, respectively.

4.6 Conclusions

The structure of poleward coastal counter currents (CCCs) during their setup along the Northern inner shelf of the Gulf of Cadiz (GoC) is examined to get insights about their main physical drivers. Various kinematic parameters are defined to characterize the flow when it changes direction, considering also incipient equatorward flows (EFs) for comparison. Data were collected with a moored ADCP at one station (Armona) located in a region occasionally affected by coastal upwelling. Analysis of the extensive dataset (16 deployments of 1-6 months-long) reveals the main flow structure patterns and its seasonal variability, despite a high intrinsic variability.

By contrast to EFs, CCCs generally develop as dynamic events (i.e., with large parameters such as the vertical shear) occurring through the bed layer first. The differences between both alongshore flows are strongest during the upwelling season, when EFs are typically related to the upwelling process. Observations at a nearby station (Cacela) suggest that these patterns are common along the studied region.

The seasonal analysis indicates an enhanced influence of the wind stress in winter on the setup of alongshore flows. Favourable (i.e., westerly) wind also explains the large occurrence of EFs developing at the surface first during the upwelling season, consistent with the expected development of an upwelling circulation. However, a key finding of this study is that although

70% of CCCs also develop under favourable wind conditions (Levanter), these flows generally change direction near the bed first, in particular in summer, excluding the wind as their main driver in most cases.

The general structure of incipient CCCs strongly suggests that the dominant force competing with the wind stress is an alongshore pressure gradient (APG). In particular, previous studies have described the development of coastal flows through the bed layer in response to fluctuations in the pressure gradient. The depth dependence of the turbulence length scale allows the near-bed layer to adapt faster to the changing conditions (and the near-surface layer to keep longer its momentum). A dominant APG forcing is supported by the remarkable correlation between the eastward flow magnitude (that affects the water slope) and the near-bed westward flow acceleration during wind relaxation. An analysis of the depth-averaged momentum equation strongly supports that the circulation is mainly driven by linear dynamics, with the APG explaining most of the flow variability during CCCs setup.

Overall, based on kinematic parameters describing the flow when it changes direction, the present study presents additional evidence, that CCCs in the GoC are often produced by the unbalance of an APG during the relaxation or reversal of westerly wind.

Supplementary Materials

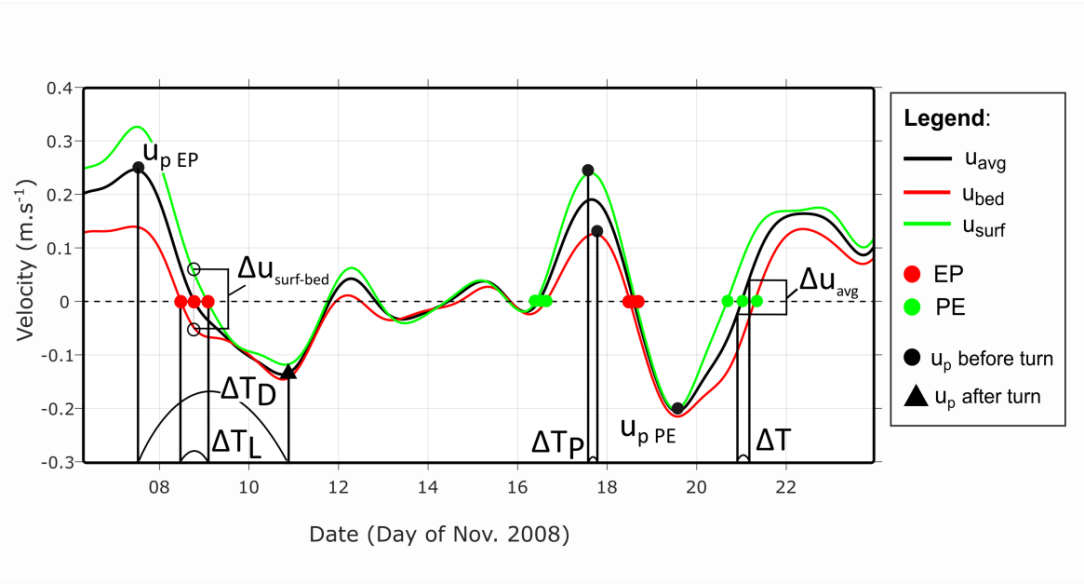

Figure S4.13 - Alongshore flow velocity at Armona exemplifying the parameters used to describe the turn of the flow: Flow Acceleration ($\Delta U/\Delta T$), Peak Velocity (u_p), Event Duration (ΔT_D), Peak Delay (ΔT_P), Vertical Shear (u_{surf}-u_{bed}), and Layers Time Lag (ΔT_L).

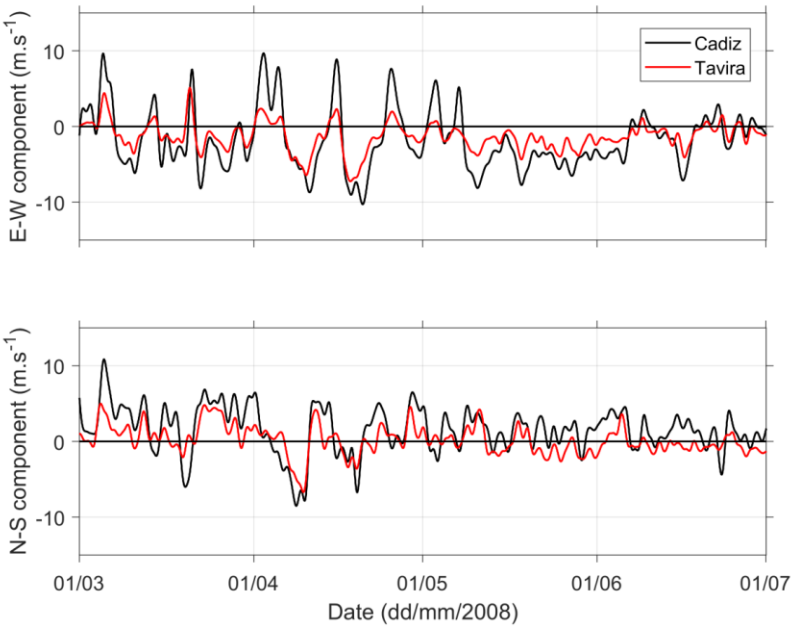

Figure S4.14 - Comparison of the eastern (upper) and northern (lower) wind components at Cadiz offshore buoy and Tavira land station in March-June 2008.

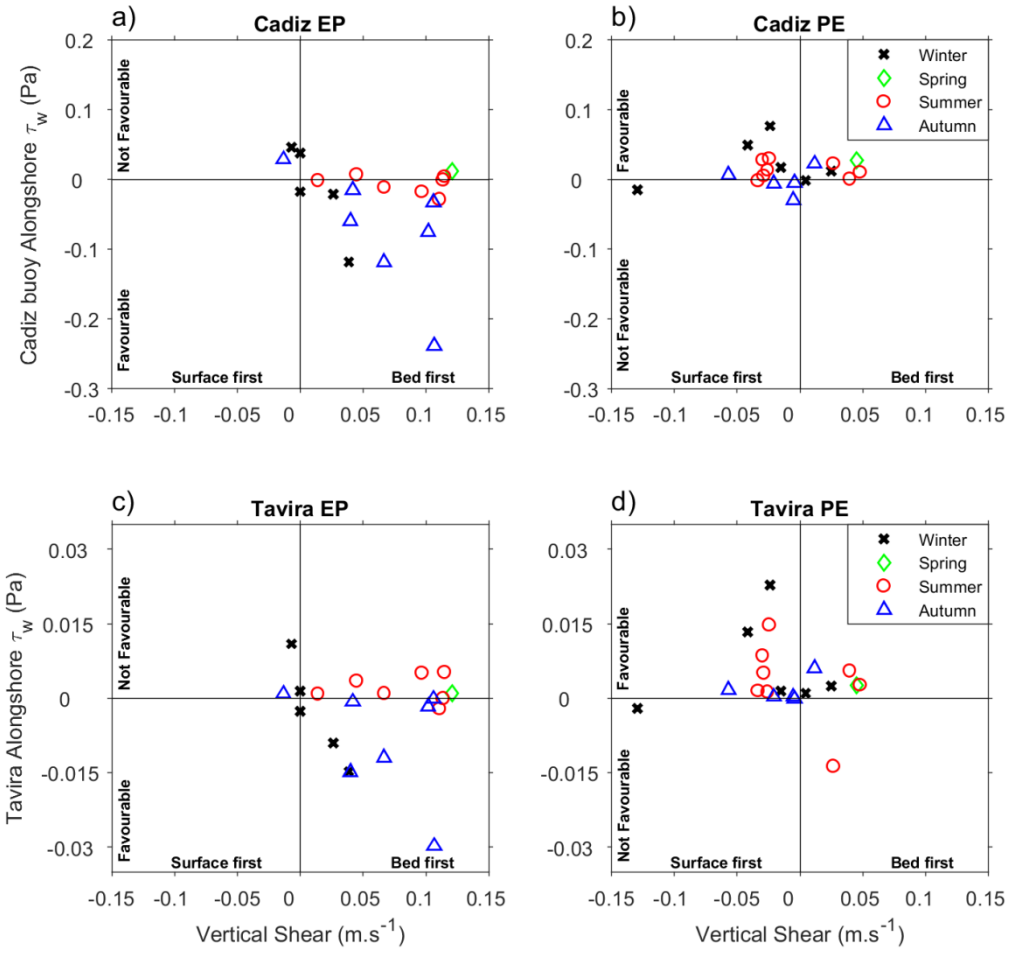

Figure S4.15 - Same as Figure 4.9 but based on the concurrent wind time series at Cadiz offshore buoy and Tavira land station.

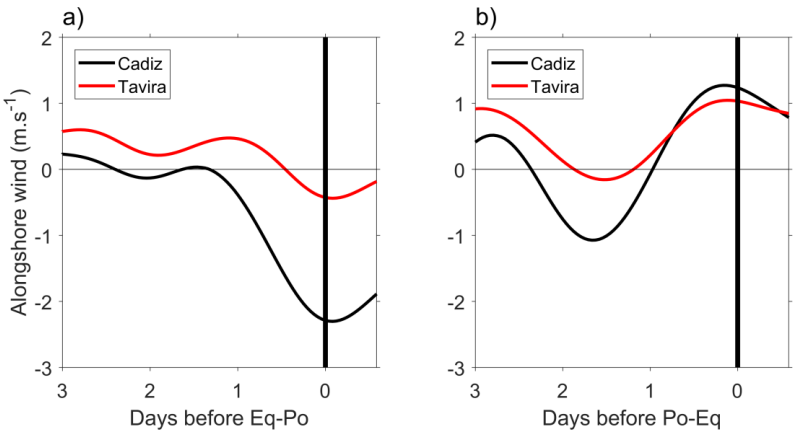

Figure S4.16 - Mean alongshore wind component at Tavira (red) and Cadiz offshore buoy (black) few days before EP (a) and PE (b) events.

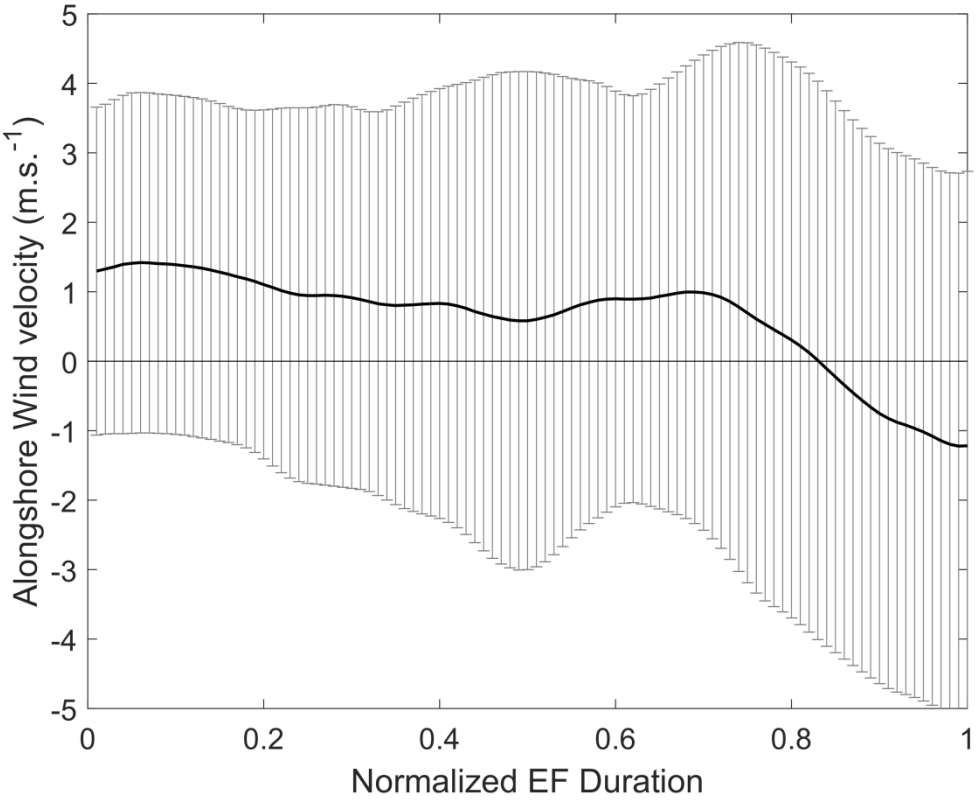

Figure S4.17 - Mean alongshore wind velocity at Cadiz offshore buoy during EF (with standard deviation as error bars). The flow duration was normalized from 0 (start) to 1 (end). The figure is based on 58 events for which the EF maximum velocity occurred towards the end of the flow (duration > 0.6). The mean wind is relatively constant during most of the flow duration (0-0.7) and weakens.

Chapter 5 - Conclusions

A novel set of current velocity observations that includes multi-year (from 2008 to 2019) ADCP vertical profiles at 5 different locations and 4.5 years (2016-2020) of surface velocities from HFR was exploited to complement the understanding of the ocean circulation along the NMGoC between 9ºW and 7ºW approximately. The existing literature is based on relatively few direct observations, mostly centred around summer, and provides an incomplete description of the general circulation patterns. Consequently, several aspects of the physical processes involved are unclear or debatable. Therefore, the main objective of this Thesis was to characterize the circulation based on observations updating the understating of the main patterns and also to provide an additional explanation for the dynamics involved.

The extensive analysis of the main surface circulation patterns from HFR provided additional details on pathways of the slope circulation that is composed of a permanent jet-like flow, the GCC, that was shown to be a dominant feature of the slope circulation from 9ºW to 7ºW. An important contribution of this work was to show for the first time how the GCC is seasonally modulated over the western bight, being on average weak and narrow in winter while in summer it is strong and wide. Evidence of the GCC modulation dynamics was provided by the estimations of Ekman transport and Ekman pumping mechanisms from high-resolution modelled winds. Main results showed that the seasonal and spatial variability of the different upwelling mechanisms are associated with the variability (strength and location) of the cross-shore pressure gradient, which in turn contributes significantly to the meridional position of the GCC core.

Over the shelf, long-term ADCP and HFR observations showed that the circulation is overall balanced, polarized in the alongshore direction and fluctuates with the wind. Statistical analysis of the EFs vertical structure at the time of flow reversals, showed that these flows often reverse through the surface layers indicating that they are driven by the dominant western component of the wind. EFs were generally associated with the advection of cold water supporting that it is associated with upwelling dynamics. In addition, HFR data analysis showed that these flows constitute the lateral extension, on the shelf, of the GCC, similar to a classical wind-driven upwelling circulation.

Despite the dominance of the western component of the wind shown by in situ and modelled wind analysis, quantifications based on HFR currents showed that shelf PFs are balanced with EFs in most regions. According to the literature, PFs are generally regarded as CCC and are mainly driven by an APG. In the present study, a set of additional evidence was presented to confirm the existence of this forcing agent:

- Observations from HFR and ADCP along the coast showed that PFs often develop under relaxation of dominant upwelling favourable (modelled and observed) winds.
- Seasonal mean sea level anomalies from satellite altimetry confirmed the existence of a permanent APG that is strongest in summer. Instantaneous estimates of the APG in summer showed that its magnitude, which is comparable with the estimations from tide gauges, could effectively drive these currents.
- PFs reversals do not propagate along the coast. Instead, PFs reversals develop relatively at the same time along the NMGoC, in concordance with the existence of a local mesoscale pressure gradient driving these currents simultaneously.
- At Armona ADCP station, PFs generally change direction near the bed first (66%). This behaviour results from the depth dependence of the turbulence length scale that allows the near bed layer to adapt faster to the changes in the pressure gradient, and the near-surface layer to keep longer its momentum toward the east. In support, near-bed flow reversals are most observed (81%) and present the highest vertical shear in summer, when the APG is also strongest.
- A simplified momentum analysis corroborates the existence of a dominant pressure gradient during the PFs setup. The magnitude of the inferred gradient agrees with the magnitude of estimations in the literature and from altimetry data.

During the upwelling season, PFs are generally observed up to the shelf break where they are bounded by the equatorward GCC. However, in winter stronger winds may promote flow reversal over the entire NMGoC, including the GCC. This clear spatial structure difference shows that not all PFs are CCCs. From this definition, it was possible to quantify that CCCs develop predominantly (>60 %) during the upwelling season and are the rarest (<10 %) in late autumn and winter. Nevertheless, the vertical structure of the incipient PFs remains marked by

the development through the bed layers even under favourable wind conditions, confirming that the APG is a key forcing for triggering PFs throughout the year.

The shelf circulation was shown to be independent of the slope circulation. The dominant GCC only reverses under strong winds whereas the shelf circulation is more variable. Nevertheless, analysis of the HFR observations showed that shelf and slope flows interact episodically through a cyclonic circulation at the western bight during the upwelling season. The permanent and strong effect of Ekman pumping anchored at CSV is argued to sustain an overall circular-shaped depression in the sea level over the western bight as indicated by satellite altimetry. The dynamic adjustment of this depression favours the development of a cyclonic circulation that promotes offshore flows near CSV and onshore flows near CSM. The recirculation of PFs near CSV has important consequences for productivity as it promotes offshore transport of water from a nutrient-reach region towards a more oligotrophic one.

Overall, the detailed analysis of the current observations together with the other relevant environmental parameters provides a holistic understanding of the coastal and slope circulation at various temporal and spatial scales. One of the main outcomes of the present study was the production of an updated conceptual model of the spring and summer surface circulation. The integration of the main results suggests that the circulation at the NMGoC, is highly affected by the atmosphere-ocean interaction through modulation of the pressure field induced by a spatially and temporally variable upwelling processes.

Future work

The origin of the APG was shown to be associated with the localized effect of Ekman pumping as it promotes a variable upwelling intensity along the coast. However, a direct estimation of the APG remains to be done and future studies should aim at obtaining measurements from pressure sensors or sea level fluctuations from tide gauges. Furthermore, other potential mechanisms such as buyancy imputs and flow topography interactions may also be significant contributors to the development of the APG. To assess the thermal effect, long-term stratification measurements are essential. Preferably, stratification should be measured at least in the extremities of the NMGoC which are marked by significant temperature differences in summer. The contribution from the interaction of the flow with the topography to the APG

development could be estimated from process-orientated simulations, through the application of numerical models capable of reproducing the patterns described in this study.

References

Alvarez, I., Gomez-Gesteira, M., de Castro, M., & Dias, J. M. (2008). Spatiotemporal evolution of upwelling regime along the western coast of the Iberian Peninsula. Journal of Geophysical Research: Oceans, 113(7). https://doi.org/10.1029/2008JC004744

Alvera-Azcárate, A., Barth, A., Rixen, M., & Beckers, J. M. (2005). Reconstruction of incomplete oceanographic data sets using empirical orthogonal functions: Application to the Adriatic Sea surface temperature. Ocean Modelling, 9(4), 325–346. https://doi.org/10.1016/j.ocemod.2004.08.001

Ambar, I., Serra, N., Brogueira, M. J., Cabeçadas, G., Abrantes, F., Freitas, P., et al. (2002). Physical, chemical and sedimentological aspects of the Mediterranean outflow off Iberia. Deep-Sea Research Part II: Topical Studies in Oceanography, 49(19), 4163–4177. https://doi.org/10.1016/S0967-0645(02)00148-0

Arístegui, J., Barton, E. D., Álvarez-Salgado, X. A., Santos, A. M. P., Figueiras, F. G., Kifani, S., et al. (2009). Sub-regional ecosystem variability in the Canary Current upwelling. Progress in Oceanography, 83(1–4), 33–48. https://doi.org/10.1016/j.pocean.2009.07.031

ASCAT - Remote Sensing Systems and sponsored by NASA. Retrieved 21 January, 2022 from www.remss.com

Bakun, A. (1973). Coastal upwelling indices, west coast of North America, 1946–1971. NOAA Tech. Rep. NMFS SSFR-671, 103. https://doi.org/NMFSSSRF-671

Beckers, J. M., & Rixen, M. (2003). EOF Calculations and Data Filling from Incomplete Oceanographic Datasets. Journal of Atmospheric and Oceanic Technology, 20(12), 1839–1856. https://doi.org/10.1175/1520-0426(2003)020<1839:ECADFF>2.0.CO;2

Bellanco, M. J., & Sánchez-Leal, R. F. (2016). Spatial distribution and intra-annual variability of water masses on the Eastern Gulf of Cadiz seabed. Continental Shelf Research, 128(January), 26–35. https://doi.org/10.1016/j.csr.2016.09.001

Benazzouz, A., Mordane, S., Orbi, A., Chagdali, M., Hilmi, K., Atillah, A., et al. (2014). An improved coastal upwelling index from sea surface temperature using satellite-based approach - The case of the Canary Current upwelling system. Continental Shelf Research, 81, 38–54. https://doi.org/10.1016/j.csr.2014.03.012

Boavida, J., Paulo, D., Aurelle, D., Arnaud-Haond, S., Marschal, C., Reed, J., et al. (2016). A well-kept treasure at depth: Precious red coral rediscovered in Atlantic deep coral gardens (SW Portugal) after 300 Years. PLoS ONE, 11(1), 1–26. https://doi.org/10.1371/journal.pone.0147228

Boyd, A. J., & Nelson, G. (1998). Variability of the Benguela Current off the Cape Peninsula, South Africa. South African Journal of Marine Science, 19(1), 27–39. https://doi.org/10.2989/025776198784126665

Bravo, L., Ramos, M., Astudillo, O., Dewitte, B., & Goubanova, K. (2016). Seasonal variability of the Ekman transport and pumping in the upwelling system off central-northern Chile (∼ 30° S) based on a high-resolution atmospheric regional model (WRF). Ocean Science, 12(5), 1049–1065. https://doi.org/10.5194/os-12-1049-2016

Bueno-Pardo, J., Ramalho, S. P., García-Alegre, A., Morgado, M., Vieira, R. P., Cunha, M. R., & Queiroga, H. (2017). Deep-sea crustacean trawling fisheries in Portugal: Quantification of effort and assessment of landings per unit effort using a Vessel Monitoring System (VMS). Scientific Reports, 7(December 2016), 1–10. https://doi.org/10.1038/srep40795

Burchard, H., Bolding, K., Rippeth, T. P., Stips, A., Simpson, J. H., & Sündermann, J. (2002). Microstructure of turbulence in the northern North Sea: a comparative study of observations and model simulations. Journal of Sea Research, 47(3–4), 223–238. https://doi.org/10.1016/S1385-1101(02)00126-0

Capet, X. J., Marchesiello, P., & McWilliams, J. C. (2004). Upwelling response to coastal wind profiles. Geophysical Research Letters, 31(13), 1–4. https://doi.org/10.1029/2004GL020123

Capon, R. A. (2006). High resolution studies of the Gibraltar Levanter validated using sun-glint anemometry. Meteorological Applications, 13(03), 257–265. https://doi.org/10.1017/S135048270600226X

Castelao, R. M., & Barth, J. A. (2006). Upwelling around Cabo Frio, Brazil: The importance of wind stress curl. Geophysical Research Letters, 33(3), 2–5. https://doi.org/10.1029/2005GL025182

Castelao, R. M., & Barth, J. A. (2007). The Role of Wind Stress Curl in Jet Separation at a Cape, (June 2000), 2652–2672. https://doi.org/10.1175/2007JPO3679.1

Castelao, R. M., & Luo, H. (2018). Upwelling jet separation in the California Current System. Scientific Reports, (August), 1–8. https://doi.org/10.1038/s41598-018-34401-y

Chapman, R. D., Shay, L. K., Graber, H. C., Edson, J. B., Karachintsev, A., Trump, C. L., & Ross, D. B. (1997). On the accuracy of HF radar surface current measurements: Intercomparisons with ship-based sensors. Journal of Geophysical Research: Oceans, 102(C8), 18737–18748. https://doi.org/10.1029/97JC00049

Chase, J. (1951). The Bermuda-Azores High Pressure Cell; its surface wind circulation. Woods Hole Oceanographic Institution (Vol. 20).

CMEMS Service Evolution. (2017). Report on European HF Radar systems development and roadmap for HF Radar products evolution in compliance with CMEMS needs. http://www.cmems-increase.eu/static/INCREASE_Report_D1.1.pdf

CODAR (2004a): About Baseline Interpolation, Manual. Retrieved March 15, 2021, from http://support.codar.com/Technicians_Information_Page_for_SeaSondes/Docs/Informative/Baseline_Interpolation.pdf

CODAR (2004b): Obtaining Total Current Velocities from Radials, Manual. Retrieved March 15, 2021 from http://support.codar.com/Technicians_Information_Page_for_SeaSondes/Docs/Informative/Combining_Radials.pdf

Cravo, A., Relvas, P., Cardeira, S., & Rita, F. (2013). Nutrient and chlorophyll a transports during an upwelling event in the NW margin of the Gulf of Cadiz. Journal of Marine Systems, 128, 208–221. https://doi.org/10.1016/j.jmarsys.2013.05.001

Criado-Aldeanueva, F., García-Lafuente, J., Vargas, J. M., Del Río, J., Vázquez, A., Reul, A., & Sánchez, A. (2006). Distribution and circulation of water masses in the Gulf of Cadiz from in situ observations. Deep-Sea Research Part II: Topical Studies in Oceanography, 53(11–13), 1144–1160. https://doi.org/10.1016/j.dsr2.2006.04.012

Criado-Aldeanueva, F., García-Lafuente, J., Vargas, J. M., Del Río, J., Sánchez, A., Delgado, J., & Sánchez, J. C. (2006). Wind induced variability of hydrographic features and water masses distribution in the Gulf of Cadiz (SW Iberia) from in situ data. Journal of Marine Systems, 63(3–4), 130–140. https://doi.org/10.1016/j.jmarsys.2006.06.005

Criado-Aldeanueva, F., García-Lafuente, J., Navarro, G., & Ruiz, J. (2009). Seasonal and interannual variability of the surface circulation in the eastern Gulf of Cadiz (SW Iberia). Journal of Geophysical Research, 114(C1), C01011. https://doi.org/10.1029/2008JC005069

Csanady, G. T. (1984). The Free Surface Turbulent Shear layer. Journal of Physical Oceanography, 14(2), 402–411. https://doi.org/10.1175/1520-0485(1984)014<0402:TFSTSL>2.0.CO;2

de Oliveira Júnior, L., Garel, E., & Relvas, P. (2021). The structure of incipient coastal counter currents in South Portugal as indicator of their forcing agents. Journal of Marine Systems, 214(October 2020), 103486. https://doi.org/10.1016/j.jmarsys.2020.103486

de Oliveira Júnior, Luciano, Relvas, P., & Garel, E. (2022). Kinematics of surface currents at the northern margin of the Gulf of Cádiz. Ocean Science, 18(4), 1183–1202. https://doi.org/10.5194/os-18-1183-2022

do Valle, P. O., Pintassilgo, P., Matias, A., & André, F. (2012). Tourist attitudes towards an accommodation tax earmarked for environmental protection: A survey in the Algarve. Tourism Management, 33(6), 1408–1416. https://doi.org/10.1016/j.tourman.2012.01.003

Dickey, T. D., & Simpson, J. J. (1983). The sensitivity of upper ocean structure to time varying wind direction. Geophysical Research Letters, 10(2), 133–136.

Díez-Minguito, M., Baquerizo, A., Ortega-Sánchez, M., Navarro, G., & Losada, M. A. (2012). Tide transformation in the Guadalquivir estuary (SW Spain) and process-based zonation. Journal of Geophysical Research, 117(C03019), C03019. https://doi.org/10.1029/2011JC007344

di Lorenzo, E. (2003). Seasonal dynamics of the surface circulation in the Southern California Current System. Deep-Sea Research Part II: Topical Studies in Oceanography, 50(14–16), 2371–2388. https://doi.org/10.1016/S0967-0645(03)00125-5

Dorman, C. E., Beardsley, R. C., & Limeburner, R. (1995). Winds in the strait of Gibraltar. Quarterly Journal of the Royal Meteorological Society, 121(528), 1903–1921. https://doi.org/10.1002/qj.49712152807

Dronkers, J. (2005). Dynamics of Coastal Systems (Vol. 25). World Scientific. https://doi.org/10.1142/5781

Dudas, S. E., Grantham, B. A., Kirincich, A. R., Menge, B. A., Lubchenco, J., & Barth, J. A. (2009). Current reversals as determinants of intertidal recruitment on the central Oregon coast. ICES Journal of Marine Science, 66(2), 396–407. https://doi.org/10.1093/icesjms/fsn179

Ekman, V. W. (1905). On the Influence of the Earth's Rotation on Ocean-Currents. Arkiv För Matematick Astronomi Och Fysik, 2(11), 1–52.

CMEMS. Altimeter satellite gridded Sea Level Anomalies (SLA) computed with respect to a twenty-year 1993, 2012 mean. product identifier: SEALEVEL_EUR_PHY_L4_MY_008_068 Retrieved January 21, 2022 from https://doi.org/10.48670/moi-00141

CMEMS. Optimally interpolated night time sea surface temperature (SST) fields product identifier: SST_MED_SSTA_L4_NRT_OBSERVATIONS_010_004 Retrieved January 21, 2022 from

Fawcett, A. L., Pitcher, G. C., & Shillington, F. A. (2008). Nearshore currents on the southern Namaqua shelf of the Benguela upwelling system. Continental Shelf Research, 28(8), 1026–1039. https://doi.org/10.1016/j.csr.2008.02.005

Ferreira Cordeiro, N. G., Dubert, J., Nolasco, R., & Desmond Barton, E. (2018). Transient response of the Northwestern Iberian upwelling regime. PLoS ONE, 13(5), e0197627. https://doi.org/10.1371/journal.pone.0197627

Fewings, M. R., Washburn, L., Dorman, C. E., Gotschalk, C., & Lombardo, K. (2016). Synoptic forcing of wind relaxations at Pt. Conception, California. Journal of Geophysical Research: Oceans, 121(8), 5711–5730. https://doi.org/10.1002/2016JC011699

Fiúza, A. F. G., de Macedo, M. E., & Guerreiro, M. R. (1982). Climatological space and time variation of the Portuguese coastal upwelling. Oceanologica Acta, 5(1), 31–40. http://archimer.ifremer.fr/doc/00120/23169/21014.pdf

Fiúza, Armando F. G. (1983). Upwelling Patterns off Portugal. In E. Suess & J. Thiede (Eds.), Coastal Upwelling Its Sediment Record (pp. 85–98). Boston, MA: Springer US. https://doi.org/10.1007/978-1-4615-6651-9_5

Folkard, A. M., Davies, P. A., Fiúza, A. F. G., & Ambar, I. (1997). Remotely sensed sea surface thermal patterns in the gulf of-cadiz and the strait of Gibraltar: Variability, correlations, and relationships with the surface wind field. Journal of Geophysical Research C: Oceans, 102(C3), 5669–5683. https://doi.org/10.1029/96JC02505

Gan, J., & Allen, J. S. (2002). A modeling study of shelf circulation off northern California in the region of the Coastal Ocean Dynamics Experiment: Response to relaxation of upwelling winds. Journal of Geophysical Research, 107(C9), 3123. https://doi.org/10.1029/2000JC000768

García-Lafuente, J., Sammartino, S., Huertas, I. E., & Flecha, S. (2021). Hotter and Weaker Mediterranean Outflow as a Response to Basin-Wide Alterations, (March). https://doi.org/10.3389/fmars.2021.613444

García-Lafuente, J., Delgado, J., Criado-Aldeanueva, F., Bruno, M., del Río, J., & Miguel Vargas, J. (2006). Water mass circulation on the continental shelf of the Gulf of Cádiz. Deep Sea Research Part II: Tropical Studies in Oceanography, 53(11–13), 1182–1197. https://doi.org/10.1016/j.dsr2.2006.04.011

García-Lafuente, J., Sánchez-Román, A., Naranjo, C., & Sánchez-Garrido, J. C. (2011). The very first transformation of the Mediterranean outflow in the Strait of Gibraltar. Journal of Geophysical Research, 116(C7), C07010. https://doi.org/10.1029/2011JC006967

Garcia, C. M., Prieto, L., Vargas, M., Echevarría, F., Garcia-Lafuente, J., Ruiz, J., & Rubin, J. P. (2002). Hydrodynamics and the spatial distribution of plankton and TEP in the Gulf of Cadiz (SW Iberian Peninsula). Journal of Plankton Research, 24(January), 817–833. https://doi.org/10.1093/plankt/24.8.817

García Lafuente, J., & Ruiz, J. (2007). The Gulf of Cádiz pelagic ecosystem: A review. Progress in Oceanography, 74(2–3), 228–251. https://doi.org/10.1016/j.pocean.2007.04.001

Garel, E., & D'Alimonte, D. (2017). Continuous river discharge monitoring with bottom-mounted current profilers at narrow tidal estuaries. Continental Shelf Research, 133(October 2016), 1–12. https://doi.org/10.1016/j.csr.2016.12.001

Garel, E., Laiz, I., Drago, T., & Relvas, P. (2016). Characterisation of coastal counter-currents on the inner shelf of the Gulf of Cadiz. Journal of Marine Systems, 155, 19–34. https://doi.org/10.1016/j.jmarsys.2015.11.001

Geyer, W. R., & MacCready, P. (2014). The Estuarine Circulation. Annual Review of Fluid Mechanics, 46(1), 175–197. https://doi.org/10.1146/annurev-fluid-010313-141302

Gill, A. E. (1982). Atmosphere-Ocean Dynamics. Academic Press, New York, 662.

Gómez, F. (2003). The role of the exchanges through the Strait of Gibraltar on the budget of elements in the Western Mediterranean Sea: Consequences of human-induced modifications. Marine Pollution Bulletin, 46(6), 685–694. https://doi.org/10.1016/S0025-326X(03)00123-1

González-Ortegón, E., Laiz, I., Sánchez-Quiles, D., Cobelo-Garcia, A., & Tovar-Sánchez, A. (2019). Trace metal characterization and fluxes from the Guadiana, Tinto-Odiel and Guadalquivir estuaries to the Gulf of Cadiz. Science of The Total Environment, 650, 2454–2466. https://doi.org/10.1016/j.scitotenv.2018.09.290

Harms, S., & Winant, C. D. (1998). Characteristic patterns of the circulation in the Santa Barbara Channel. Journal of Geophysical Research, 103(C2), 3041–3065. https://doi.org/10.1029/97JC02393

Hersbach, H., Bell, B., Berrisford, P., Biavati, G., Horányi, A., Muñoz Sabater, J., Nicolas, J., Peubey, C., Radu, R., Rozum, I., Schepers, D., Simmons, A., Soci, C., Dee, D., Thépaut, J-N. (2018): ERA5 hourly data on pressure levels from 1940 to present. Copernicus Climate Change Service (C3S) Climate Data Store (CDS), https://doi.org/10.24381/cds.bd0915c6

Hernández-Carrasco, I., Solabarrieta, L., Rubio, A., Esnaola, G., Reyes, E., & Orfila, A. (2018). Impact of HF radar current gap-filling methodologies on the Lagrangian assessment of coastal dynamics. Ocean Science, 14(4), 827–847. https://doi.org/10.5194/os-14-827-2018

Hickey, B. M. (2003). Local and remote forcing of currents and temperature in the central Southern California Bight. Journal of Geophysical Research, 108(C3), 3081. https://doi.org/10.1029/2000JC000313

Hickey, Barbara M. (1979). The California current system—hypotheses and facts. Progress in Oceanography, 8(4), 191–279. https://doi.org/10.1016/0079-6611(79)90002-8

Hoinka, K. P., & De Castro, M. (2003). The Iberian Peninsula thermal low. Quarterly Journal of the Royal Meteorological Society, 129(590 PART A), 1491–1511. https://doi.org/10.1256/qj.01.189

Huyer, A., & Kosro, P. M. (1987). Mesoscale surveys over the shelf and slope in the upwelling region near Point Arena, California. Journal of Geophysical Research, 92(C2), 1655–1681. https://doi.org/10.1029/JC092iC02p01655

Iorga, M. C., & Lozier, M. S. (1999). Signatures of the Mediterranean outflow from a North Atlantic climatology 1. Salinity and density fields. Journal of Geophysical Research: Oceans, 104(C11), 25985–26009. https://doi.org/10.1029/1999jc900115

Ivanovic, R. F., Valdes, P. J., Gregoire, L., Flecker, R., & Gutjahr, M. (2014). Sensitivity of modern climate to the presence, strength, and salinity of Mediterranean-Atlantic exchange in a global general circulation model. Climate Dynamics, 42(3–4), 859–877. https://doi.org/10.1007/s00382-013-1680-5

Janjic, Z. I., Gerrity, J., & Nickovic, S. (2001). An alternative approach to nonhydrostatic modelling. Monthly Weather Review, 129(5), 1164–1178. https://doi.org/10.1175/1520-0493(2001)129<1164:AAATNM>2.0.CO;2

Jayaram, C., & Jose, F. (2022). Relative dominance of wind stress curl and Ekman transport on coastal upwelling during summer monsoon in the south-eastern Arabian Sea. Continental Shelf Research, 244(June 2021), 104782. https://doi.org/10.1016/j.csr.2022.104782

Kaihatu, J. M., Handler, R. A., Marmorino, G. O., & Shay, L. K. (1998). Empirical orthogonal function analysis of ocean surface currents using complex and real-vector methods. Journal of Atmospheric and Oceanic Technology, 15(4), 927–941. https://doi.org/10.1175/1520-0426(1998)015<0927:EOFAOO>2.0.CO;2

Kallos, G., Papadopoulos, A., Katsafados, P., & Nickovic, S. (2006). Transatlantic Saharan dust transport: Model simulation and results. Journal of Geophysical Research Atmospheres, 111(9), 1–11. https://doi.org/10.1029/2005JD006207

Kämpf, J., & Chapman, P. (2016). Upwelling Systems of the World. Upwelling Systems of the World. Springer International Publishing. https://doi.org/10.1007/978-3-319-42524-5

Kaplan, D. M., Largier, J., & Botsford, L. W. (2005). HF radar observations of surface circulation off Bodega Bay (northern California, USA). Journal of Geophysical Research, 110(10), 1–25. https://doi.org/10.1029/2005JC002959

Kida, S., Price, J. F., & Yang, J. (2008). The upper-oceanic response to overflows: A mechanism for the Azores current. Journal of Physical Oceanography, 38(4), 880–895. https://doi.org/10.1175/2007JPO3750.1

KNMI. (2007). ASCAT Wind Product User Manual. Retrieved from https://scatterometer.knmi.nl/old_manuals/ss3_pm_ascat_1.0.pdf

Kokkini, Z., Potiris, M., Kalampokis, A., & Zervakis, V. (2014). HF Radar observations of the Dardanelles outflow current in the north-eastern Aegean using validated WERA HF radar data. Mediterranean Marine Science, 15(4), 753–768. https://doi.org/10.12681/mms.938

Kudryavtsev, V., Shrira, V., Dulov, V., & Malinovsky, V. (2008). On the Vertical Structure of Wind-Driven Sea Currents. Journal of Physical Oceanography, 38(10), 2121–2144. https://doi.org/10.1175/2008JPO3883.1

Kundu, P. K., & Allen, J. S. (1976). Some Three-Dimensional Characteristics of Low-Frequency Current Fluctuations near the Oregon Coast. Journal of Physical Oceanography, 6(2), 181–199. https://doi.org/10.1175/1520-0485(1976)006<0181:STDCOL>2.0.CO;2

Laiz, I., Plecha, S., Teles-Machado, A., González-Ortegón, E., Sánchez-Quiles, D., Cobelo-García, A., et al. (2020). The role of the Gulf of Cadiz circulation in the redistribution of trace metals between the Atlantic Ocean and the Mediterranean Sea. Science of the Total Environment, 719, 134964. https://doi.org/10.1016/j.scitotenv.2019.134964

Large, W. G., & Pond, S. (1981). Open Ocean Momentum Flux Measurements in Moderate to Strong Winds. Journal of Physical Oceanography, 11(3), 324–336. https://doi.org/10.1175/1520-0485(1981)011<0324:OOMFMI>2.0.CO;2

Largier, J. L., Magnell, B. A., & Winant, C. D. (1993). Subtidal circulation over the northern California shelf. Journal of Geophysical Research, 98(C10), 18147–18179. https://doi.org/10.1029/93JC01074

Leitão, F., Relvas, P., Cánovas, F., Baptista, V., & Teodósio, A. (2018). Northerly wind trends along the Portuguese marine coast since 1950. Theoretical and Applied Climatology, (April), 1–19. https://doi.org/10.1007/s00704-018-2466-9

Lentz, S. J., & Winant, C. D. (1986). Sub inertial Currents on the Southern California Shelf. Journal of Physical Oceanography, 16(11), 1737–1750. https://doi.org/10.1175/1520-0485(1986)016<1737:SCOTSC>2.0.CO;2

Li, C. (2011). Free Surface Motions. In Treatise on Estuarine and Coastal Science (Vol. 2, pp. 91–122). Elsevier. https://doi.org/10.1016/B978-0-12-374711-2.00202-3

Lipa, B., Barrick, D., Alonso-Martirena, A., Fernandes, M., Ferrer, M. I., & Nyden, B. (2014). Brahan project high frequency radar ocean measurements: Currents, winds, waves and their interactions. Remote Sensing, 6(12), 12094–12117. https://doi.org/10.3390/rs61212094

Lipa, B. J., & Barrick, D. E. (1983). Least-Squares Methods for the Extraction of Surface Currents from CODAR Crossed-Loop Data: Application at ARSLOE. IEEE Journal of Oceanic Engineering, 8(4), 226–253. https://doi.org/10.1109/JOE.1983.1145578

Lorente, P., Piedracoba, S., & Fanjul, E. A. (2015). Validation of high-frequency radar ocean surface current observations in the NW of the Iberian Peninsula. Continental Shelf Research, 92, 1–15. https://doi.org/10.1016/j.csr.2014.11.001

Losada, A. M. P. (1999). Analysis of the meteorological synoptic situations that affect the Straits of Gibraltar and their influence on the surface wind. Boletin Instituto Español de Oceanografia, 15, 81–90.

Lozier, M. S., Owens, W. B., & Curry, R. G. (1995). The climatology of the North Atlantic. Progress in Oceanography, 36(1), 1–44. https://doi.org/10.1016/0079-6611(95)00013-5

Mace, A. J., & Morgan, S. G. (2006). Biological and physical coupling in the lee of a small headland: contrasting transport mechanisms for crab larvae in an upwelling region. Marine Ecology Progress Series, 324(October 2006), 185–196. https://doi.org/10.3354/meps324185

Maiwa, K., Masumoto, Y., & Yamagata, T. (2010). Characteristics of coastal trapped waves along the southern and eastern coasts of Australia. Journal of Oceanography, 66(2), 243–258. https://doi.org/10.1007/s10872-010-0022-z

Mauritzen, C., Morel, Y., & Paillet, J. (2001). On the influence of Mediterranean Water on the Central Waters of the North Atlantic Ocean. Deep Sea Research Part I, 48(2), 347–381. https://doi.org/10.1016/S0967-0637(00)00043-1

Mazé, J. P., Arhan, M., & Mercier, H. (1997). Volume budget of the eastern boundary layer off the Iberian Peninsula. Deep-Sea Research Part I: Oceanographic Research Papers, 44(9–10), 1543–1574. https://doi.org/10.1016/S0967-0637(97)00038-1

McDowell, S. E., & Rossby, H. T. (1978). Mediterranean water: An intense mesoscale eddy off the Bahamas. Science, 202(4372), 1085–1087. https://doi.org/10.1126/science.202.4372.1085

Melton, C., Washburn, L., & Gotschalk, C. (2009). Wind relaxations and poleward flow events in a coastal upwelling system on the central California coast. Journal of Geophysical Research, 114(C11), C11016. https://doi.org/10.1029/2009JC005397

Münchow, A. (2000). Wind stress curl forcing of the coastal ocean near Point Conception, California. Journal of Physical Oceanography, 30(6), 1265–1280. https://doi.org/10.1175/1520-0485(2000)030<1265:WSCFOT>2.0.CO;2

Navarro, G., & Ruiz, J. (2006). Spatial and temporal variability of phytoplankton in the Gulf of Cádiz through remote sensing images. Deep Sea Research Part II: Topical Studies in Oceanography, 53(11–13), 1241–1260. https://doi.org/10.1016/j.dsr2.2006.04.014

Nencioli, F., Dong, C., Dickey, T., Washburn, L., & Mcwilliams, J. C. (2010). A vector geometry-based eddy detection algorithm and its application to a high-resolution numerical model product and high-frequency radar surface velocities in the Southern California Bight. Journal of Atmospheric and Oceanic Technology, 27(3), 564–579. https://doi.org/10.1175/2009JTECHO725.1

Nunes, R., Alvim-Ferraz, M., Martins, F., Calderay-Cayetano, F., Durán-Grados, V., Moreno-Gutiérrez, J., et al. (2020). Shipping emissions in the Iberian Peninsula and its impacts on air quality. Atmospheric Chemistry and Physics Discussions, 1–28. https://doi.org/10.5194/acp-2019-1186

Ocean Color Data: Level 3 VIIRS-SNPP SST data. Retrieved November 15, 2021 from https://oceandata.sci.gsfc.nasa.gov

Oertel, H. (2004). Prandtl's Essentials of Fluid Dynamics. (M. Böhle, D. Etling, U. Müller, J. R. Sreenivasan, U. Riedel, & J. Warnatz, Eds.), Applied Mathematical Sciences (2nd Ed., Vol. 158). New York: Springer. https://doi.org/10.2307/3615195

Oey, L. Y. (1996). Flow around a coastal bend: A model of the Santa Barbara Channel eddy. Journal of Geophysical Research: Oceans, 101(C7), 16667–16682. https://doi.org/10.1029/96JC01232

Oey, L. Y. (1999). A forcing mechanism for the poleward flow off the southern California coast. Journal of Geophysical Research: Oceans, 104(C6), 13529–13539. https://doi.org/10.1029/1999jc900066

Oey, L. Y., Wang, D. P., Hayward, T., Winant, C., & Hendershott, M. (2001). "Upwelling" and "cyclonic" regimes of the near-surface circulation in the Santa Barbara Channel. Journal of Geophysical Research: Oceans, 106(C5), 9213–9222. https://doi.org/10.1029/1999jc000129

Ortega, C., Nogueira, C., & Pinto, H. (2013). Sea and littoral localities' economy: Exploring potentialities for a maritime cluster - An integrated analysis of Huelva, Spain and Algarve, Portugal. Journal of Maritime Research, 10(2), 35–42.

Paduan, J. D., & Rosenfeld, L. K. (1996). Remotely sensed surface currents in Monterey Bay from shore-based HF radar (Coastal Ocean Dynamics Application Radar). Journal of Geophysical Research C: Oceans, 101(C9), 20669–20686. https://doi.org/10.1029/96JC01663

Paduan, J. D., & Washburn, L. (2013). High-frequency radar observations of ocean surface currents. Annual Review of Marine Science, 5, 115–136. https://doi.org/10.1146/annurev-marine-121211-172315

Papadopoulos, A., Katsafados, P., Kallos, G., & Nickovic, S. (2002). The weather forecasting system for POSEIDON - An overview. Global Atmosphere and Ocean System, 8(2–3), 219–237. https://doi.org/10.1080/1023673029000003543

Peliz, A., Dubert, J., Marchesiello, P., & Teles-Machado, A. (2007). Surface circulation in the Gulf of Cadiz: Model and mean flow structure. Journal of Geophysical Research, 112(C11), C11015. https://doi.org/10.1029/2007JC004159

Peliz, A., Marchesiello, P., Santos, A. M. P., Dubert, J., Teles-Machado, A., Marta-Almeida, M., & Le Cann, B. (2009). Surface circulation in the Gulf of Cadiz: 2. Inflow-outflow coupling and the Gulf of Cadiz slope current. Journal of Geophysical Research, 114(C3), C03011. https://doi.org/10.1029/2008JC004771

Peliz, A., Boutov, D., Cardoso, R. M., Delgado, J., & Soares, P. M. M. (2013). The Gulf of Cadiz-Alboran Sea sub-basin: Model setup, exchange and seasonal variability. Ocean Modelling, 61, 49–67. https://doi.org/10.1016/j.ocemod.2012.10.007

Peliz, A., Boutov, D., Barbosa Aguiar, A., & Carton, X. (2014). The Gulf of Cadiz Gap wind anticyclones. Continental Shelf Research, 91, 171–191. https://doi.org/10.1016/j.csr.2014.09.004

Peliz, Á., Teles-Machado, A., Marchesiello, P., Dubert, J., & Lafuente, J. G. (2009). Filament generation off the Strait of Gibraltar in response to Gap winds. Dynamics of Atmospheres and Oceans, 46(1–4), 36–45. https://doi.org/10.1016/j.dynatmoce.2008.08.002

Pickett, M. H., & Paduan, J. D. (2003). Ekman transport and pumping in the California Current based on the U.S. Navy's high-resolution atmospheric model (COAMPS). Journal of Geophysical Research: Oceans, 108(10), 1–10. https://doi.org/10.1029/2003jc001902

Price, J. F., Baringer, M. O., Lueck, R. G., Johnson, G. C., Ambar, I., Parrilla, G., et al. (1993). Mediterranean Outflow Mixing and Dynamics. Science, 259(5099), 1277–1282. https://doi.org/10.1126/science.259.5099.1277

Prieto, L., Navarro, G., Rodríguez-Gálvez, S., Huertas, I. E., Naranjo, J. M., & Ruiz, J. (2009). Oceanographic and meteorological forcing of the pelagic ecosystem on the Gulf of Cadiz

shelf (SW Iberian Peninsula). Continental Shelf Research, 29(17), 2122–2137. https://doi.org/10.1016/j.csr.2009.08.007

Puertos del Estado: HFR data. Retrieved October 13, 2020 from http://opendap.puertos.es/thredds/ catalog/radar_local_huelva/catalog.html.

Reid, J. L. (1978). On the middepth circulation and salinity field in the North Atlantic Ocean. Journal of Geophysical Research, 83(C10), 5063. https://doi.org/10.1029/JC083iC10p05063

Reid, J. L. (1979). On the contribution of the Mediterranean Sea outflow to the Norwegian-Greenland Sea. Deep Sea Research Part A, Oceanographic Research Papers, 26(11), 1199–1223. https://doi.org/10.1016/0198-0149(79)90064-5

Relvas, P., & Barton, E. D. (2002). Mesoscale patterns in the Cape São Vicente (Iberian Peninsula) upwelling region. Journal of Geophysical Research, 107(C10), 3164. https://doi.org/10.1029/2000JC000456

Relvas, P., & Barton, E. D. (2005). A separated jet and coastal counterflow during upwelling relaxation off Cape São Vicente (Iberian Peninsula). Continental Shelf Research, 25(1), 29–49. https://doi.org/10.1016/j.csr.2004.09.006

Reul, A., Muñoz, M., Criado-Aldeanueva, F., & Rodríguez, V. (2006). Spatial distribution of phytoplankton <13μm in the Gulf of Cádiz in relation to water masses and circulation pattern under westerly and easterly wind regimes. Deep Sea Research Part II: Topical Studies in Oceanography, 53(11–13), 1294–1313. https://doi.org/10.1016/j.dsr2.2006.04.008

Ribas-Ribas, M., Gómez-Parra, A., & Forja, J. M. (2011). Air–sea CO2 fluxes in the north-eastern shelf of the Gulf of Cádiz (southwest Iberian Peninsula). Marine Chemistry, 123(1–4), 56–66. https://doi.org/10.1016/j.marchem.2010.09.005

Rippeth, T. P., Simpson, J. H., Williams, E., & Inall, M. E. (2003). Measurement of the Rates of Production and Dissipation of Turbulent Kinetic Energy in an Energetic Tidal Flow:

Red Wharf Bay Revisited. Journal of Physical Oceanography, 33(9), 1889–1901. https://doi.org/10.1175/1520-0485(2003)033<1889:MOTROP>2.0.CO;2

Rivas, D. (2017). Wind-driven coastal-trapped waves off southern Tamaulipas and northern Veracruz, western Gulf of Mexico, during winter 2012–2013. Estuarine, Coastal and Shelf Science, 185, 1–10. https://doi.org/10.1016/j.ecss.2016.12.002

Rosa, A., Cardeira, S., Pereira, C., Rosa, M., Madureira, M., Rita, F., et al. (2019). Temporal variability of the mass exchanges between the main inlet of Ria Formosa lagoon (southwestern Iberia) and the Atlantic Ocean. Estuarine, Coastal and Shelf Science, 228(August), 106349. https://doi.org/10.1016/j.ecss.2019.106349

Ruiz, J., & Navarro, G. (2006). Upwelling spots and vertical velocities in the Gulf of Cádiz: An approach for their diagnose by combining temperature and ocean colour remote sensing. Deep-Sea Research Part II: Topical Studies in Oceanography, 53(11–13), 1282–1293. https://doi.org/10.1016/j.dsr2.2006.04.006

Sánchez-Leal, R. F., Bellanco, M. J., Naranjo, C., García-Lafuente, J., & González-Pola, C. (2020). On the seasonality of waters below the seasonal thermocline in the Gulf of Cádiz. Continental Shelf Research, 204(June). https://doi.org/10.1016/j.csr.2020.104190

Sánchez-Leal, Ricardo F., Bellanco, M. J., Fernández-Salas, L. M., García-Lafuente, J., Gasser-Rubinat, M., González-Pola, C., et al. (2017). The Mediterranean Overflow in the Gulf of Cadiz: A rugged journey. Science Advances, 3(11), eaao0609. https://doi.org/10.1126/sciadv.aao0609

Sánchez, R.F., Mason, E., Relvas, P., da Silva, A. J., & Peliz, Á. (2006). On the inner-shelf circulation in the northern Gulf of Cádiz, southern Portuguese shelf. Deep Sea Research Part II, 53(11–13), 1198–1218. https://doi.org/10.1016/j.dsr2.2006.04.002

Sánchez, Ricardo F., & Relvas, P. (2003). Spring–summer climatological circulation in the upper layer in the region of Cape St. Vincent, Southwest Portugal. ICES Journal of Marine Science, 60(6), 1232–1250. https://doi.org/10.1016/S1054-3139(03)00137-1

Sánchez, Ricardo F., Relvas, P., & Delgado, M. (2007). Coupled ocean wind and sea surface temperature patterns off the western Iberian Peninsula. Journal of Marine Systems, 68(1–2), 103–127. https://doi.org/10.1016/j.jmarsys.2006.11.003

Santos, A. I. P. (2005). Caracterização hidro-sedimentológica do estuário do Guadiana. Universidade Técnica de Lisboa Instituto Superior Técnico.

Savenije, H. H. G. (2012). Salinity and tides in alluvial estuaries (2nd Ed.) Elsevier Science. http://hubertsavenije.files.wordpress.com/2014/01/salinityandtides2_21.pdf

Send, U., Beardsley, R. C., & Winant, C. D. (1987). Relaxation from upwelling in the Coastal Ocean Dynamics Experiment. Journal of Geophysical Research, 92(C2), 1683–1698. https://doi.org/10.1029/JC092iC02p01683

Silva, A. J. da, Santos, A. I., Garcia, A. C., & González, R. (2008). Análise dos resultados referentes à segunda fase de execução do projecto SIRIA: Dezembro 2000 - Dezembro 2001 e relatório final do projecto.

Simpson, J. H., & Sharples, J. (2012). Introduction to the Physical and Biological Oceanography of Shelf Seas. In Introduction to the Physical and Biological Oceanography of Shelf Seas (pp. 306–313). Cambridge: Cambridge University Press. https://doi.org/10.1017/CBO9781139034098

Simpson, J. H., Crawford, W. R., Rippeth, T. P., Campbell, A. R., & Cheok, J. V. S. (1996). The Vertical Structure of Turbulent Dissipation in Shelf Seas. Journal of Physical Oceanography, 26(8), 1579–1590. https://doi.org/10.1175/1520-0485(1996)026<1579:TVSOTD>2.0.CO;2

Solabarrieta, L., Rubio, A., Castanedo, S., Medina, R., Charria, G., & Hernández, C. (2014). Surface water circulation patterns in the southeastern Bay of Biscay: New evidences from HF radar data. Continental Shelf Research, 74, 60–76. https://doi.org/10.1016/j.csr.2013.11.022

Sordo, I., Barton, E. D., Cotos, J. M., & Pazos, Y. (2001). An Inshore Poleward Current in the NW of the Iberian Peninsula Detected from Satellite Images, and its Relation with G.

catenatum and D. acuminata Blooms in the Galician Rias. Estuarine, Coastal and Shelf Science, 53(6), 787–799. https://doi.org/10.1006/ecss.2000.0788

Stacey, M. T., Burau, J. R., & Monismith, S. G. (2001). Creation of residual flows in a partially stratified estuary. Journal of Geophysical Research: Oceans, 106(C8), 17013–17037. https://doi.org/10.1029/2000JC000576

Stevenson, R. E. (1977). Huelva Front and Malaga, Spain, eddy chain as defined by satellite and oceanographic data. Deutsche Hydrographische Zeitschrift, 30(2), 51–53. https://doi.org/10.1007/BF02226082

Teles-Machado, A., Peliz, Á., Dubert, J., & Sánchez, R. F. (2007). On the onset of the Gulf of Cadiz Coastal Countercurrent. Geophysical Research Letters, 34(12), L12601. https://doi.org/10.1029/2007GL030091

Thorpe, S. A. (2004). Recent Developments in the Study of Ocean Turbulence. Annual Review of Earth and Planetary Sciences, 32(1), 91–109. https://doi.org/10.1146/annurev.earth.32.071603.152635

Trenberth, K. E., Large, W. G., & Olson, J. G. (1990). The Mean Annual Cycle in Global Ocean Wind Stress. Journal of Physical Oceanography, 20(11), 1742–1760. https://doi.org/10.1175/1520-0485(1990)020<1742:TMACIG>2.0.CO;2

Trigo, R. M., & DaCamara, C. C. (2000). Circulation weather types and their influence on the precipitation regime in Portugal. Int. J. Climatol., 20, 1559–1581.

Vargas, J. M., García-Lafuente, J., Delgado, J., & Criado, F. (2003). Seasonal and wind-induced variability of Sea Surface Temperature patterns in the Gulf of Cádiz. Journal of Marine Systems, 38(3–4), 205–219. https://doi.org/10.1016/S0924-7963(02)00240-3

Wang, D. (1997). Effects of small-scale wind on coastal upwelling with application to Point Conception. Journal of Geophysical Research: Oceans, 102(C7), 15555–15566. https://doi.org/10.1029/97JC00635

Washburn, L., & McPhee-Shaw, E. (2013). Coastal Transport Processes Affecting Inner-Shelf Ecosystems in the California Current System. Oceanography, 26(3), 34–43. https://doi.org/10.5670/oceanog.2013.43

Washburn, L., Fewings, M. R., Melton, C., & Gotschalk, C. (2011). The propagating response of coastal circulation due to wind relaxations along the central California coast. Journal of Geophysical Research, 116(C12), C12028. https://doi.org/10.1029/2011JC007502

Wesson, J. C., & Gregg, M. C. (1994). Mixing at Camarinal Sill in the Strait of Gibraltar. Journal of Geophysical Research, 99(C5), 9847–9878. https://doi.org/10.1029/94JC00256

Winant, C. D., Beardsley, R. C., & Davis, R. E. (1987). Moored wind, temperature, and current observations made during Coastal Ocean Dynamics Experiments 1 and 2 over the Northern California Continental Shelf and upper slope. Journal of Geophysical Research, 92(C2), 1569–1604. https://doi.org/10.1029/JC092iC02p01569

Winant, C. D., Dever, E. P., & Hendershott, M. C. (2003). Characteristic patterns of shelf circulation at the boundary between central and southern California. Journal of Geophysical Research, 108(C2), 3021. https://doi.org/10.1029/2001JC001302

Wing, S., Botsford, L., Largier, J., & Morgan, L. (1995). Spatial structure of relaxation events and crab settlement in the northern California upwelling system. Marine Ecology Progress Series, 128(1–3), 199–211. https://doi.org/10.3354/meps128199